Band structure vs. localized f electrons: High field magnetism in uranium intermetallics

Von der Fakultät für Elektrotechnik, Informationstechnik, Physik
der Technischen Universität Carolo-Wilhelmina zu Braunschweig

zur Erlangung des Grades eines Doktors
der Naturwissenschaften (Dr. rer. nat.)

genehmigte Dissertation

von

Dirk Schulze Grachtrup
aus Warendorf

1. Referent: Prof. Dr. Stefan Süllow
2. Referent: Prof. Dr. Joachim Wosnitza

eingereicht am: 28.4.2014

mündliche Prüfung (Disputation) am: 22.10.2014

Druckjahr: 2014

Abstract

We have studied the uranium intermetallic compounds $U(Pd_{1-x}Pt_x)_3$ and UPt_2Si_2 to determine the degree of localization or itinerancy of the uranium $5f$ electrons in their respective environments.

For single crystalline UPt_2Si_2 an extensive high magnetic field study was performed including measurements of the magnetization in pulsed magnetic fields up to 52 T and measurements of resistivity, magnetoresistivity and Hall effect in DC magnetic fields up to 35 T. From these measurements we have constructed the magnetic phase diagrams along the a and c axes. For the magnetic field applied along the a axis we find a new region indicated by strong hysteresis below ≈ 20 K in magnetic fields of ≈ 35 to 48 T resulting in a very uncommon magnetic phase diagram along this direction. For the magnetic field applied along the c axis at least three field induced phases are observed above 24 T at temperatures below ≈ 18 K leading to a very exotic magnetic phase diagram. From a careful analysis of our Hall effect data including anomalous contributions and a comparison to recent band structure calculations we identified at least one of the field induced phase transitions as a Lifshitz or electronic topological transition.

For the quadrupolar ordering compound $U(Pd_{1-x}Pt_x)_3$ we have characterized single crystalline samples with low alloying levels of $x = 0.5\%$ and 1% by means of specific heat, resistivity and susceptibility measurements. Against expectation for Pt levels as low as 0.5% we observe a strong reduction of the ordering temperatures by approximately one half upon isoelectronic alloying at the Pd sites and only short range order at $x = 1\%$. From our data we have constructed the magnetic phase diagrams along the a and c axes for $x = 0.5\%$ and an alloying phase diagram. From the magnetic field dependency of the ordering temperatures we conclude that the physical mechanisms are identical for UPd_3 and $U(Pd_{1-x}Pt_x)_3$ at low alloying levels. To identify critical parameters which cause the observed strong reduction of ordering temperatures we have set up mean field modeling allowing for shifts of crystal electric field levels, Zeeman splitting and multiple quadrupolar order parameters. In such models we reproduce large parts of the experimentally determined magnetic phase diagram. Furthermore, in these models we find an extraordinary large sensitivity of the ordering temperatures against changes of the quadrupolar coupling constants which may account for our experimental observations.

Vorabveröffentlichungen der Dissertation

Teilergebnisse aus dieser Arbeit wurden mit Genehmigung der Fakultät für Elektrotechnik, Informationstechnik, Physik, vertreten durch den Betreuer der Arbeit, in folgenden Beiträgen veröffentlicht:

Publikationen:

- D. Schulze Grachtrup, M. Bleckmann, S. Süllow, B. Willenberg, H. Rakoto, Y. Skourski, and J. A. Mydosh: *High Field Magnetization of* UPt_2Si_2, J. Low Temp. Phys., **159**, 147 (2010)

- D. Schulze Grachtrup, M. Bleckmann, B. Willenberg, S. Süllow, M. Bartkowiak, Y. Skourski, H. Rakoto, I. Sheikin, and J. A. Mydosh: *Field-induced phases in* UPt_2Si_2, Phys. Rev. B, **85**, 054410 (2012)

Tagungsbeiträge:

- International Workshop on Correlated Electron Systems in High Magnetic Fields (CORMAG08) 2008 in Dresden, Germany: *Magnetic field dependency of the spin excitation gap in* UPt_2Si_2 (Poster).

- 9th International Conference on Research in High Magnetic Fields (RHMF) 2009 in Dresden, Germany: *Field induced phases in* UPt_2Si_2 (Poster).

- European School on Magnetism (ESM) 2009 in Timisoara, Romania: *Field induced phases in* UPt_2Si_2 (Poster).

- 9th Prague Colloquium on f-electron systems (PCFES) 2010 in Prague, Czech Republic: *Field induced phases in* UPt_2Si_2 (Talk).

- Frühjahrstagung der Deutschen Physikalischen Gesellschaft 2011 in Dresden, Germany: *Exotic field induced phases in* UPt_2Si_2 (Poster).

- Strongly Correlated Electron Systems (SCES) 2011 in Cambridge, United Kingdom: *Exotic Field Induced Phases in* UPt_2Si_2 (Poster).

- Frühjahrstagung der Deutschen Physikalischen Gesellschaft 2012 in Berlin, Germany: *Annealing effects in the antiferroquadrupolar compound* $U(Pd_{1-x}Pt_x)_3$ (Poster).

- 10th Prague Colloquium on f-electron systems (PCFES) 2012 in Prague, Czech Republic: *High field Hall measurements on* UPt_2Si_2 *at very low temperatures* (Poster).

- Frühjahrstagung der Deutschen Physikalischen Gesellschaft 2013 in Regensburg, Germany: *High field Hall measurements on* UPt_2Si_2 *at very low temperatures* (Talk).

Contents

1 Introduction

Materials sciences have been of great interest for mankind since the stone age. While in the early times pragmatic solutions to everyday problems like hunting or surviving with the available materials (wood, leather, stones, etc.) were the main task, the focus has to a large part shifted to metallic materials in the bronze and iron ages. However, in these times "materials science" was more adequately described as artisanal work than as science according to todays standards. This remained true until the 19th century when systematic analyses of the properties of steels, alloys and ceramics became widespread and materials science became a well-defined field of research, even to nowadays standards. Since then this field has diversified, still including metallic materials, from pure and simple elements to complex alloys, as well as plastics, ceramics, glasses, biological matter and others. Moreover, all these materials may be combined and put in different shapes, for instance as bulk material, thin films, foams, etc. which again may change their properties. In the last decades this large variety has lead to the discovery of many new effects and lots of new materials with special properties. Subsequently these new materials have enabled the rapid development of new technologies, in particular in electronics and optics with the archetypal example, the computer being ubiquitous now.

However, due to the almost infinite number of imaginable combinations of materials and shapes there is a growing interest in changing the scientific process from systematically analyzing materials that can be produced to designing new materials with specified properties for certain applications. Until now this is still a difficult if not impossible task since many material properties depend strongly on very small changes of the microscopic details and the competition of different energy scales and interactions on the atomic level. Hence, it is desirable to obtain a deeper understanding of all these mechanisms. Such an understanding on the other hand might then enable us to produce materials with adjustable physical properties which might help to solve urging problems such as the growing energy and resource consumption or enable more efficient, cheaper, less toxic or in other ways improved replacements of existing technologies.

Especially in the area of metals and alloys complex and advanced materials are used nowadays for many very special applications like levitation with high T_C superconductors, sophisticated magnetic recording and reading techniques in computers or the production of strong permanent magnets for various applications. All these effects and special properties are a result of the respective (metallic) environments where strong interactions between the electrons and nuclei of the material and with external fields and forces exist. The interactions in these systems give rise to many different and often competing ordering phenomena from which magnetism and superconductivity are probably the most well-known. Some of these complex systems, that is the systems with extraordinary strong interactions are referred to as strongly correlated systems and which have become an important topic in recent research efforts. However, even after more than one century of research on magnetic systems and many theoretical efforts a simple theory of magnetism dealing with most magnetic phenomena (comparable to Maxwell's equations for electromagnetic fields) is still absent although many theories exist to explain special aspects of magnetism and magnetic ordering for many materials. The same is true for the unconventional and high T_c superconductors. Thus, large efforts are put in this field to gain further understanding of such complex interactions and ordering mechanisms.

The materials studied in this thesis are especially interesting since they contain uranium atoms in a metallic alloy which gives rise to interactions between electrons in spatially extended uranium f orbitals (but which are still predominantly localized at the uranium atoms) and quasi-free conduction electrons. These localized $5f$ electrons may then hybridize with the conduction electrons forming quasiparticles with a renormalized effective mass m^* which can be described with Fermi-liquid theory in many cases. Depending on the effective mass of the quasiparticles these systems range from moderately correlated with m^* being some free electron masses m_0 up to very strongly correlated so-called heavy Fermion systems with m^* being more than $1000\,m_0$. Such interactions are not only limited to uranium systems but can also be observed in most metallic systems containing $4f$ or $5f$ electrons, that is most metallic rare earth and actinide systems. Depending on the degree of hybridization the f electrons have to be treated as localized, itinerant or something in between.

Moreover, in these systems often an interaction of the magnetic moments of the localized and conduction electrons is found leading to the Kondo effect which describes the formation of a polarized conduction electron cloud around localized electrons which shields the localized magnetic moment. Depending on temperature, magnetic interaction strength and details of the electronic structure of the compound this may lead to a simple quasi-paramagnetic state. However, since magnetic interactions support long-range order in contrast to the competing shielding due to the Kondo effect the ground state strongly depends on very subtle details of the electronic structure. Thus, for one single compound there may exist multiple stable ordered states depending on various parameters, material properties and temperature. In such compounds multiple phase transitions between different electronic states can be observed. In some of these materials even so-called quantum phase transitions are found where a phase transition (the change of the electronic ground state) is not driven by changing temperature but by variation of some other control parameter at zero temperature, for instance a magnetic field or applied pressure. Thus, such transitions also take place at absolute zero temperature although experimental evidence is found only down to the lowest achievable temperatures close to absolute zero.

This large variety of possible interactions, couplings and competing ground states gives rise to a huge number of possible electronic structures. Unfortunately, this variety also causes ambiguities in data interpretation since the same set of experimental data might be attributed to different electronic structures or different models of the electronic structure might give similar predictions with respect to experimental findings. And although many of the electronic structures are simple and easy to confirm or to falsify, some structures are difficult to understand for instance the famous *hidden order* phase in URu_2Si_2 where the order parameter is still unknown despite decades of intense experimental and theoretical efforts.

In this thesis the focus is put on two systems which are, or at least have been thought to be, less exotic than many other $4f$ and $5f$ systems. These systems, UPt_2Si_2 and $U(Pd_{1-x}Pt_x)_3$ or the pure system UPd_3, were considered as well localized f electron systems for many years. As we will show, this might not be the whole story. The thesis is structured as follows.

In **chapter 2** we will give a brief introduction to the concept of the crystalline electric field. This is the electric field at the position of a charge carrying particle which is generated by the surrounding charge distribution. This field then modifies the energy of different electronic states and lifts the degeneracy of degenerate electronic orbitals. Using certain mathematical transformations the Hamiltonian of a crystal electric field scheme can be written in a rather simple form where the number of terms is strongly limited due to the crystal symmetry. This description is widely used to treat problems concerning localized electron systems. Furthermore, we will introduce the mean field approximation which will be used later.

Next, in **chapter 3** a review on the basics of Lifshitz transitions will be given. These transitions are also known as electronic topological transitions (ETT) or $2\frac{1}{2}$ order transitions and describe a phase transition due to a changing Fermi surface topology. Since it is an effect of the Fermi surface these transitions only take place in conducting systems where the definition of a Fermi surface makes sense. Unfortunately the signatures of Lifshitz transitions are usually small and ambiguous, hence the existence of Lifshitz transition has been proven unequivocally only for very few systems so far.

In **chapter 4** first a summary of the most important physical properties of UPt_2Si_2 is given. Additionally, we present new high magnetic field measurements from which we have constructed a complex high magnetic field phase diagram. Although sample quality is an issue in this compound and absolute values strongly depend on experimental details the overall features do not. From a comparison with systems that resemble UPt_2Si_2 in different aspects we conclude that UPt_2Si_2 has to be treated in a more itinerant approach and that a Lifshitz transition is highly likely in this compound. This finding is in agreement with very recent theoretical publications.

Finally, in **chapter 5** we will give an overview on the physical properties of pure UPd_3 and perform a comparison to the doped system $U(Pd_{1-x}Pt_x)_3$ with very low Pt doping levels. UPd_3 is one of the rare examples of compunds where qudrupolar order is observed. We will find that the observed properties of $U(Pd_{1-x}Pt_x)_3$ are difficult to explain if we assume a completely localized picture as in UPd_3. In order to verify or falsify the local moment assumption of $\mathrm{U(Pd}_{1-x}\mathrm{Pt}_x)_3$ we set up several mean field CEF models of this compound and compare our calculated physical properties and magnetic phase diagrams to experimental data.

2 The crystal electric field

The crystal electric field (CEF) is a model to describe the physical properties of electrons localized at an ion in a surrounding regular arrangement of charges or charge distributions, especially in a surrounding crystal lattice. Multiple reviews have been written dealing with this topic, for instance Refs. [1–3]. Furthermore, multiple papers have been published tabulating most potential functions and operators used in this field, e.g. Refs. [4–7]. In the following we will present a shortened overview of the arguments and calculations given in Refs. [1–3] mostly using (besides minor modifications) the notation of Ref. [2].

To apply the crystal electric field model it is first necessary to know the atoms electronic wave function which solves the stationary Schrödinger equation

$$H\Psi = E\Psi \tag{2.1}$$

with the non-relativistic Hamiltonian

$$H = -\frac{\hbar}{2m}\sum_{i}^{Z}\nabla_i^2 + \frac{1}{2}\sum_{i,j}^{Z}\frac{e^2}{|\vec{r}_i - \vec{r}_j|} + \sum_{i}^{Z} v_{ext}(\vec{r}_i) \tag{2.2}$$

where the three terms represent the kinetic energy, the coulomb interaction and an energy due to an external potential v_{ext} for the Z electrons of the atom. For a complete and precise treatment of this problem also effects like relativistic corrections have to be taken into account and the whole problem needs to be solved, for instance, with a self consistent Hartree-Fock procedure. Since the potential of an atom is spherically symmetric the solutions (the single electron wavefunctions) can be written as a product of a radial function $R_{n\,l}(r)$, a spherical harmonic $Y_{l\,m_l}(\vec{\hat{r}})$ and a spin function χ_{m_s} as

$$\psi_{n\,l\,m_l\,m_s}(\vec{r}\sigma) = R_{n\,l}(r)Y_{l\,m_l}(\vec{\hat{r}})\chi_{m_s} \tag{2.3}$$

where $\vec{\hat{r}}$ is the unit vector in direction of $\vec{r}$ and $r = |\vec{r}|$. Each partial function can be found by solving a determining equation separately.

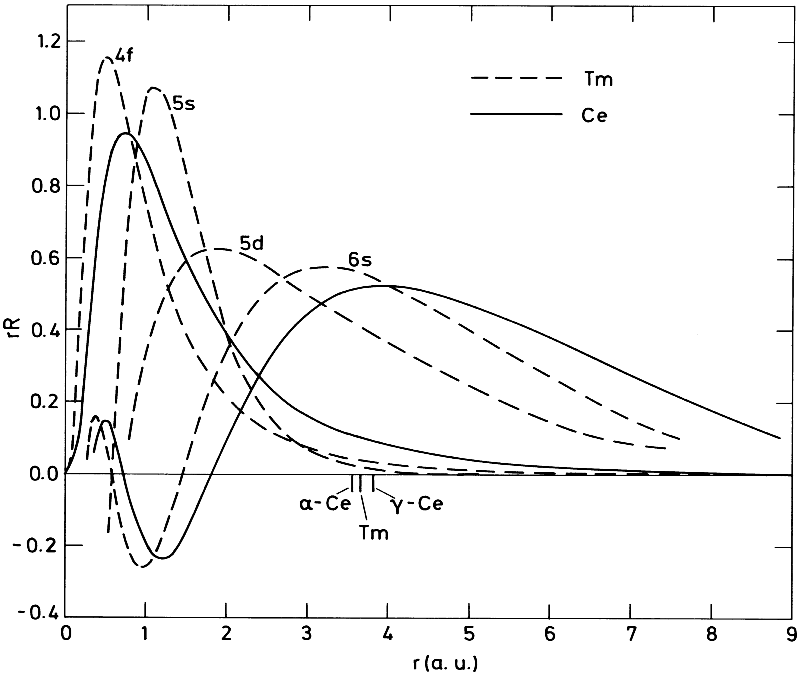

Figure 2.1: Radial components of some atomic wavefunctions for Tm and Ce. It can be seen that the *f* electrons are generally more localized with small distances from the nucleus while *s* and *d* states are more extended [2].

Here, the electrons quantum numbers n (principal quantum number), l (orbital quantum number), m_l (magnetic quantum number) and m_s (spin projection quantum number) appear which completely determine the electrons orbital. As an example the radial and angular contributions for some quantum numbers of $4f$ electrons are depicted in Figs. 2.1 and 2.2 [2]. Hence, such an electronic state may be written in bra-ket notation as

$$|n\, l\, m_l\, m_s\rangle \tag{2.4}$$

for a single electron or, for an atom where the single electron orbital and spin moments are coupled to the atoms momenta L and S, as [1]

$$|L\, S\, L_z\, S_z\rangle\,. \tag{2.5}$$

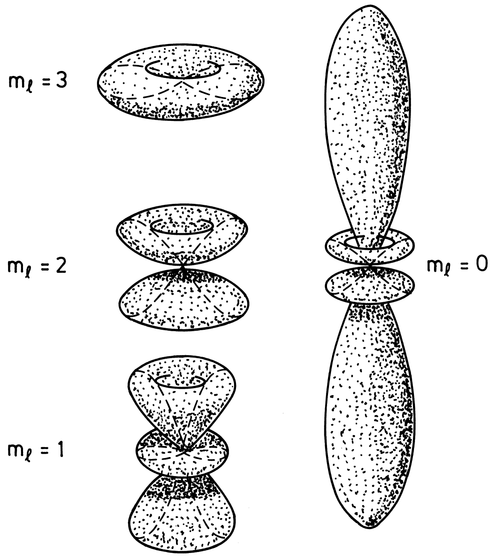

Figure 2.2: Angular component due to the spherical harmonic of some $4f$ electron wavefunctions for different m_l [2].

Since in this work special emphasis is laid on the uranium f electrons we will limit this short introduction to crystal electric fields to the case of f electrons although for other orbitals only few things are changed. Due to the rather strong spin-orbit coupling in the rare earths and actinides the Russel-Saunders coupling scheme is applied after the orbitals are occupied according to Hund's rules. Thus, first, the orbital and spin moments l_i and s_i of individual electrons i in unfilled shells are coupled forming the orbital and spin moments L and S of the atom and second, these moments are coupled giving the atoms total angular momentum $J = L + S$ or $J = |L - S|$. Then, in the appropriate basis this state in bra-ket notation is [1, 3]

$$|L\,S\,J\,J_z\rangle\,. \tag{2.6}$$

Without any potential acting upon the atom all these states have the same energy and are thus degenerate. However, if such an atom is located for example in a crystal lattice or a magnetic field it is exposed to a variety of interactions with its surrounding which lift this degeneracy. One very important interaction is due to the electric field caused by the surrounding charges of neighbouring atoms (the ligand atoms) and conduction electrons in the crystal. This electric field is named crystal (electric) field or ligand field [2, 3].

The crystal field causes a potential v_{cf} at the central atoms site which is given by

$$v_{cf}(\vec{r}) = -\int \frac{e\rho(\vec{R})}{|\vec{r} - \vec{R}|}\,d\vec{R} \tag{2.7}$$

and which solves the Poisson equation

$$\nabla^2 v_{cf}(\vec{r}) = -4\pi\rho(\vec{r}). \tag{2.8}$$

Thus, the potential may be expanded in spherical harmonics[1] as

$$v_{cf}(\vec{r}) = \sum_{p\,q} A_p^q r^l Y_{p\,q}(\hat{\vec{r}}) \tag{2.9}$$

---

[1] The potential may as well be written and expanded in cartesian coordinates. The calculations become more complex in this case but the results are identical.

with the coefficients given by

$$A_p^q = -(-1)^q \frac{4\pi}{2p+1} \int \frac{e\rho(\vec{R})}{R^{p+1}} Y_{p\,-q}(\hat{\vec{R}})\, d\vec{R} \tag{2.10}$$

when we assume that the charges producing the CEF lie outside the orbitals for which the CEF energies shall be calculated. If both charge distributions interleave the potential can still be expanded in spherical harmonics but the coefficients are different from Eq. 2.10 [2, 7, 8].

Since the crystal field splitting is small compared to the spin-orbit coupling in f electrons the effects of the CEF on the eigenstates can be treated with first-order perturbation theory. Now, to determine the matrix elements of the disturbing Hamiltonian for a system which remains in its J state the method proposed by Stevens using operator equivalents of the disturbing potential is widely used [1–4, 7].

To apply this method the spherical harmonics from Eq. 2.9 are expressed in cartesian coordinates and x, y, z and r^2 are replaced by the operators J_x, J_y, J_z and $J(J+1)$ where products of coordinates are expressed with all possible combinations of operators to allow for non-commutation. Hence, x becomes J_x while $x\,y$ becomes $\frac{1}{2}\,(J_xJ_y + J_yJ_x)$. These operator equivalents then define the so called Stevens operators O_p^q which are especially useful since the summation (or integration) over the k electrons is no longer necessary [4]. As an example potential terms due the spherical harmonics Y_{20} and Y_{21} in this notation become

$$\sum_{i=1}^{k} Y_{20} \rightarrow \sum_{i=1}^{k} (3z_i^2 - r_i^2) = \alpha_J \langle r^2 \rangle \left(3J_z^2 - J(J+1)\right) = \alpha_J \langle r^2 \rangle O_2^0 \tag{2.11}$$

and

$$\sum_{i=1}^{k} Y_{21} \rightarrow \sum_{i=1}^{k} x_i y_i = \alpha_J \langle r^2 \rangle \left(\frac{1}{2}(J_xJ_y + J_yJ_x)\right) = \alpha_J \langle r^2 \rangle O_2^1 \tag{2.12}$$

with $\langle r^2 \rangle$ being the average squared radius of the f states and α_J being a multiplicative factor which depends on the number of electrons in unfilled shells and their orbital quantum numbers l and J [1, 3]. It can be shown that the matrix elements of the disturbing Hamiltonian for these operator equivalents are identical to the ones of the original potential, so that[2]

$$\langle L\,S\,J\,J_z|\sum_i Y_{p\,q}\,|L\,S\,J\,J_z\rangle = \alpha_J\,\langle r^2\rangle\,\langle L\,S\,J\,J_z|\,O_p^q\,|L\,S\,J\,J_z\rangle \quad (2.13)$$

With this definition of the Stevens operators the disturbing crystal field Hamiltonian for a single ion can now be written in a simple form as

$$H_{cf} = \sum_{p\,q} B_p^q O_p^q \quad (2.14)$$

where the coefficients B_p^q are the so-called crystal (electric) field or CEF parameters [1–3].

There are many restrictions on which of the coefficients may be non-zero since the crystal electric field potential has to reflect the symmetry of the lattice. Thus, the more symmetric the crystal is, the less non-zero crystal electric field parameters exist. First, $p = 0$ only gives an additive constant to the potential which has no physical effect and can hence be omitted. Second, it can be shown that in the general case $p \leq 2l$ and for f electrons with $l = 3$ p is limited to $p \leq 6$. Third, if the site has inversion symmetry p needs to be even. And fourth, if the z-axis is an q-fold axis of symmetry terms $B_p^q O_p^q$ exist [1, 3].

Now, the crystal field hamiltonian (Eq. 2.14) can be diagonalized in a straightforward way which gives the Eigenstates and the CEF energy levels (Eigenvalues) of the atom in the crystal electric field. Starting

---

[2] Here, the integration of Eq. 2.7 to determine v_{cf} is replaced by a summation over i point charges. The results for an integration are identical.

with this CEF levels one may then go on and calculate various physical properties such as magnetization or susceptibility of the material in a next step [2]. For instance the magnetization of a material is

$$\langle M\rangle = \frac{1}{Z}\,\mathrm{Tr}(J_z g_J \mu_B\, e^{-\beta H_{cf}}) \tag{2.15}$$

with

$$Z = \mathrm{Tr}(e^{-\beta H_{cf}}) \qquad \text{and} \qquad \beta = \frac{1}{k_B T} \tag{2.16}$$

where g_J, μ_B and k_B are the Landé g-factor, the Bohr magneton and the Boltzmann constant [7].

In principle the crystal field parameters B_p^q may be calculated from the charge density distribution in the material. However, this requires very precise knowledge of the crystal structure and the charge distribution of all electrons of the central ion as well as the charge distributions of the ligand atoms. Since all these charge densities on the other hand interact and modify each other, usually this is not very accurate and crude approximations are necessary giving only a rough estimate of the crystal field parameters in most cases. As a very simple yet instructive model sometimes the charge densities are even approximated by point charges [2].

Furthermore, since the f electron orbitals have a strong anisotropy and interact witch the surrounding crystal there is some magnetoelastic coupling which additionally modifies the energies of the CEF levels. Effectively this coupling can be considered as a strain-dependent renormalization of the CEF parameters [2].

Due to the difficulties arising in the calculation of the crystal electric field parameters these are usually determined experimentally. This may be realized for instance by including a Zeeman term in the calculations so that the Hamiltonian becomes

$$H = H_{cf} + H_Z = \sum_{pq} B_p^q O_p^q - g_J \mu_B J_z H \tag{2.17}$$

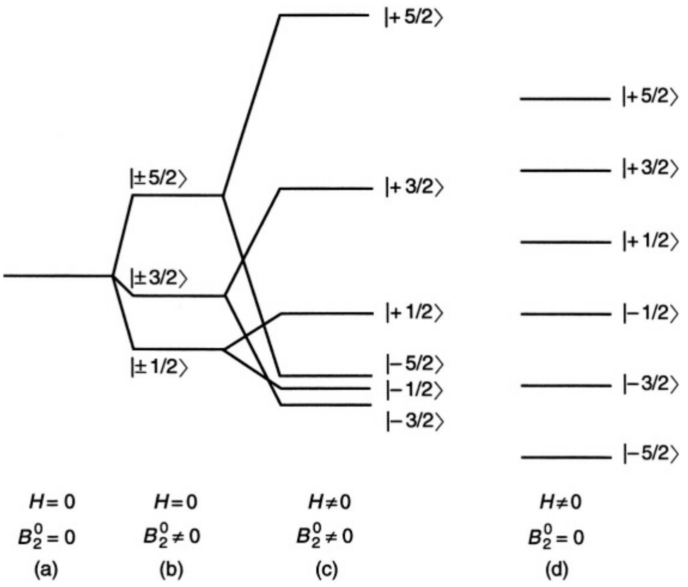

Figure 2.3: The crystal electric field levels for a $J = \frac{5}{2}$ manifold. Plotted are the CEF levels without CEF and magnetic field (a), with CEF only (b), with CEF and magnetic field (c) and for a magnetic field without CEF (d) [3].

where then the CEF parameters are varied and the CEF levels are calculated [9].

This may give a CEF scheme as depicted in Fig. 2.3 for a $J = \frac{5}{2}$ manifold. Next, from these levels physical properties like, for instance, the magnetization are calculated according to Eq. 2.15 and compared to experimental data. If the experimental and calculated data do not match this procedure is repeated with modified CEF parameters until sufficient agreement is achieved. The exemplary low temperature magnetization for the CEF scheme depicted in Fig. 2.3 is shown in Fig. 2.4.

Such a procedure can also be realized with inelastic neutron scattering, specific heat or any other technique that either provides direct access to the CEF levels or to properties that can be derived from a given set of CEF levels [3].

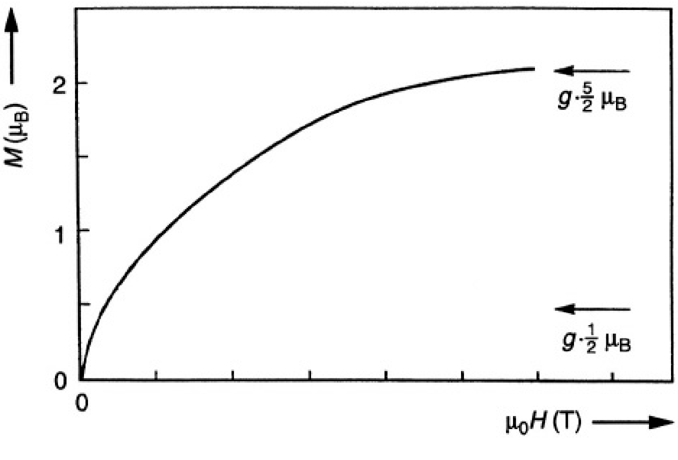

Figure 2.4: Calculated low temperature magnetization versus applied magnetic field for the CEF level scheme depicted in Fig. 2.3 [3].

2.1 The mean field approximation of magnetic ordering

The mean field description of a system is often used to calculate the magnetic ordering of a crystal with many interacting magnetic moments $\vec{J}$. These magnetic moments may be a result of localized orbitals in a crystal electric field scheme as described above but may as well have another origin. The main idea in this model is to replace the interaction of two arbitrary magnetic moments with an interaction of a single magnetic moment with an averaged (background) field, the mean field. In the literature the mean field model is described and used frequently. Here, we want to give a short introduction following Ref. [2] where the problem is treated in more detail.

The simplest Hamiltonian which is adequate to explain many magnetic structures in extended systems is

$$H = \sum_i H_{cf}(i) - \frac{1}{2} \sum_{ij} K_{ij} \vec{J}_i \vec{J}_j + H_Z(i) \tag{2.18}$$

where $H_{cf}(i)$ is the single ions CEF Hamiltonian from Eq. 2.14 for a single Ion i, the summation takes account of the interaction between different magnetic moments i and j and $H_Z(i)$ is the Zeeman Hamiltonian. This Zeeman term is

$$H_Z(i) = -\sum_i g_J \mu_B \vec{J}_i \vec{H}_i \tag{2.19}$$

allowing for different fields $\vec{H}_i$ at the different sites.

In order to determine the ground state with the lowest energy one needs to minimize the free energy

$$F = -k_B T \ln Z \tag{2.20}$$

of the system where

$$Z = \mathrm{Tr}(e^{-\beta H}) = \sum_n e^{-\beta E_n} \qquad \text{and} \qquad \beta = \frac{1}{k_B T}. \tag{2.21}$$

This calculation is simple in all cases where the Hamiltonian (Eq. 2.18) can be diagonalized in a straightforward way. However, the summation over $\vec{J}_i \vec{J}_j$ usually can not be performed easily. In order to deal with this product $\vec{J}_i \vec{J}_j$ can be rewritten as

$$\vec{J}_i \vec{J}_j = (\vec{J}_i - \langle \vec{J}_i \rangle)(\vec{J}_j - \langle \vec{J}_j \rangle) + \vec{J}_i \langle \vec{J}_j \rangle + \vec{J}_j \langle \vec{J}_i \rangle - \langle \vec{J}_i \rangle \langle \vec{J}_j \rangle \tag{2.22}$$

where $\vec{J}_i - \langle \vec{J}_i \rangle$ are the fluctuations around the equilibrium value. These are considered to be small compared to $\langle \vec{J}_i \rangle$ and thus the first term on the right-hand side of Eq. 2.22 may be neglected. This is called the mean field approximation. Next, with

$$\vec{J}_i \langle \vec{J}_j \rangle \approx \vec{J}_j \langle \vec{J}_i \rangle \tag{2.23}$$

the product becomes

$$\vec{J}_i \vec{J}_j \approx 2\vec{J}_i \langle \vec{J}_j \rangle - \langle \vec{J}_i \rangle \langle \vec{J}_j \rangle. \tag{2.24}$$

With this result now the Hamiltonian (Eq. 2.18) is effectively decoupled and can be written as a sum of single-site Hamiltonians as

$$H \approx \sum_i H_{MF}(i) \tag{2.25}$$

where the single-site Hamiltonian is

$$H_{MF}(i) = H_{cf}(i) - \vec{J}_i g_J \mu_B \vec{H}_i - (\vec{J}_i - \frac{1}{2} \langle \vec{J}_i \rangle) \sum_j K_{ij} \langle \vec{J}_j \rangle \, . \tag{2.26}$$

In a next step an effective field is defined as

$$\vec{H}_i^{eff} = g_J \mu_B \vec{H}_i + \sum_j K_{ij} \langle \vec{J}_j \rangle \tag{2.27}$$

with which the mean field Hamiltonian (Eq. 2.26) can be written as

$$H_{MF}(i) = H_{cf}(i) - \vec{J}_i \vec{H}_i^{eff} + \frac{1}{2} \langle \vec{J}_j \rangle \, (\vec{H}_i^{eff} - g_J \mu_B \vec{H}_i). \tag{2.28}$$

The solutions of this mean field Hamiltonian may in some cases be found by means of self-consistent equations analytically or more generally by numerical procedures given that the crystal lattice and the magnetic structure are commensurable. The last term in Eq. 2.28 only gives an additive constant to the free energy F_i but does not affect $\langle \vec{J}_i \rangle$.

As long as the ordered magnetic moment $\langle \vec{J}_i \rangle$ is sufficiently small the free energy of the ith site can be expanded in powers of $\langle \vec{J}_i \rangle$. For a Hamiltonian

$$\tilde{H}(i) = H_{cf}(i) - \vec{J}_i \vec{h} \tag{2.29}$$

the free energy may be written as

$$\tilde{F}_i = \frac{F_0}{N} - \langle \vec{J}_i \rangle \, \vec{h} + \sum_{\alpha} A_\alpha \, \langle \vec{J}_{i\,\alpha} \rangle^2 + \sum_{\alpha\,\beta} B_{\alpha\beta} \, \langle \vec{J}_{i\,\alpha} \rangle^2 \, \langle \vec{J}_{i\,\beta} \rangle^2 + \ldots \tag{2.30}$$

where the coefficients A_α and $B_{\alpha\beta}$ may be determined from the zero-field limit of the susceptibility and J for some cases.

To find the free energy of the whole system the expansion of $\tilde{F}_i$ of the single sites is summed over i, the magnetic field $\vec{h}$ is replaced by the exchange field

$$\vec{H}_i^{eff} = \sum_j K_{ij} \langle \vec{J}_j \rangle \tag{2.31}$$

and the constant

$$\frac{1}{2} \langle \vec{J}_i \rangle \vec{H}_i^{eff} \tag{2.32}$$

is added so that the free energy becomes

$$F = F_0 - \frac{1}{2} \sum_{ij} K_{ij} \langle \vec{J}_i \rangle \langle \vec{J}_j \rangle + \sum_i \left(\sum_\alpha A_\alpha \langle \vec{J}_{i\,\alpha} \rangle^2 + \sum_{\alpha\,\beta} B_{\alpha\beta} \langle \vec{J}_{i\,\alpha} \rangle^2 \langle \vec{J}_{i\,\beta} \rangle^2 \right) \tag{2.33}$$

This expansion of the free energy as a function of the order parameters is called the Landau expansion. With this mean field approximation and the Landau expansion many properties of materials where magnetic order is possible can be calculated. This will later be used, in particular in chapter 5 of this thesis.

3 The concept of Lifshitz transitions

Although the theoretical concept of Lifshitz transitions is well established since 1960 it has been widely unnoticed for decades since experimental proof of these transitions was almost impossible. In recent years there has been a renewed interest in such transitions since experimental techniques are nowadays capable of detecting the small signatures of Lifshitz transitions. As a consequence such transitions have been proposed for different materials in the last years.

A Lifshitz transition is an *electronic topological transition* (ETT) due to a change of the Fermi surface topology as function of an external control parameter. According to Ehrenfest's notation it is also known as a $2\frac{1}{2}$-order transition due to an exponent $2\frac{1}{2}$ in the thermodynamic potential Ω [10–12]. This type of transition has been first proposed by I. M. Lifshitz in 1960 to be induced by externally applied pressure to a metal but has recently also been observed or proposed to occur as a result of doping or applied magnetic field [13–20]. Since it is an effect related to the modification of the Fermi surface such transitions only appear in materials where a Fermi surface exists, i.e. metals. In such materials the topology of the Fermi surface may be altered in different ways as depicted in Fig. 3.1. Either, a neck of the Fermi surface can become disrupted or connected, or a separate region of a Fermi surface can appear or disappear.

A well arranged overview over the theory concerning Lifshits transi-

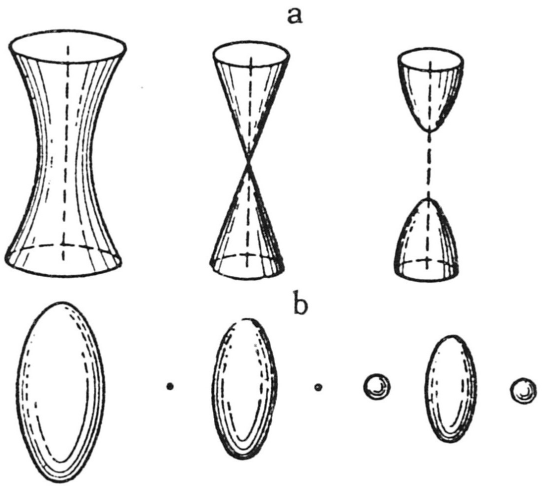

Figure 3.1: Fermi surface evolution across a Lifshitz transition according to Ref. [10]. Disruption of a neck (a) and appearance of a new separate region (b) of the Fermi surface.

tions has been given by Blanter *et al.* in Ref. [11]. In the following paragraphs we will present a shortened overview over some of their considerations using their notation. All of the given arguments apply only for conductors where a band structure with a dispersion relation $\epsilon(\vec{k})$ exists.

With the approximation of indenpent electrons every electronic state in a metal is described by its band number s and its momentum $\vec{p}$. For all possible states within the band s the energy $\epsilon^{(s)}(\vec{p})$ varies within certain limits, that is between $\epsilon^{(s)}_{min}$ and $\epsilon^{(s)}_{max}$. An appropriate description of the band structure in order to discuss the concept of Lifshitz transitions is realized by means of equienergy surfaces where

$$\epsilon^{(s)}(\vec{p}) = \epsilon. \tag{3.1}$$

In metals the conduction electrons at the Fermi energy ϵ_F are of particular interest as they determine the electronic properties. These electrons occupy states in one or more partially filled bands which cross ϵ_F and hence the Fermi surface for a band s is defined by

$$\epsilon^{(s)}(\vec{p}) = \epsilon_F \tag{3.2}$$

and represents the border between filled and empty electronic states. Since for the conduction electrons at ϵ_F the change in energy $\delta\epsilon^{(s)}$ is

$$\delta\epsilon^{(s)} = \vec{v}_F^{(s)}\delta\vec{p} \tag{3.3}$$

because of

$$\vec{v}_F^{(s)}(\vec{p}) = \frac{\partial\epsilon^{(s)}}{\partial\vec{p}} \tag{3.4}$$

it is obvious that two physical values determine the material properties: First, the Fermi surface itself (shape, size, etc.) and second, the velocity distribution on the Fermi surface.

Now, for every band there exist at least the two energies $\epsilon_{min}^{(s)}$ and $\epsilon_{max}^{(s)}$ where the topology of the equienergy surfaces changes from existing to non-existing (van Hove theorem [21]). There may exist more energies where the topology of the equienergy surface is changed, namely when the energy ϵ coincides with a local Minimum or Maximum of $\epsilon^{(s)}(\vec{p})$. Since it is not important from which band the electrons originate the index s determining the band will be omitted from here. This situation is depiced in Fig. 3.2 for a band with two local extrema at $\vec{p}_{c,2}$ and $\vec{p}_{c,3}$.

Close to the local Extrema at the critical quasi-momentum $\vec{p}_c$ of a band the dispersion $\epsilon(\vec{p})$ can be expanded in a series. With

$$\vec{v}_c = \left.\frac{\partial\epsilon}{\partial\vec{p}}\right|_{\vec{p}=\vec{p}_c} = 0 \tag{3.5}$$

we find

$$\epsilon = \epsilon(\vec{p}_c) + \sum_{i=1}^{3}\frac{p_i'^2}{2m_i} \tag{3.6}$$

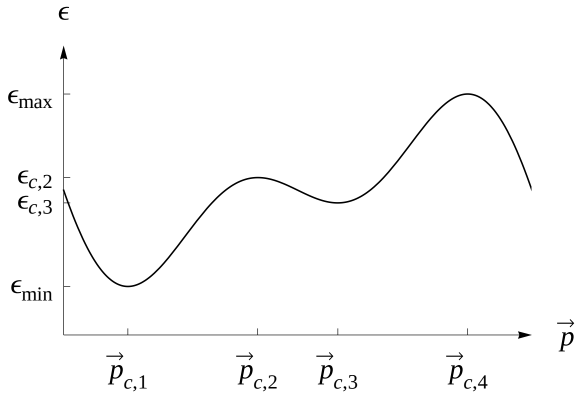

Figure 3.2: Schematic representation of an electronic band with two global extrema at $\vec{p}_{c,1}$ and $\vec{p}_{c,4}$ and two local extrema at $\vec{p}_{c,2}$ and $\vec{p}_{c,3}$ with their respective energies.

where

$$m_i = \left(\left. \frac{\partial^2 \epsilon}{\partial p_i^2} \right|_{\vec{p}=\vec{p}_c} \right)^{-1} \qquad \text{and} \qquad \vec{p'} = \vec{p} - \vec{p}_c. \tag{3.7}$$

If all effective masses m_i are positive (negative) the point $\vec{p_c}$ is a minimum (maximum) while for different signs of the m_i equienergy surfaces exist for $\epsilon < \epsilon_c$ and $\epsilon > \epsilon_c$ and the surface degenerates to a cone at $\epsilon = \epsilon_c$ $(\vec{p} = \vec{p}_c)$.

Many properties, and in particular the transport properties of a material, are determined by the density of states (DOS) $\nu(\epsilon)$ per energy. The DOS is defined as

$$\nu(\epsilon) = \frac{2V}{(2\pi\hbar)^3} \frac{d}{d\epsilon} \Delta(\epsilon) \tag{3.8}$$

where

$$\Delta(\epsilon) = \int \theta(\epsilon - \epsilon(\vec{p})) d^3\vec{p} \tag{3.9}$$

is the volume of the Brillouin zone with energy smaller than ϵ and $\theta(x)$

is the Heaviside function. This can be evaluated to

$$\nu(\epsilon) = \frac{2V}{(2\pi\hbar)^3} \oint\limits_{\epsilon(\vec{p})=\epsilon} \frac{d\Omega_{\vec{p}}}{\vec{v}(\vec{p})} \qquad \text{with} \qquad \vec{v}(\vec{p}) = \frac{\partial\epsilon(\vec{p})}{\partial\vec{p}} \tag{3.10}$$

where the integration of the surface elements $d\Omega_{\vec{p}}$ has to be carried out over the equienergy surface $\epsilon(\vec{p}) = \epsilon$. If this integration is performed one finds that in the vicinity of the critical energy ϵ_c (at the local extremum of the band) the DOS can be written in the form

$$\nu(\epsilon) = \nu_0(\epsilon) + \delta\nu. \tag{3.11}$$

Here, $\nu_0(\epsilon)$ is a smooth continuous function that originates from the integration far from the critical quasiparticle impulse $\vec{p}_c$, hence from $\vec{p} \ll \vec{p}_c$ and $\vec{p} \gg \vec{p}_c$. Contrary, $\delta\nu$ is a singular addition which originates from the integration with $\vec{p} \approx \vec{p}_c$. Depending on the type of extremum this singular addition either is determined to

$$\delta\nu(\epsilon) = a\sqrt{\epsilon - \epsilon_c}\,\theta(\epsilon - \epsilon_c) \qquad \text{with} \qquad a = \frac{V}{\pi^2\hbar^3}\sqrt{2m_1m_2m_3} \tag{3.12}$$

for a minimum or

$$\delta\nu(\epsilon) = a\sqrt{\epsilon_c - \epsilon}\,\theta(\epsilon_c - \epsilon) \qquad \text{with} \qquad a = \frac{V}{\pi^2\hbar^3}\sqrt{|2m_1m_2m_3|} \tag{3.13}$$

for a maximum.

As a result of these considerations, if one defines a Region I as the energy region where only the smooth part of the DOS contributes and a Region II with the singular addition, the latter can be rewritten as

$$\delta\nu(\epsilon) = \begin{cases} 0 & \text{in Region I} \\ \pm a\sqrt{|\epsilon - \epsilon_c|} & \text{in Region II.} \end{cases} \tag{3.14}$$

These singularities in the density of states now are the so-called van Hove singularities [21]. However, the exact calculation of the singular part $\delta\nu(\epsilon)$ in the density of states may become complicated since the local details of the Fermi surface are very important. Thus, usually very precise knowledge of the materials physical properties and complex numerical routines are necessary to perform such calculations.

If now the Fermi energy is close to the critical value ϵ_c the application of pressure or magnetic fields, doping or other effects, can slightly alter the materials physical properties in a way that the Fermi energy is shifted from above to below ϵ_c or vice versa. If this occurs, the topology of the Fermi surface is changed at ϵ_c, and the transition is called an electronic topological transition (ETT) or Lifshitz transition [10]. Depending on the combination of algebraic signs in Eq. 3.14 the type of topology change corresponds to the disruption/creation of a neck or the appearance/disappearance of new regions of the Fermi surface as depicted in Fig. 3.1.

Regarding above set out discussion, it should be kept in mind that usually the typical energy scales involved are very different, being some eV for the Fermi energy and electronic band widths and only meV for the experimentally caused shifts of the Fermi energy or the electronic band structure. Additionally, the arguments from Blanter *et al.* (Ref. [11]) presented above only remain valid if the band stucture as such survives the extreme environments required to induce such energy shifts and is not altered by another phase transition, for instance a structural transformation, before the Lifshitz transition takes place. Thus, Lifshitz transitions, although they have been observed in some materials, are not a widespread kind of phase transition [11, 13–20, 22].

As a result from the existence of the singular part in the DOS according to Eq. 3.14 a Lifshitz transition causes anomalies in the thermodynamic properties, for instance in specific heat, magnetization, compressibility, etc.. To evaluate these anomalies the thermodynamics of the electron gas can be calculated from the thermodynamic potential

$\Omega = \Omega(\mu, T)$ with the assumption that the density of states $\nu(\epsilon)$ is independent of temperature. This assumption is not true at elevated temperatures due to the shift of interatomic distances but it is fullfilled at low temperatures, that is $T \ll \Theta_D$. The thermodynamic potential Ω is given by

$$\Omega(\mu, T) = -\int\limits_0^\infty \frac{N(\epsilon)}{e^{\frac{\epsilon-\mu}{T}} + 1}\, d\epsilon \tag{3.15}$$

where

$$N(\epsilon) = \int\limits_0^\epsilon \nu(\epsilon')\, d\epsilon' \tag{3.16}$$

denotes the number of states below the energy ϵ. Now, if Ω is calculated according to Eq. 3.15 it can again be written as a sum of smooth and singular contribution $\delta\Omega$ as a result from the singular part $\delta\nu(\epsilon)$ in Eq. 3.14.

Since, in cases where a Lifshitz transition takes place in a material, the chemical potential μ has to be close to a critical energy ϵ_c in literature often a parameter z is defined as

$$z(T) = \mu(T) - \epsilon_c, \tag{3.17}$$

denoting the distance from the transition. With this definition the transition occurs at $z = 0$. Now, for zero temperature the singular part of Ω is found to be

$$\delta\Omega(T = 0) = \begin{cases} 0 & \text{in Region I} \\ -\frac{4}{15} a |z|^{\frac{5}{2}} & \text{in Region II.} \end{cases} \tag{3.18}$$

Due to the exponent $\frac{5}{2}$ it follows that second derivatives have a kink ($\propto \sqrt{z}$) at the transition point while third derivatives become infinite ($\propto \frac{1}{\sqrt{z}}$). Additionally, this is the reason why these transitions have been called $2\frac{1}{2}$ order phase transitions by I. M. Lifshitz according to Ehrenfest terminology [10, 12]. These anomalies in the derivatives of the thermodynamic potential can be found experimentally for instance in the electronic part of specific heat, bulk modulus (second derivatives) and thermal expansion coefficient (third derivative) [11].

At finite temperatures Equation 3.18 becomes more complex, with the calculations now leading to

$$\delta\Omega(T>0) = \begin{cases} -\sqrt{\frac{\pi}{2}}aT^{\frac{5}{2}}e^{-\frac{|z|}{T}} & \text{in Region I} \\ -\frac{4}{15}a|z|^{\frac{5}{2}} - \frac{\pi^2}{6}aT^2\sqrt{|z|} & \text{in Region II.} \end{cases} \tag{3.19}$$

Here, a finite contribution of the singular part is found on both sides of the transition which makes anomalies of physical properties derived from Ω less evident. Moreover, in real crystals various types of imperfections exist, and which cause scattering at defects and broaden the signatures of a Lifshitz transition even more. Due to these effects the anomalies associated to the transition in real materials become small and wipe out with temperature. Altogether, features in experimental properties of materials are subtle and the interpretation of experimental data in the context of Lifshitz transitions becomes difficult and is often ambiguous. Therefore, usually a combination of experiments and theoretical calculations is necessary to definitely establish the presence of a Lifshitz transition.

Although features in experimental data pointing to a Lifshitz transition have been observed earlier for some metals and alloys and a Lifhsitz transition was discussed in the given context, the required combination of experimental and theoretical approach unequivocally proving a Lifshitz transition has (to our knowledge) not been published until 1988 when Varyukhin *et al.* attributed their results on $\mathrm{Cd}_{1-x}\mathrm{Mg}_x$ alloys to an ETT [23–27].

However, since that time very precise measurement equipment and lowest experimental temperatures became more widely available, hence the observations of Lifshitz transitions are still challenging, but easier to be carried out nowadays. Correspondingly, in the last years such transitions were detected in several compounds using high resolution measurements under extreme conditions.

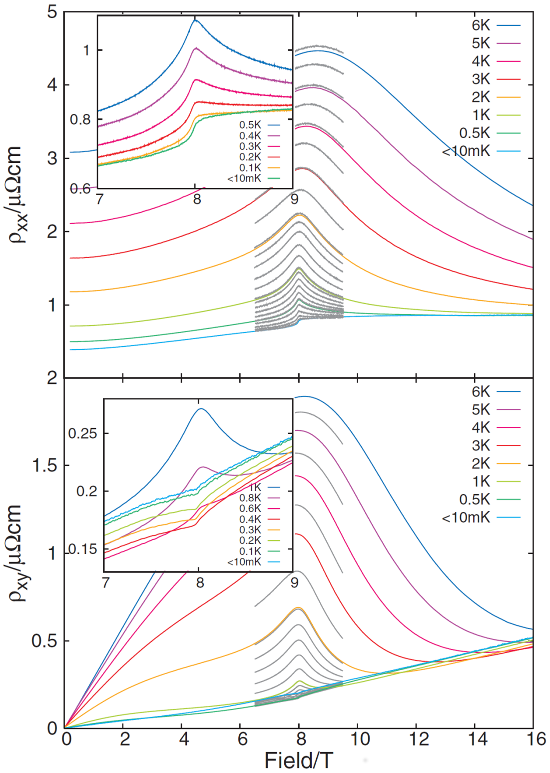

Figure 3.3: Resistivity and Hall effect of $CeRu_2Si_2$ across the magnetic field induced Lifshitz transition down to very low temperatures [16].

Some examples of experiments performed on $CeRu_2Si_2$, Na_xCoO_2 and URhGe in order to clarify the details of a changing Fermi surface in these compounds are depicted in Figs. 3.3, 3.4 and 3.5. All three materials are candidates for the existence of Lifshitz transitions and are discussed in this context. In the case of $CeRu_2Si_2$, among other techniques, very precise resistivity and de Haas-van Alphen data at lowest temperatures, as well as advanced theoretical calculations were discussed and compared (for details see Ref. [16] and Refs. therein). The situation in Na_xCoO_2 is similar although in this compound the Lifshitz transition is driven by band-filling due to an increasing x instead of an applied magnetic field [14]. For URhGe the Fermi surface vanishes as a function of an applied magnetic field similar to $CeRu_2Si_2$. Experimental evidence for this interpretation is found in very precise resistivity measurements at very low temperatures where a detailed analysis of quantum oscillations was performed and compared to a model for a shrinking Fermi surface [18]. We will not discuss the above cases in more detail since the physical mechanisms in these materials are different from UPd_3, $U(Pd_{1-x}Pt_x)_3$ and UPt_2Si_2. However, these materials indicate the large efforts necessary to clarify the mechanisms for changing Fermi surfaces and to prove or disprove the existence of a Lifshitz transition.

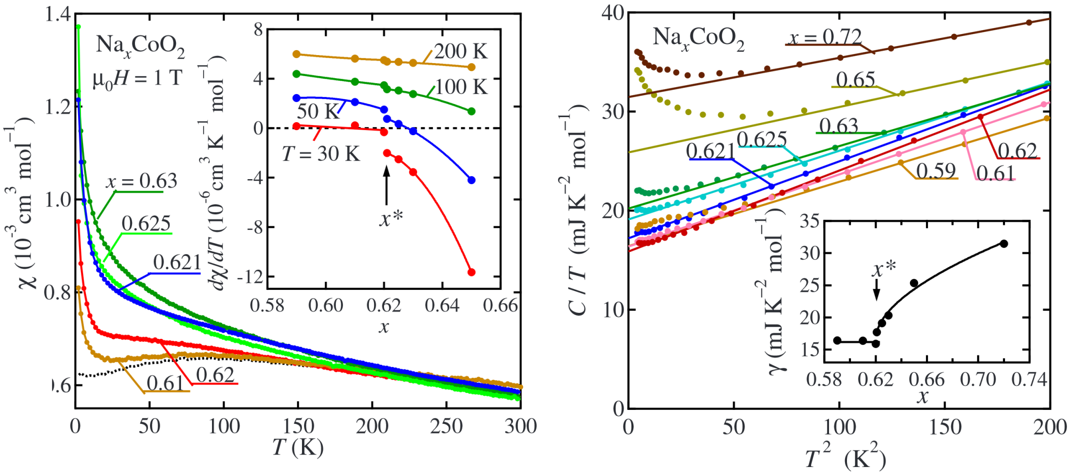

Figure 3.4: Susceptibility (left) and specific heat (right) of Na_xCoO_2 for different x close to the composition induced Lifshitz transition at $x^* \approx 0.62$. Insets depict the temperature derivative and the γ coefficient with x^* indicated [14].

Along with these three exemplary compounds in a few other materials discussed in the context of heavy fermions Lifshitz transitions were found or proposed, that are, for instance, CeBiPt, $Gd_{1-x}Y_x$, $YbRh_2Si_2$, UPd_2Si_2. However, the experimental evidence for such kind of transition is much less clear in the latter cases [13, 15, 17, 19, 20].

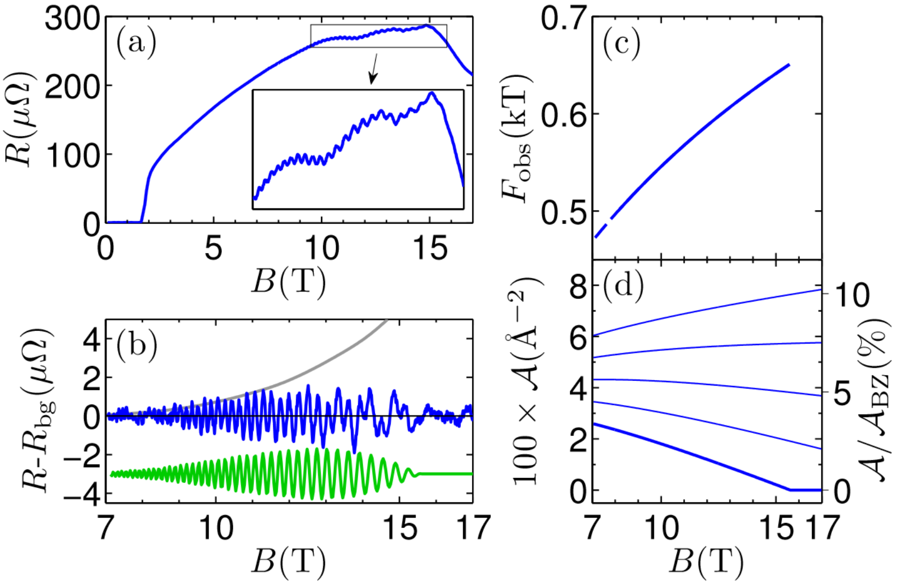

Figure 3.5: Experimental evidence for a magnetic field induced Lifshitz transition at $B \approx 15$ T in URhGe. (a) Magnetic field dependent resistivity at $T = 20$ mK, inset shows the quantum oscillations in more detail. (b) Residual oscillations after subtracting a smooth background (blue) and model calculations (green). (c) Observed quantum oscillation frequency. (d) Forms of the magnetic field dependent Fermi surface area that are consistent with $F_{\mathrm{obs}}(B)$ [18].

4 UPt_2Si_2

Throughout the last decades, ternary intermetallic uranium compounds of composition UT_2M_2, with T a transition metal and M either Si or Ge, stood in the focus of intensive research efforts. In this field, there are various topics that are addressed in experimental and theoretical studies. For instance, the heavy fermion superconductor URu_2Si_2 [28] exemplifies the topic "hidden order" [29], which presently is dicussed in terms of spin nematic phases [30, 31]. The very same material is also a prime example for the observation of exotic field induced phases [32–34], and whose microscopic nature have not been resolved so far. The series of materials UT_2Si_2 has served as testing ground for advanced band structure calculations [35], with experimental tests from many different authors (see for instance Refs. [19, 36–41] and references therein). URh_2Ge_2 and UPt_2Si_2 have served as model materials to study disorder effects in correlated electron materials [42–45]. Especially for the latter compound, UPt_2Si_2, the reinvestigations in the Refs. [45–47] brought up the issue of the degree of f electron localization in U compounds, a topic also discussed in context with other uranium intermetallics such as the heavy fermion superconductors UPd_2Al_3 or UPt_3 [48–53].

For UPd_2Al_3 already a short time after discovery of the system the concept of different degrees of localization of the f electron system was formulated [54, 55]. In contrast, UPt_2Si_2 was considered to be one of the rare examples of uranium intermetallics with strongly localized f electrons, even allowing to describe the material properties based on a well defined crystal field scheme [56–58]. This way, it was accounted for the temperature dependence of the susceptibility and the high field magnetization at lowest temperatures.

Recently, we have presented detailed high field studies and given strong arguments against the localized crystal electric field model of UPt_2Si_2 [59, 60]. Here, we now propose that UPt_2Si_2 has indeed to be treated as an itinerant system. This thesis is not only supported by the discovery of the field induced phases in UPt_2Si_2 but is now emphasized by initial band structure calculations on this compound taking into account the possibility of delocalization [61]. Thus, we associate the high field phase transitions in UPt_2Si_2 with Lifshitz transitions. Altogether, we believe that with the experimental properties and initial band structure calculations presented so far UPt_2Si_2 is a candidate material to be studied in detail by more advanced band structure calculations, to verify or disprove the phenomenological descriptions put forth by experimentalists.

4.1 Physical properties

UPt_2Si_2 was shown to crystallize in the tetragonal $CaBe_2Ge_2$ structure (space group $P4/nmm$) as it is depicted in Fig. 4.1 [62]. Due to the lattice parameter anomaly at $T \approx 100$ K depicted in Fig. 4.2 the system contains a high level of static strain-induced disorder at low temperatures. This disorder is reflected by extraordinary large displacement parameters in neutron diffraction data refinement with the displacement parameters being largest for the Pt(2) and Si(2) sites in the a-b-plane. The size of the ellipsoids in Fig. 4.1 reflects the magnitude of this displacement parameters to visualize the distribution of the disorder in UPt_2Si_2 [45].

Below $T_N = 32$ K the system orders antiferromagnetically with ferromagnetically coupled layers in the ab plane, antiferromagnetic stacking of these layers along the c axis and a moment of about 2 μ_B per ura-

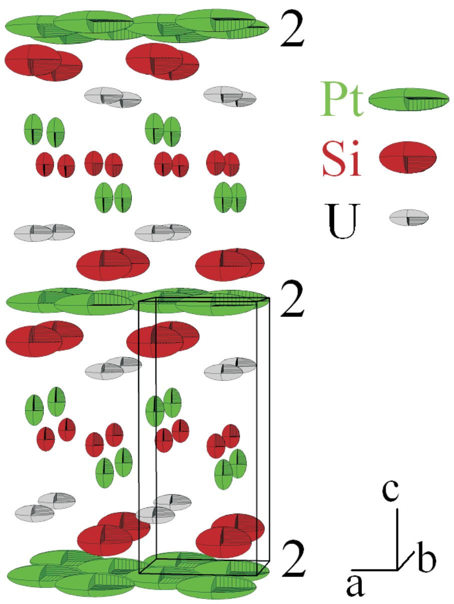

Figure 4.1: Tetragonal crystal structure (space group $P4/nmm$) of UPt_2Si_2 in ellipsoidal representation with the unit cell indicated (for details see text) [45].

nium atom at 4.2 K pointing into the c direction [45, 57, 63, 64]. The linear term of the specific heat was reported to $\gamma = 32$ mJ mole^{-1} K^{-2} indicating a moderate mass enhancement of the electrons [57].

Various physical properties of UPt_2Si_2 in low magnetic fields, such as susceptibility, magnetization and specific heat, were described in terms of a crystal electric field scheme within mean field approximation even though the calculated magnetic moment of $\approx 2.9\ \mu_B$ per uranium atom in this model is much larger than the experimentally observed one [45, 56, 57, 63, 64]. Further, in high field magnetization measurements shown in Fig. 4.3 carried out by Amitsuka *et al.* [58], besides of the discrepancies in the magnitude of the magnetic moment, additional multistep-like fine structures together with hysteresis were observed. Still, the authors concluded that the CEF model qualitatively is correct and that the observed discrepancies could result from not taking

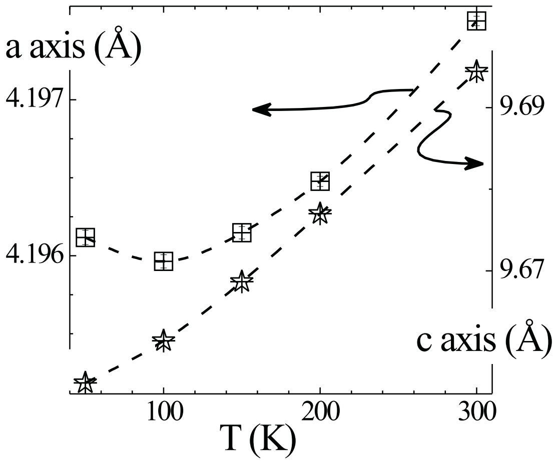

Figure 4.2: Temperature dependence of the *a* and *c* lattice parameters in UPt_2Si_2 [45].

into account hybridisation effects between 5*f* and conduction electrons in the CEF modelling [58].

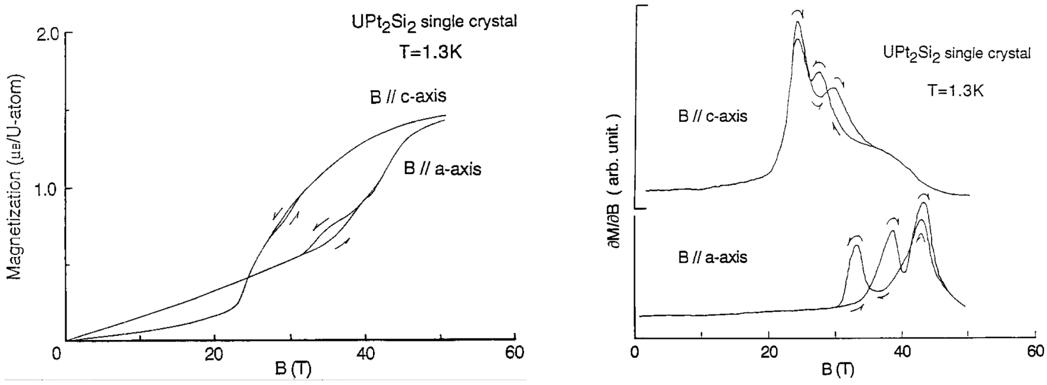

Figure 4.3: Field dependent magnetization and susceptibility of single crystalline UPt_2Si_2 measured by Amitsuka *et al.* [58].

In new high field magnetization measurements we could reproduce experimental data from Amitsuka *et al.*. However, in a comparison of this data to the magnetization expected in a CEF scheme as proposed by Nieuwenhuys as depicted in Fig. 4.4 we only find partial agreement up to magnetic fields of 20 T. In higher magnetic fields along the *a* axis we find a step-like hysteretic area around 42 T, this in contrast to the continuous increase of the magnetization predicted by the model. Furthermore, along the *c* axis we observe a two-step structure with hysteretic regions and a strong deviation of absolute values from the model. Thus, in contrast to Amitsuka *et al.*, based on our new high field magnetization data and the comparison of measured data to the calculated magnetization within a CEF scheme as depicted in Fig. 4.4, we have concluded that these data do not support a CEF modeling of UPt_2Si_2 although our experimental data agree well with Amitsuka *et al.* [59].

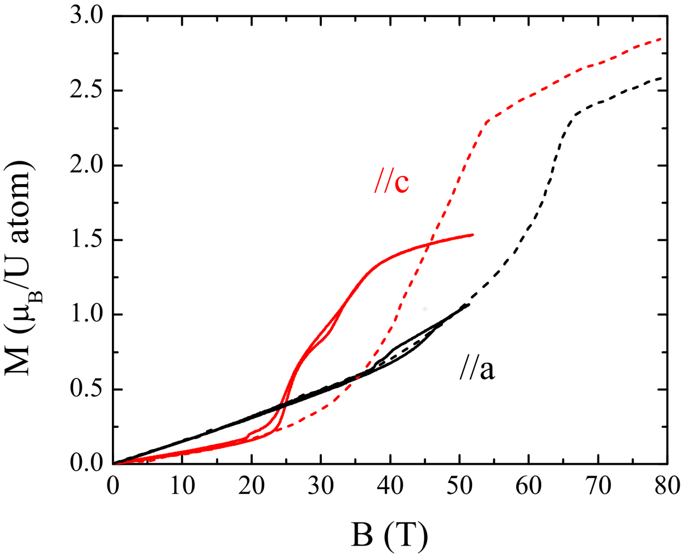

Figure 4.4: Comparison of the high field magnetization of UPt_2Si_2 at 1.5 K for both crystallographic axes. Solid lines are our new high field data, dashed lines are calculated values within a CEF scheme according to Nieuwenhuys [56, 59, 65].

Recently, UPt_2Si_2 was reexamined in the context of disorder affecting the electronic properties of *f* electron intermetallics [45]. Here, it was demonstrated that the electronic transport along the *c* axis can be described by localization theory at temperatures $T > T_N$, while electron-magnon scattering contributes to the electronic transport in the antiferromagnetic phase. At T_N, a Fermi surface reconstruction, indicated by a maximum of $\rho(T)$ within the ordered phase for the c axis data, occurs. From a comparison of resistivity along the c axis and neutron diffraction the transition temperature was identified in the resistivity as a minimum of $\partial\rho/\partial T$ as shown in Fig. 4.5 [45]. Along the a axis the resistivity is that of a common antiferromagnetic uranium intermetallic with moderate mass enhancement.

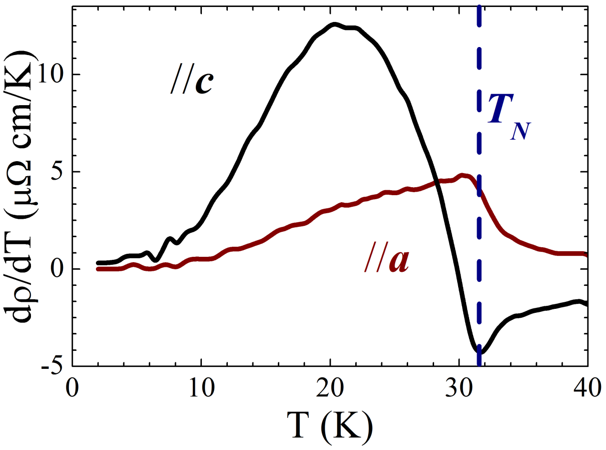

Figure 4.5: Derivative of the resistivity ρ with respect to the temperature for UPt_2Si_2 along the a and c axes with the Néel temperature indicated [45].

Furthermore, using a comparison of the Hall coefficient R_H and the magnetic susceptibility χ as depicted in Fig. 4.6 it was shown that the Hall effect contains a contribution proportional to χ and that the charge carrier density is of the order of one electron per unit cell [45].

Recently, motivated by first published results from this study two independent density functional theory studies were performed on UPt_2Si_2 calculating the system in an itinerant or partially itinerant framework [61, 66]. Both studies independently concluded that contrary to previously published theoretical descriptions UPt_2Si_2 cannot be treated in a completely localized CEF scheme but has rather to be treated as a partially delocalized $5f$ electron system and that the Fermi surface topology in this compound is sensitive to small shifts of the Fermi energy.

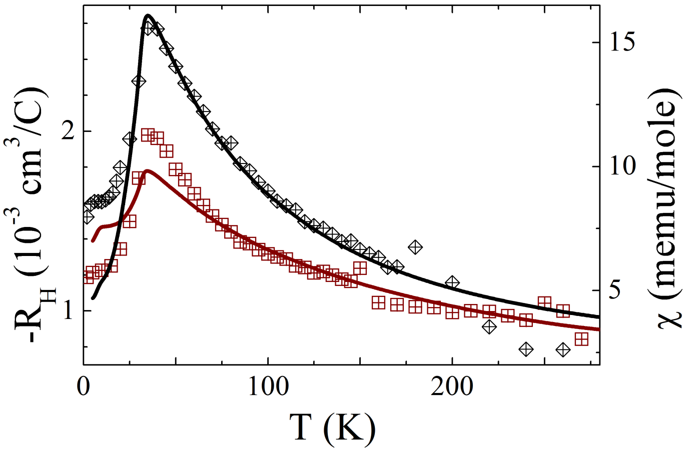

Figure 4.6: The Hall coefficient R_H (symbols) and magnetic susceptibility χ (solid lines) of UPt_2Si_2 along the a (brown) and c (black) axes [45].

In the following, we present a full account of our high field study by discussing field and temperature dependent magnetization and resistivity experiments. From our data we extract the magnetic phase diagram for fields applied along the crystallographic a and c axes and discuss on a phenomenological level possible scenarios to account for the observed physical properties. Consistent with very recent theoretical approaches (Refs. [61, 66]) we finish with our conclusion that UPt_2Si_2 has to be treated as an itinerant system in which at least one Lifshitz transition occurs in high magnetic fields.

4.2 Experimental setup

All measurements presented in this thesis were performed on single crystalline UPt_2Si_2 grown in Leiden using a modified Czochralski method as described in Ref. [67]. The samples are bar shaped with a cross section of 1x1 mm^2 and a length of 3 to 10 mm, with the long side cut parallel either to the a or the c axis. The crystals have been characterized previously in zero magnetic field with neutron diffraction, susceptibility, specific heat, Hall and resistivity measurements (see Refs. [45, 47]). For magnetization, Hall effect and the resistivity measurements shown in Figs. 4.16, 4.17 and 4.26 as-cast crystals were used, while the remaining resistivity measurements were done using crystals that have been annealed for one week at 900°C. We have previously shown that the annealing process does not significantly alter the physical properties of UPt_2Si_2, hence, in terms of the ground-state properties and the behavior in magnetic fields as-cast and annealed material should give the same results [47].

The high field magnetization measurements were carried out in Toulouse at the Laboratoire National des Champs Magnétiques Intenses (LNCMI) as well as the Dresden High Magnetic field laboratory (HLD) in pulsed magnetic fields up to 53 T. A typical setup for the coils providing the magnetic field is described in detail in Ref. [68]. Experimental data were taken by recording and integrating the induced voltage of a small pick-up coil surrounding the sample inside the magnet. Each magnetic pulse was measured twice, with and without the sample mounted. This way, by subtracting both measurements, all additional magnetization contributions from the sample environment are corrected for.

Resistivity data in magnetic fields up to 9 T directed parallel to the applied current and along the crystallographic a and c axes down to 1.8 K were taken in Braunschweig using a standard four-wire ac-technique. Moreover, resistivity in high DC magnetic fields up to 28 T for the same geometry were performed at the Grenoble site of the LNCMI, here using a four-wire lock-in technique. In a second campaign measuring resistivity and Hall effect up to 34 T in static fields (Figs. 4.16, 4.17, 4.20, 4.21 and 4.22) in Grenoble the geometry was slightly modified with the current applied parallel to the basal plane and orthogonal to the magnetic field with the magnetic field applied along a and c axes again.

4.3 Magnetization

Our data from magnetization measurements at the LNCMI and the HLD cover the temperature range from 1.5 to 35 K, *i.e.*, from the AFM ordered phase in zero magnetic field into the paramagnetic regime above T_N. Both data sets contain the same significant field dependent features. Furthermore, at lowest temperatures the data agree well with low temperature data from Amitsuka *et al.* [58]. In the Figs. 4.7, 4.8 and 4.9 we show the data taken at the LNCMI, which cover a broader temperature range than the HLD data [60].

First, in Figs. 4.7 and 4.8 the absolute magnetization M for both crystallographic axes is depicted. Further, Fig. 4.9 contains the field derivative $\partial M/\partial B$ for the c axis to emphasize the most important features along this direction.

Along the a axis at a high temperature of 35 K (*i.e.*, above the Néel temperature), we see an almost linear dependence of $M(B)$ up to the highest fields, as one expects for an unsaturated paramagnet. On reducing temperature to 20 K, thus in the AFM phase, the magnetization is slightly reduced but qualitatively unchanged. In contrast, upon further reduction of temperature a metamagnetic-like transition appears, which in addition exhibits hysteresis in the field range $\approx$ 35 to 48 T. Measurements at additional temperatures reveal that this distinct change of the

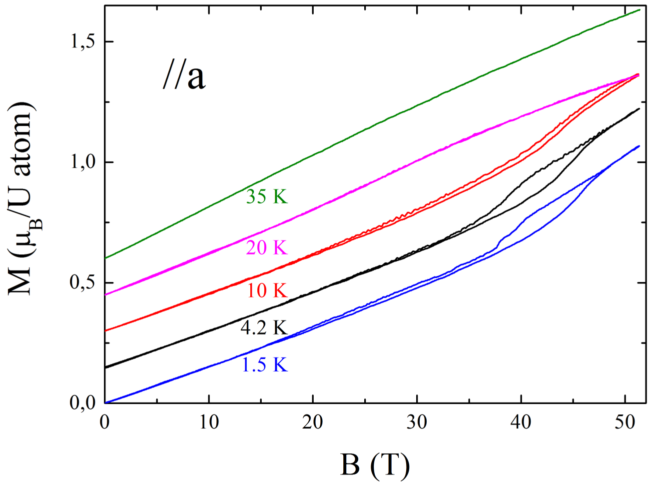

Figure 4.7: Magnetization $M(B)$ for the a axis of single crystalline UPt$_2$Si$_2$ from measurements in pulsed magnetic fields. Scale applies to 1.5 K data, higher temperature data are shifted by 0.15 μ_B [60, 65].

magnetic behavior sets in between 16 and 20 K.

Along the c axis at temperatures above T_N again we find the expected almost linear $M(B)$ dependence up to the highest fields. However, in contrast to the a axis data, for the c axis there is now a strong reduction of the absolute magnetization at 52 T as the temperature is lowered from 35 K (1.28 μ_B/U atom) to below T_N (here 20 K: 0.56 μ_B/U atom). Except for this difference in absolute values, both curves are qualitatively similar. This is also seen in Fig. 4.9 with the derivatives $\partial M/\partial B$ at 20 and 35 K being almost constant but different in absolute numbers.

Upon further reduction of the temperature a very pronounced metamagnetic-like transition appears around 25 T at 10 K, indicating a qualitative difference between the magnetization curves at 10 and 20 K. This difference is also observed in the derivative $\partial M/\partial B$ (Fig. 4.9), where now a single peak appears. In addition, this metamagnetic tran-

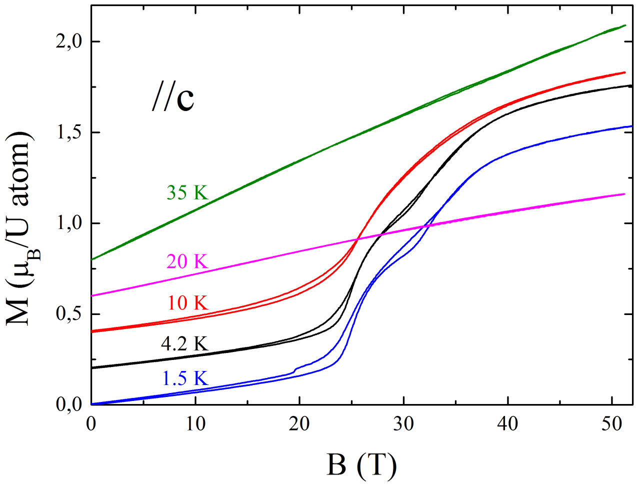

Figure 4.8: Magnetization $M(B)$ for the c axis of single crystalline UPt_2Si_2 from measurements in pulsed magnetic fields. Scale applies to 1.5 K data, higher temperature data are shifted by 0.2 μ_B [60, 65].

sition is accompanied by weak hysteresis in the field range up to ≈ 25 T.

Finally, at even lower temperatures (here 4.2 and 1.5 K) a second metamagnetic-like transition appears, and which again is accompanied by weak hysteresis (for instance, at 1.5 K between ≈ 28 and 33 T). The occurrence of a new field induced phase is also reflected in $\partial M/\partial B$, where now two separate peaks are observed (Fig. 4.9).

A plot of the susceptibility M/B (derived from the field dependence of the magnetization data) along the c axis as depicted in Fig. 4.10 highlights this temperature dependence in high magnetic fields. Up to about 20 T there is a slow monotonic increase with temperature from 1.5 to 35 K. In higher fields of $B \approx 25$ T and temperatures ≤ 16 K the susceptibility is almost constant, but with increased absolute values as compared to 20 T. Between 16 and 20 K at 25 T there is a sudden drop to

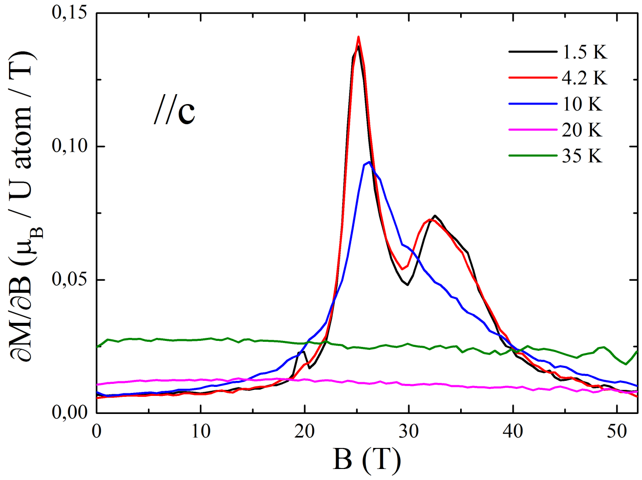

Figure 4.9: Field derivative of the magnetization $\partial M/\partial B$ of UPt_2Si_2 along the c axis as function of the magnetic field B [60, 65].

the low field (20 T) values, indicating a qualitative change in behavior. A similar temperature dependence as in 25 T is observed for an external field of 35 T, but now again with an increase of the absolute values M/B at temperatures $\leq$ 16 K. Further increase of the magnetic field (50 T) does not change absolute susceptibility values within experimental error.

Summarizing our findings, from the magnetization data along the a axis we find a regime with a qualitative change of behavior for fields of the order 40 T at temperatures below $\approx$ 20 K. Furthermore, along the c axis there is evidence for multiple field induced phases. The magnetization (Fig. 4.8) and field dependent susceptibility (Fig. 4.9) attest to phase transitions at around 25 T for temperatures below 20 K, and around 30 T below 10 K. The temperature dependent high field susceptibility (Fig. 4.10) points to phase transitions upon lowering temperature to $<$ 20 K in fields $\geq$ 25 T.

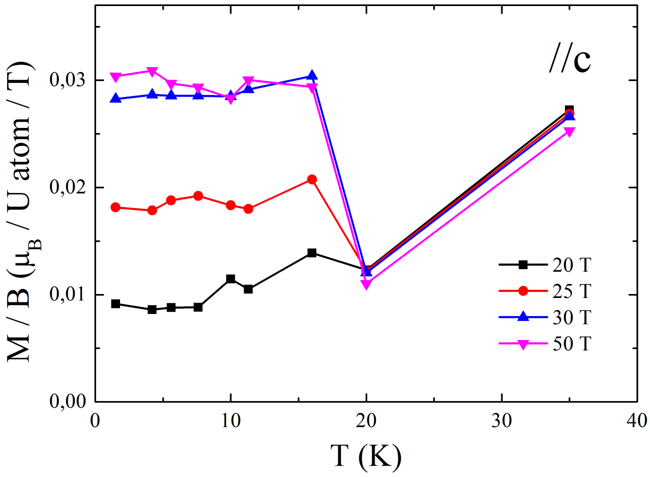

Figure 4.10: M/B of UPt$_2$Si$_2$ along the c axis as a function of temperature for different magnetic fields. Data points are extracted from $M(B)$ measurements as depicted in Fig. 4.8 [60].

4.4 Resistivity

Our resistivity data consists of multiple field and temperature sweeps covering the temperature range from 2 up to 40 K in magnetic fields up to 34 T. Temperature dependent measurements in zero magnetic field nicely reproduce all resistive features previously reported [45, 57, 69]. Due to the intrinsic disorder in UPt$_2$Si$_2$ the absolute values of the resistivity are strongly dependent on the sample used and the actual contact positions of the connecting wires [45]. Therefore, even different measurements of the same crystal in the same setup yield different resistivities when the contacts are renewed between two measurements. Due to this variation of absolute resistivities we have normalized our experimental data of the temperature dependent measurements according to

$$\rho_{norm} = \frac{\rho(T) - \rho_{min}}{\rho_{max} - \rho_{min}}, \tag{4.1}$$

with ρ_{min} and ρ_{max} being the minimum and maximum resistivities in the temperature range 2 to 40 K in zero magnetic field. This normalization was carried out separately for each data set using the corresponding zero field values with the same contact positions. This way, field dependent effects are emphasized in our graphic representations, while the residual resistivity as the most important resistive component independent of field is corrected for in the data. In Figs. 4.11 and 4.12 we show the resulting data for selected fields after the normalization procedure has been performed [60].

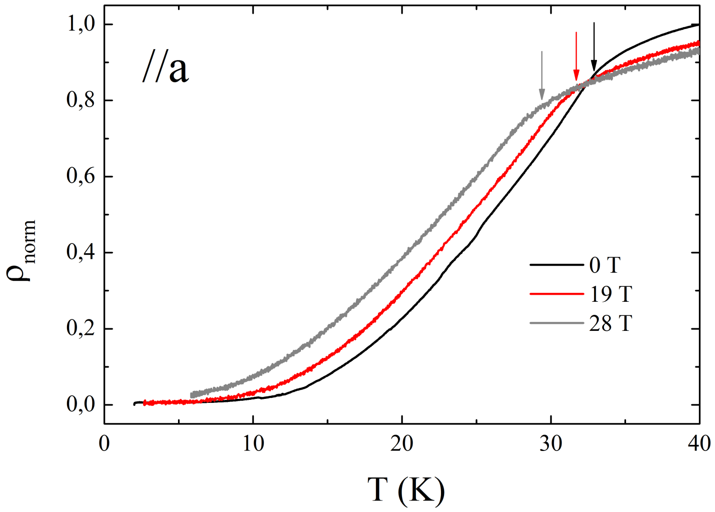

Figure 4.11: Normalized resistivity $\rho_{norm}(T)$ of single crystalline UPt_2Si_2 for selected fields from measurements in static magnetic fields along the a axis as determined using Eq. 4.1. Arrows indicate T_N [60].

For measurements with the field applied along the a axis, the Néel temperature T_N shifts down to lower temperatures with increasing magnetic field, as is typical for the field response of an antiferromagnet. Based on a comparison of in-field with zero field data we find that the Néel temperature can be identified as kink in $\rho_{norm}(T)$, *i.e.*, $\left|\partial^2\rho_{norm}(T)/\partial T^2\right| =$

max. We note that the highest experimentally accessible fields of 28 T and 34 T were not sufficient to reach the field region where a new hysteretic metamagnetic transition appeared in the magnetization. Thus, the magnetoresistivity along the a axis as shown in Figs. 4.13 and 4.16 exhibits a B^2 dependence as expected for an antiferromagnet. In our data minor deviations from this ideal dependence exist. Since in all measurements the temperature was recorded at all times, from a comparison of temperature and resistivity data, we can attribute these deviations to small temperature changes which are caused by the variation of the magnetic field. This temperature variation is depicted in Fig. 4.15 for selected measurements.

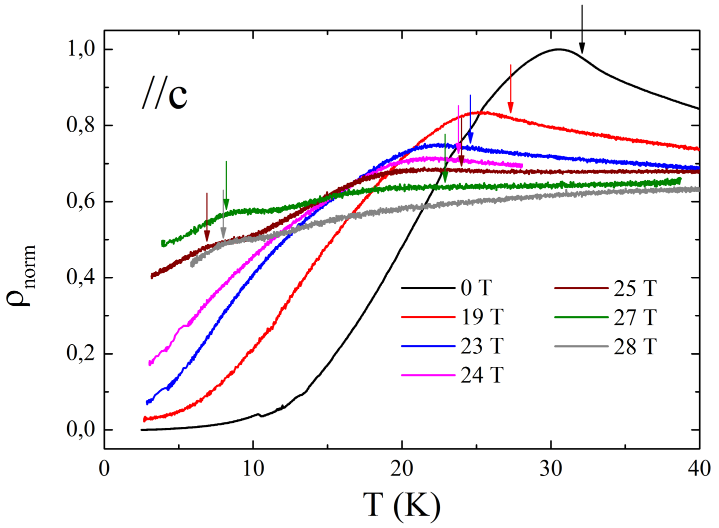

Figure 4.12: Normalized resistivity $\rho_{norm}(T)$ of single crystalline UPt$_2$Si$_2$ for selected fields from measurements in static magnetic fields along the c axis as determined using Eq. 4.1. Arrows indicate T_N and T^* [60].

In contrast to the a axis, along the c axis the antiferromagnetic phase transition at the Néel temperature in zero magnetic field can be identified as the minimum in $\partial\rho/\partial T$ (see Ref. [45]). This minimum is a result of an anomalous and instantaneous increase of the resistivity upon entering the AFM ordered phase due to a Fermi surface reconstruction. Upon increasing the magnetic field this resisitive anomaly, and correspondingly the minimum in $\partial\rho/\partial T$, become less pronounced. Nevertheless traces of the anomaly indicative of the AFM phase transition are visible up to 27 T, with the Néel temperature being shifted from 32 K in zero field to 23 K at 27 T.

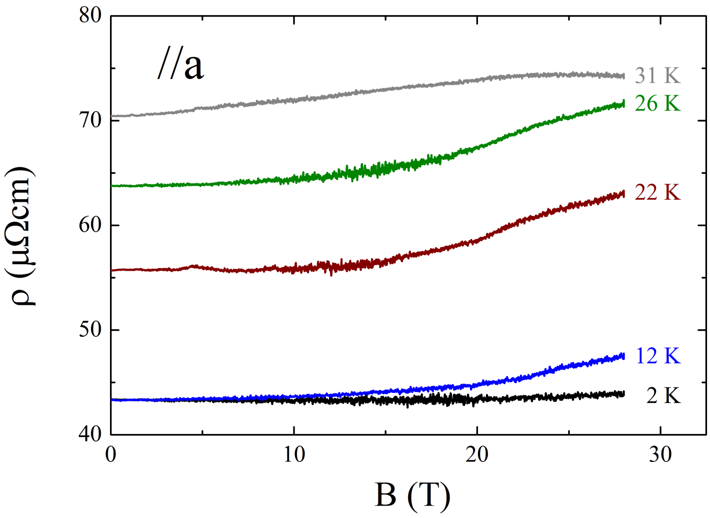

Figure 4.13: Absolute magnetoresistivity of single crystalline UPt_2Si_2 along the a axis for selected temperatures from measurements in static magnetic fields [60].

Furthermore, starting at zero magnetic field and at temperatures below ≈ 13 K, the resistivity first increases with increasing field without qualitative changes up to 24 T. But in higher magnetic fields (here: at and above 25 T) a new and distinct anomaly appears, and which is clearly visible as an additional contribution to the resistivity. The magnitude of this anomaly reaches its maximum at 27 T and decreases upon further increase of the magnetic field reaching the 25 T value at 28 T again. This anomaly is indicative of another phase transition at a critical temperature T^*, which we determine from the condition $\left|\partial^2\rho_{norm}(T)/\partial T^2\right| = max$ and varies between 6.9 and 8.2 K in the field range 25 to 28 T.

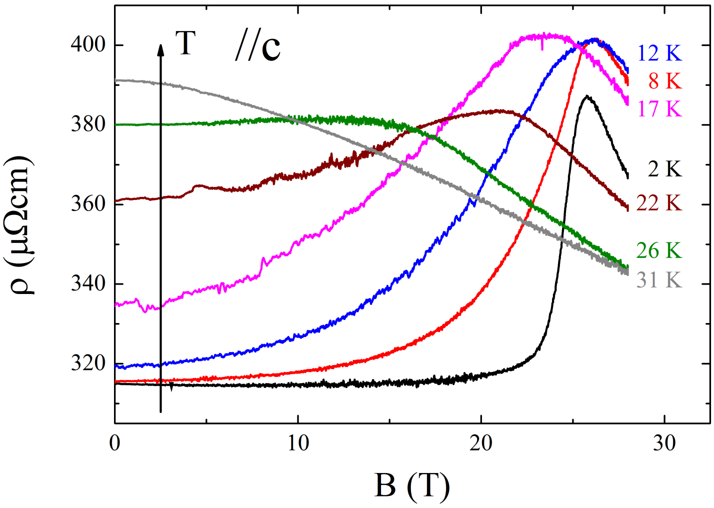

Figure 4.14: Absolute magnetoresistivity of single crystalline UPt_2Si_2 along the c axis for selected temperatures from measurements in static magnetic fields [60].

This additional anomaly also leaves a trace in the field dependent resistivity along the c axis, which is depicted as absolute magnetoresistivity in Fig. 4.14 [60]. At 2 K we first see an almost field independent resistivity up to ≈ 20 T. In higher magnetic fields the resistivity increases, with a peak-shaped field dependence reaching its maximum at 26 T. With increasing temperature this peak is strongly broadened while the overall curve transforms into a monotonously decreasing one at 31 K, close to the ordering temperature.

In order to identify anomalies that could prove or disprove the existence of a magnetic field induced Lifshitz transition in UPt_2Si_2 we have carried out a second set of resistivity measurements at very low temperatures, i. e. 50 mK. In this data depicted in Figs. 4.16 and 4.17, along

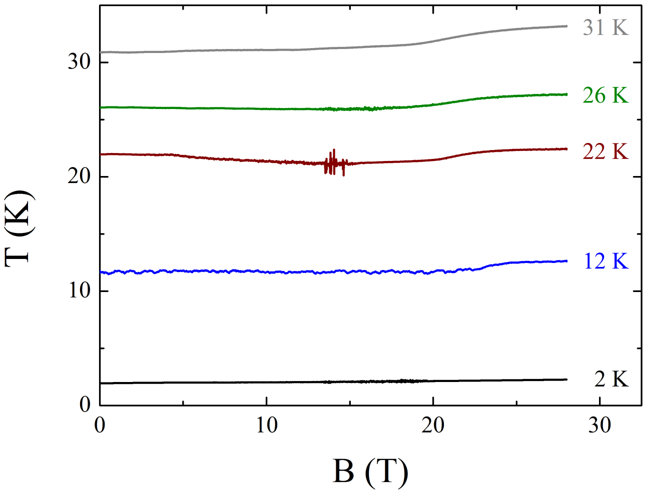

Figure 4.15: Temperature vs. applied magnetic field for the magnetoresistivity measurements shown in Figs. 4.13 and 4.14. Temperature and resistivities along both axes were recorded simultaneously.

the c axis, the same traces of the high field phase transitions are visible. Here, due to experimental limitations, smaller samples without heat treatment have been used to match the cryostats geometric limitations. Additionally, the current has been applied parallel to the basal plane while the magnetic field was aligned orthogonal to the current direction along the a and c axes respectively. This way the setup allowed for simultaneous resistivity and Hall effect measurements and the magnetic field direction (sample orientation) could be changed with a rotatable sample holder without the necessity to remove the sample from the cryostat. The resulting resistivity data has been scaled to match previous data for $I||a$ and $B = 0$ at 2 K for comparability. In principle this should give similar results to the data shown in Figs. 4.13 and 4.14 since the annealing process does not alter the physical properties significantly and a possible Hall voltage due to the rotated current direction can not be detected in this experiment [47].

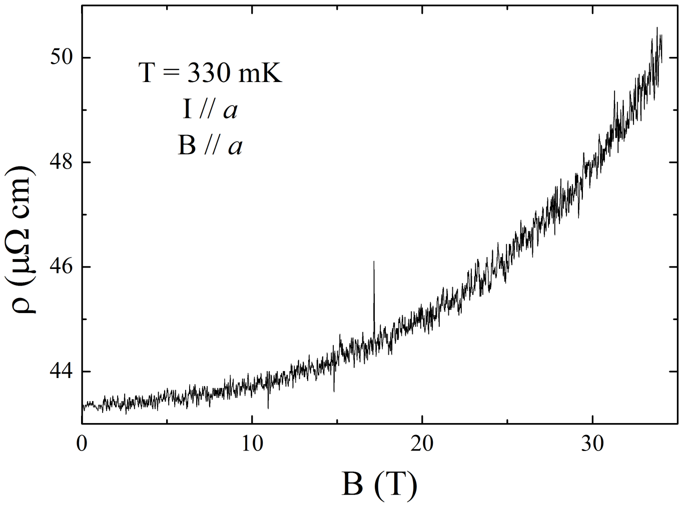

Figure 4.16: Magnetoresistivity of single crystalline UPt_2Si_2 along the a axis at 330 mK from measurements in static magnetic fields.

For the data taken with the magnetic field applied along the a direction this is true except for a stronger absolute increase in resistivity. However, since the absolute values are strongly dependent on the contact positions as described above and qualitatively no differences are observable this data nicely reproduces previous results. In contrast, when the magnetic field is applied along the c axis with the current flowing in the basal plane we again find a broad maximum indicating a phase transition. However, the shape of the maximum is modified being a tilted plateau in the field range $\approx$ 26 - 32 T here. But now we additionally observe hysteresis at all temperatures up to 2 K which was not present in the measurements on annealed samples with $I \| c$. Moreover, above $\approx$ 32 T this hysteresis vanishes or becomes very small. Furthermore, upon cooling below $\approx$ 530 mK multiple steps appear in the downsweeps with the discontinuities appearing at higher fields for lower temperatures. We will discuss these remarkable discrepancies between the two sets of magnetoresistivity data more detailed in the context of the magnetic phase diagram below.

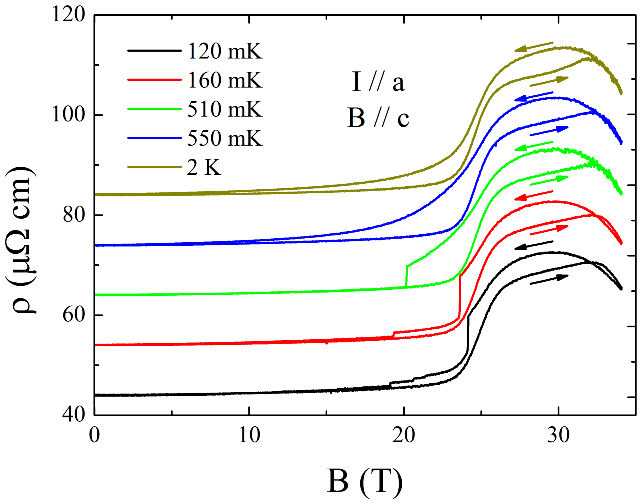

Figure 4.17: Magnetoresistivity of single crystalline UPt2Si2 with current applied along the *a* and magnetic field applied along the *c* axis at very low temperatures. Scale applies to 120 mK data, higher temperatures are shifted by 10 $\mu\Omega$cm for clarity. For details see text.

The mechanisms for the temperature dependence of the resistivity of magnetic materials such as UPt$_2$Si$_2$ are electron-electron ρ_{el-el}, electron-magnon ρ_{el-mag} and electron-phonon scattering ρ_{el-ph},

$$\rho(T) = \rho_0 + \rho_{el-el} + \rho_{el-mag} + \rho_{el-ph}, \tag{4.2}$$

with ρ_0 as the residual resistivity. Especially, for the *c* axis data on UPt$_2$Si$_2$ at low temperatures we have demonstrated that electon-phonon scattering can be neglected to first approximation, thus leaving electron-electron and electron-magnon scattering in the resistivity to be accounted for as described in Eq. 4.3 (Ref. [70]):

$$\rho(T) = \rho_0 + AT^2 + \frac{DT}{\Delta}\left(1 + 2\frac{T}{\Delta}\right) e^{-\frac{\Delta}{T}}. \qquad (4.3)$$

Here, AT^2 reflects electron-electron-scattering, while the exponential term covers scattering due to magnons which are excited across a spin wave excitation gap Δ.

We have used this function to fit our experimental data along the a and c axes in the range up to $\frac{2}{3} \times T_N$ for fields up to 9 T, and up to $\frac{1}{3} \times T_N$ for higher fields, with the upper temperature limit variable to account for the decrease of T_N with magnetic field. Although Eq. (4.3) a priori is only valid in the low temperature limit ($T \ll T_N$), the fitted parameters do not change significantly upon increasing the temperature range of the fit while the accuracy clearly is improved. Thus, effectively for UPt_2Si_2 Eq. (4.3) can also be applied at higher temperatures.

From our fits we observe that the free parameter A is quite small, randomly being positive or negative and consistent with being zero within calculated errors. This is also consistent with the moderate mass enhancement in the specific heat ($A \propto \gamma^2$). In effect, electron-electron scattering accounts only for less then 10% of the temperature dependence of $\rho(T)$. Therefore, we approximate this parameter by fixing it at zero, a condition that does not alter the other fit parameters significantly. Also, this assumption is consistent with the data analysis previously carried out in zero magnetic field, where the resistive contributions from electron-electron scattering turned out to be rather small [45]. Correspondingly, from our fits we obtain the field dependence of the spin wave excitation gap Δ, which is depicted in Figs. 4.18 and 4.19. In these fits, the prefactor D also exhibits a field dependence, so fit parameter interdependency might be an issue here, and which gives rise to some uncertainty in the determination of Δ as indicated in the plot by the large error bars.

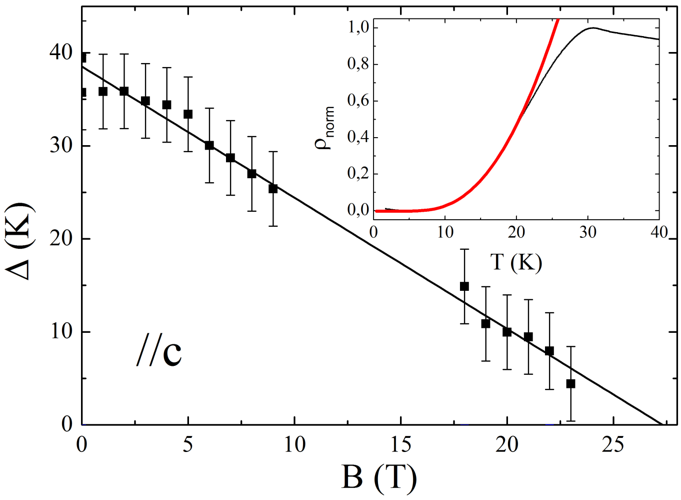

Figure 4.18: Temperature dependence of the spin wave excitation gap Δ of UPt_2Si_2 from fits of Eq. 4.3 to the experimental resistivity data along the crystallographic c axis. The line is a guide to the eye and indicates the disappearance of the gap around 27 T. The inset shows an exemplary fitted curve (red) for zero field data (black) [60].

Keeping in mind this uncertainty, our analysis essentially yields a suppression of the spin wave excitation gap $\Delta(B)$ with applied magnetic field. From Figs. 4.18 and 4.19 we conclude that the spin wave excitation gap closes at around 27 T and 47 T for the c and a axes respectively. In other words, the field dependent resistivity data $\rho(T)$ of UPt_2Si_2 suggests that the zero field spin excitation gap Δ dissappears in that field range, where from the resistivity and magnetization we have established the appearance of new field induced phases.

However, as a note of caution, the analysis of the a axis data in fact is more intricate. In Ref. [45] it was demonstrated that for both a and c axes the resistivity in the AFM state can be described using Eq. 4.3. However, since there is no maximum in $\rho(T)$ just below T_N for the resistivity along the a axis, a priori there is no fundamental argument to prove that this assumption is correct and the description with Eq.

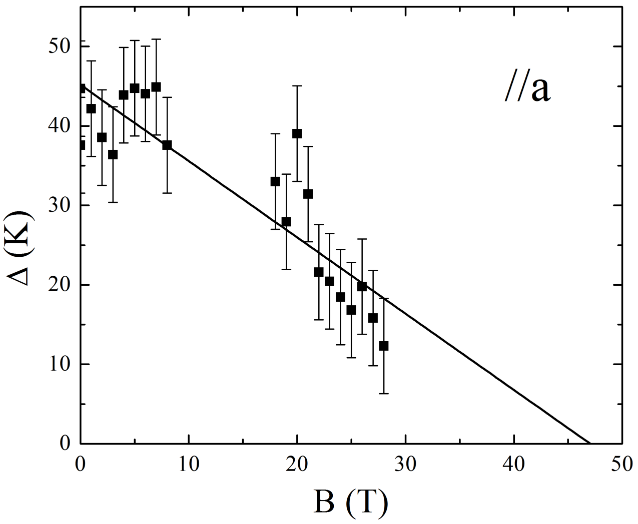

Figure 4.19: Temperature dependence of the spin wave excitation gap Δ of UPt_2Si_2 from fits of Eq. 4.3 to the experimental resistivity data along the crystallographic a axis. The line is a guide to the eye and indicates the disappearance of the gap around 47 T.

4.3 is valid. Alternatively, it could be assumed that the temperature dependence of $\rho(T)$ below T_N is the result of electron-magnon scattering without excitation gap, and which is parameterized by (neglecting again phonon scattering)

$$\rho(T) = \rho_0 + AT^2 + BT^x. \tag{4.4}$$

Here, x is an exponent depending on the type of magnetic fluctuations (for instance, according to Ref. [70], $x = 2$ for ferromagnetic and $x = 5$ for antiferromagnetic fluctuations). In this situation, for the a axis data we have additionally carried out a second type of analysis by parameterizing our data utilizing Eq. 4.4. Both types of fits reproduce the experimental data equally well, therefore we cannot draw definite conclusions about the possibility of a field dependence of the various parameters in the Eqs. 4.3 or 4.4 along the a axis.

4.5 Hall effect

The Hall effect data has been measured in DC magnetic fields up to 34 T in a dilution cryostat at different temperatures in the range 50 mK to 2 K. Due to the sample geometry relatively high currents of 500 μA (lowest temperatures) and 1 mA (higher temperatures) were necessary to produce measureable Hall voltages. For lowest temperatures, these currents resulted in equilibrium sample temperatures of $\approx$ 50 and 150 mK significantly above the base temperature of the cryostat at $\approx$ 10 mK. However, since sample, sample holder and connecting wires were immersed in the liquid Helium mixture still a homogenuous and stable temperature was obtained. Data was taken for both polarities ($\pm B$) of the magnetic field and the Hall voltage U_H has been calculated from the measured Signal U_S according to

$$U_H(B) = \frac{1}{2}\left(U_S(B) - U_S(-B)\right). \tag{4.5}$$

This way interfering signals with $U_S(B) = U_S(-B)$, i.e. from a resistive contribution due to imperfect contact alignment, are corrected for. We do not find any temperature dependence in the Hall signal up to the highest experimental temperature of 2 K and except for increased noise levels at lowest temperatures due to the reduced current all data show the same features.

With the magnetic field applied along the a axis depicted in Fig. 4.20 we see a linear Hall signal with increasing field up to the highest accessible fields of 34 T. From a linear fit through the origin we find a constant Hall coefficient of $R_H = 5.35 \cdot 10^{-4}\,\mathrm{m^3C^{-1}}$.

Contrary, as it is depicted in Fig. 4.21, for the magnetic field applied along the c axis, the Hall signal is only linear in the AFM ground state up to $\approx$ 23 T. For higher fields, we observe a significant increase of U_H from 2.9 mV at 23 T to 5.1 mV at 26 T with another subsequent linear regime

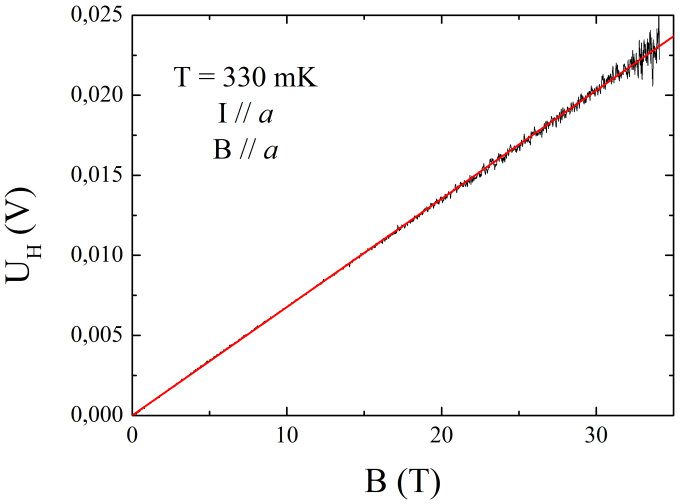

Figure 4.20: Hall effect data for a magnetic field applied along the a axis. The red line is a linear fit through the origin.

from 26 - 32 T and a final reduction of the Hall signal for $B > 32$ T. From linear fits through the origin in both linear regimes ($B < 23$ T and 26 T $< B < 31$ T) we find Hall coefficients of $R_{H,1} = 1.16 \cdot 10^{-4}\,\mathrm{m^3C^{-1}}$ and $R_{H,2} = 1.83 \cdot 10^{-4}\,\mathrm{m^3C^{-1}}$.

Thus, we find distinct changes in the Hall signal along the c axis at $B \approx 24$ T and $B \approx 32$ T where we have found anomalies indicating phase transitions in the magnetization and resistivity data. Since it was shown previously that an anomalous contribution to the Hall signal has to be taken into account in UPt_2Si_2 we have parameterized our Hall signal considering the normal (linear) Hall effect together with different models for the anomalous contributions [45]. The contributions taken into account here are (compare Ref. [71]):

(i) a term $\propto M$ taking into account the magnetization of the material

(ii) skew scattering ($\propto \rho M$) and

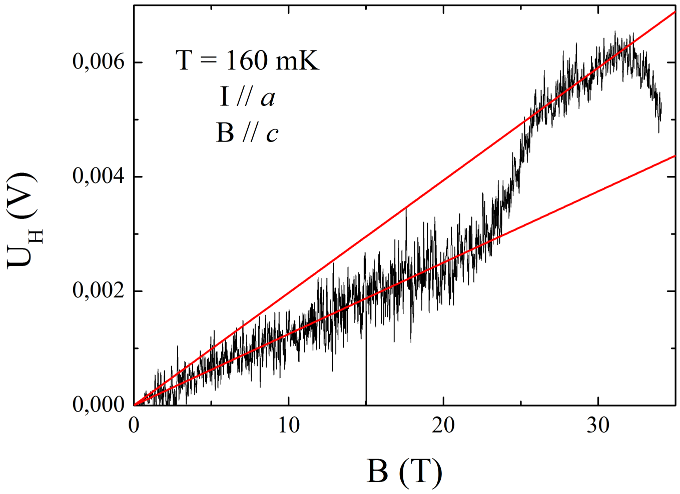

Figure 4.21: Hall effect data for a magnetic field applied along the c axis. The red lines are a linear fits through the origin in the field ranges $B < 23$ T and 26 T $< B <$ 31 T.

(iii) side-jump Scattering ($\propto \rho^2 M$).

Thus, the functions fitted to the total Hall effect for this analysis are

$$U_{H,i} = R_{H,i}B + C_i M(B) \tag{4.6}$$

$$U_{H,ii} = R_{H,ii}B + C_{ii}\rho(B)M(B) \quad \text{and} \tag{4.7}$$

$$U_{H,iii} = R_{H,iii}B + C_{iii}\rho^2(B)M(B) \tag{4.8}$$

which were applied to experimental data at 2 K with only R_H and C coefficients as free parameters. To determine $M(B)$ and $\rho(B)$ for this parameterization field dependent magnetization data from Fig. 4.8 and resistivity data from Fig. 4.17 at 2 K have been fitted with appropriate functions deviating less than 5% (magnetization) and 1% (resistivity) from measured data. Fits of Eqns. 4.6, 4.7 and 4.8 for the field range 0 - 30 T together with a simple linear Hall effect fit for $B < 22$ T are depicted in Fig. 4.22.

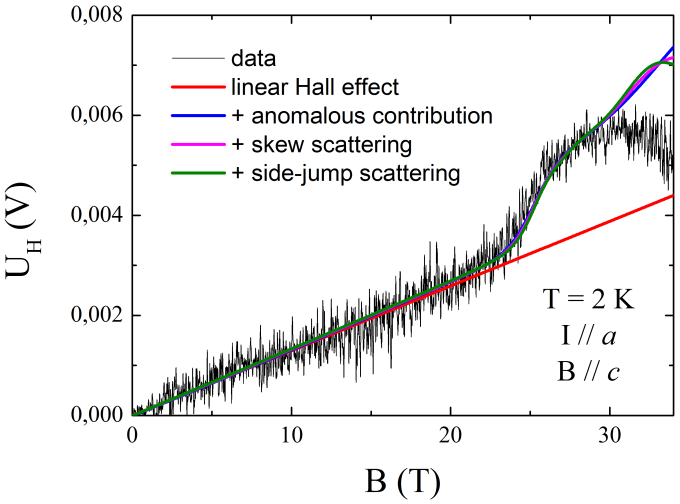

Figure 4.22: Hall effect data for a magnetic field applied along the c axis together with fitted curves for different contributions to the Hall voltage. The red line is a linear fit through the origin up to 23 T. Blue, purple and green lines are combined fits of a normal and an anomalous contribution to the Hall effect for $B < 30$ T; for details see text.

As can be seen all three models that include an anomalous contribution to the Hall effect fit our data equally well up to ≈ 28 T. However, above 28 T all models deviate significantly from the measured data. In particular, all models give a growing and too large Hall signal while the measured Hall voltage decreases. Thus, even a combination of the different models will not be able to account for our measured Hall signal above ≈ 30 T.

4.6 Discussion

Based on the magnetization and resistivity data presented above we can now proceed and construct the magnetic phase diagrams for fields aligned along both a and c axes. Here, one has to keep in mind that experimental features indicating the phase boundaries might be broadened due to the intrinsic disorder in UPt_2Si_2 (see Ref. [45]). The data analysis for the a axis is straightforward and based upon ($i.$) the data $\rho(T)$ up to 28 T and ($ii.$) the data $M(B)$ up to 52 T. From the resistivity we find a continuous suppression of T_N with field B. Further, from the magnetization we can extract the fields B_{a1} and B_{a2} of start and end of the hysteretic regime by determining the fields at which the $M(B)$ data for the field-sweep up and field-sweep down deviate from and join each other, respectively. Using the values $T_N(B)$, B_{a1} and B_{a2}, we arrive at the phase diagram for the a axis as depicted in Fig. 4.23.

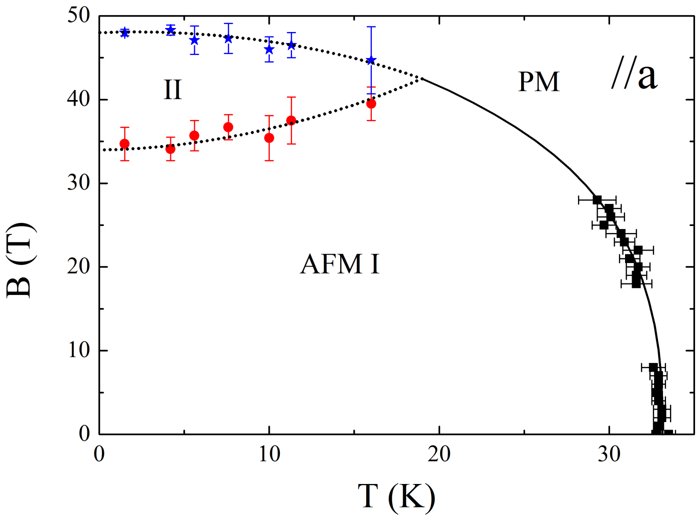

Figure 4.23: Magnetic phase diagram of UPt_2Si_2 for magnetic fields applied along the hard magnetic a axis. Black squares indicate T_N as obtained from the maximum curvature of $\rho(T)$, while red circles and blue stars denote the lower (B_{a1}) and upper (B_{a2}) boundary of the hysteretic area (II); for details see text [60].

Altogether, along the a axis we see a smoothly decreasing Néel temperature defining the AFM phase I with increasing magnetic field up to 28 T, implying that we have the typical phase diagram for an antiferromagnet down to ≈ 18 K. Then, at lower temperatures between 16 K and 20 K, we observe a distinct change in the magnetization with the appearance of a metamagnetic-like transition and hysteresis between field-sweep up und down. Here, the characteristic fields B_{a1} and B_{a2} define the hysteretic region II. The observation of magnetic hysteresis possibly might indicate that the second order AFM phase transition at high temperatures becomes first order at low temperatures/high fields, as it has been observed and calculated previously [72–78]. This possibility is visualized by solid and dotted lines in Fig. 4.23.

At first glance, the phase diagram along the a axis bears close resemblance to those of other antiferromagnets [73] such as $FeCl_2$, $FeBr_2$ or $CoCl_2{\cdot}2H_2O$. In those materials the phase transitions occur from a ground state in which the magnetic field is applied parallel to the easy magnetic axis. For UPt_2Si_2, however, this condition is not fulfilled, since neutron scattering experiments prove the c axis to be the easy axis [57, 79]. To our knowledge in the literature there are no materials or models which exhibit similar characteristics for a geometry of the magnetic field applied along the hard magnetic, in our case the a axis as in UPt_2Si_2.

There have been efforts to calculate the magnetic phase diagrams of an Ising metamagnet in combined longitudinal and transverse fields [80]. These calculations reproduce some features of the phase diagram along the a axis, especially a crossover from a first-to-second order phase transition along the magnetically hard axis. However, such a crossover only occurs in a combination of sufficiently large transverse and longitudinal fields. This is not the case for our measurements on UPt_2Si_2. Here, longitudinal fields along the a axis would only arise from imperfect alignment of the crystal and will be much smaller ($< 5^o$) than discussed in Ref. [80], thus this model cannot account for the observed properties of UPt_2Si_2.

As a last line of thought, we note that for the related uranium intermetallic UPd_2Al_3 a hysteretic metamagnetic high field transition has been observed [81–83]. As yet, a conclusive explanation for such behavior has not been put forth, although it might be speculated that the hysteretic behavior is a result of significant magnetoelastic coupling, thus reflecting a structural response of the system onto a change of the magnetic state. Analogously, it might be argued that for UPt_2Si_2 the observation of hysteresis in the magnetization $\|a$ axis does reflect a first order phase transition associated to magnetoelastic effects. Unfortunately, on behalf of theoretical modelling such issues have hardly been investigated for uranium intermetallics in recent years.

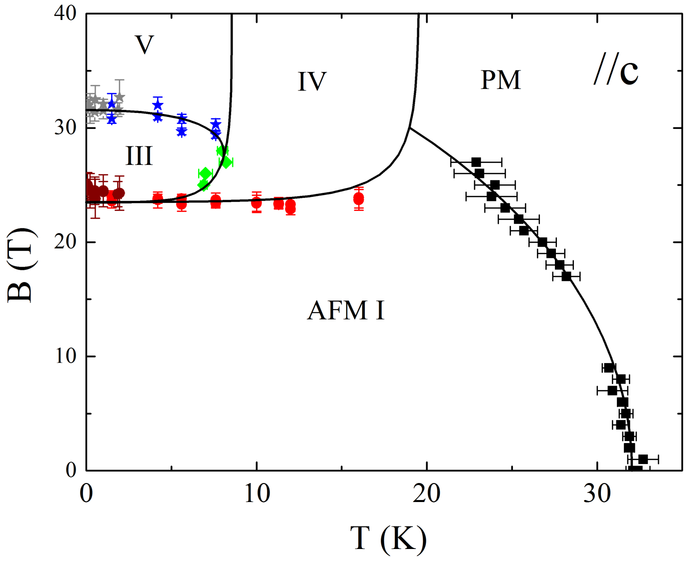

Figure 4.24: Magnetic phase diagram of UPt_2Si_2 for magnetic fields applied along the soft magnetic c axis. Black squares and green diamonds define the transition temperatures T_N and T^* as obtained from resistivity measurements in magnetic fields. Red circles and blue stars indicate the critical fields B_{c1} and B_{c2} of metamagnetic-like transitions as obtained from the maxima in $\partial M/\partial B$. Brown circles and gray stars indicate the same transitions from Hell effect measurements. Solid lines schematically indicate phase boundaries; for details see text [60].

Constructing the magnetic phase diagram for the field B applied along the c axis is a much more complicated task. In a first step, we determine the phase boundary at T_N between paramagnetic and low field antiferromagnetic phase I using the resistivity measurements in magnetic field from the condition $\partial\rho/\partial T = min$ (black squares in Fig. 4.24). As for the a axis, we observe the common behavior of an antiferromagnet with a smooth decrease of T_N down to $\approx$ 23 K with field B up to 27 T. Secondly, from the magnetization $M(B)$ at different temperatures we can extract a first critical field B_{c1} of a metamagnetic-like transition by determining the (first) maximum in the field derivative $\partial M/\partial B$ (see Fig. 4.9), this way defining a phase boundary as indicated by the red circles in Fig. 4.24. A third set of phase boundary data we obtain from the high field ($\geq$ 25 T) resistivity, which as function of temperature shows two transitions. As described above (see Fig. 4.12), this second transition temperature T^* is obtained from the condition $\partial^2\rho_{norm}(T)/\partial T^2 = min$ (green diamonds in Fig. 4.24). Finally, for the magnetization $M(B)$ at $T \leq 8$ K a second metamagnetic-like transition occurs, with a critical field B_{c2} determined from the position of the second maximum in $\partial M/\partial B$ in Fig. 4.9 (blue stars in Fig. 4.24). The critical fields B_{c1} and B_{c2} are also visible in the Hall effect data (see Fig. 4.21) although due to the high level of noise detailed features indicating the phase transition are difficult to determine and estimated errors are large. First, we determine B_{c1} as the middle of the field range where experimental Hall data significantly deviates from the two linear fits in Fig. 4.21 (brown circles in Fig. 4.24). Data points defined this way are in good agreement to features derived from the magnetization previously. Since in our case there is no possibility to predict how to correctly extrapolate $U_H(B)$ for magnetic fields above 34 T we identify B_{c2} with the magnetic field where the deviation between linear fit and experimental data in Fig. 4.21 becomes bigger than the noise level of the Hall signal (gray stars in Fig. 4.24).

In the magnetic field range $B > 28$ T for $T > 2$ K only magnetization data is available, leading to uncertainties in defining the phase boundary lines in very high fields. With the data for the phase diagram $B \| c$ axis put together as described above, we can now draw these phase boundary lines. First of all, there is the boundary between paramagnetism and AFM phase I at comparatively low fields. Secondly, the critical field B_{c1} separates the AFM phase I from a distinct high field state. And thirdly, the data points B_{c1}, B_{c2} and T^* indicate that there is a distinct (antiferromagnetic?) phase III in the field range 24 to 32 T at temperatures $T \leq 8$ K.

The temperature dependent susceptibility in Fig. 4.10 indicates that by changing temperature from 1.5 to 35 K in 20 T only the boundary from phase I to paramagnetism is crossed. In contrast, in a field of 25 T there is the pronounced dip between 16 and 20 K, suggesting that the phase boundary defined by B_{c1} exhibits an upward curvature as indicated by the corresponding line in Fig. 4.24. In other words, in 25 T at 20 K the system resides in the AFM phase I, while in this field at lower temperatures - say at 16 K - there is a new and distinct phase IV. For higher fields (here 35 and 50 T), the temperature dependent susceptibility in Fig. 4.10 suggests that there is a phase boundary between 16 and 20 K, suggesting an evolution of the boundary line as depicted in Fig. 4.24.

Finally, at temperatures ≤ 8 K, there is a sequence of field induced transitions B_{c1}/B_{c2} in the magnetization. It implies that the thermodynamic state at low temperature/high fields (say, at 35 T and 5 K) is different both from that in phase III as in phase IV. The latter conclusion can also be drawn by directly comparing the magnetization for $B \| c$ axis at 4.2 and 10 K in Fig. 4.8. Clearly, there is a qualitative difference in the field dependence of M in high fields. This in turn requires yet another phase boundary to exist just below 10 K in high magnetic fields, and which separates phase IV from phase V. Schematically, we have included this phase boundary line in Fig. 4.24, assuming that the line must be almost vertical, since in our field dependent magnetization measurements we have no indication to cross this line. Altogether, we thus arrive at a very rich high field phase diagram for UPt_2Si_2 along the c axis.

The main concern regarding this scenario is that there is only circumstantial evidence for the existence of the boundary lines defining the phases IV and V, but no direct experimental evidence.

Given this ambiguity regarding phase boundary lines in UPt_2Si_2, one might even speculate that the field derivative of the magnetization $\partial M/\partial B$ along the c axis (Fig. 4.9) contains yet another additional high field transition. This line of thought would be motivated by the rather broad maximum of $\partial M/\partial B$ at 1.5 / 4.2 K in the range 30 to 40 T. It could be argued that the shoulder at 36 T indicates a distinct phase transition, which in some way might connect to one of the other transition lines. However, a quantitative analysis of $\partial M/\partial B$ in this field range turns out to be an awkward procedure, hence we did not follow up on this idea. We note that the uncertainty regarding the evolution of phase boundary lines might also be a result of structural disorder, which is inherent to UPt_2Si_2. As an example, in a related heavy fermion system, UNi_2Al_3, it has been found that the observation of subtleties of the magnetic phase diagram depended on the sample quality [84, 85]. Such issues will be more prominent for an inherently disordered system such as UPt_2Si_2.

Before we discuss the phase diagram along the c axis (Fig. 4.24) in more detail we will reanalyze the magnetoresistivity data shown in Figs. 4.14 and 4.17 in the context of the now determined phase boundary lines since we did not yet use this data to construct the phase diagram. Since all results of the magnetoresistivity measurements with the magnetic field applied along the c axis could be reproduced on different samples with and without heat treatment these remarkable features are an intrinsic property of UPt_2Si_2. For the data set with $B \| c$ and $I \| c$ depicted in Fig. 4.25 we do not cross the III ↔ V phase boundary at B_{c2} but different phase boundaries between the AFM I phase and the high field phases III, IV and PM are crossed. Since these different phase transitions most likely cause different signatures in the magnetoresistivity data they are visualized by different arrows, that is solid, dashed and dotted. It is important to mention that in none of the measurements depicted in 4.25 hysteresis was observed.

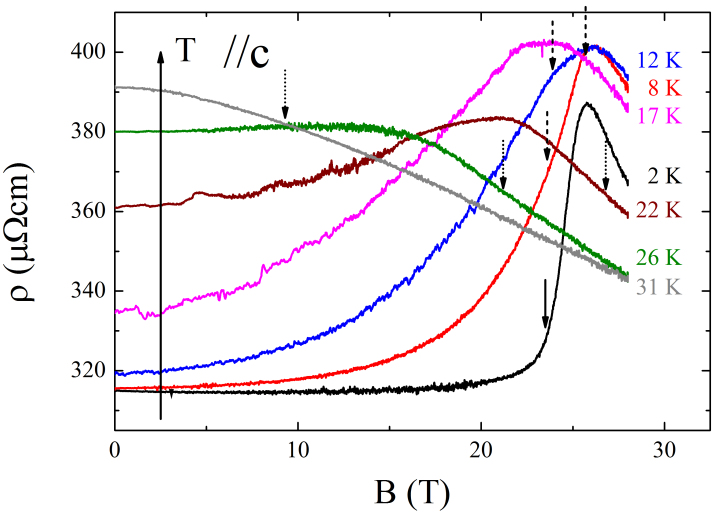

Figure 4.25: Absolute magnetoresistivity of single crystalline UPt_2Si_2 with current and magnetic field applied along the c axis for selected temperatures from measurements in static magnetic fields. Arrows indicate phase transitions according to phase boundary lines in Fig. 4.24. The solid, dashed and dotted arrows indicate the phase transitions AFM I ↔ III, AFM I ↔ IV and AFM I ↔ PM, respectively.

In contrast, for the second set of magnetoresistivity data with $B \| c$ and $I \| a$ shown in Fig. 4.26 we cross the phase boundaries AFM I ↔ III and III ↔ V at B_{c1} and B_{c2}. Since all measurements were done at very low temperatures where the phase boundary line in Fig. 4.24 is almost horizontal the phase transitions occur at $B_{c1} = 23.5$ T and $B_{c2} = 31.5$ T at all temperatures which are indicated by the solid and dotted lines in Fig. 4.26.

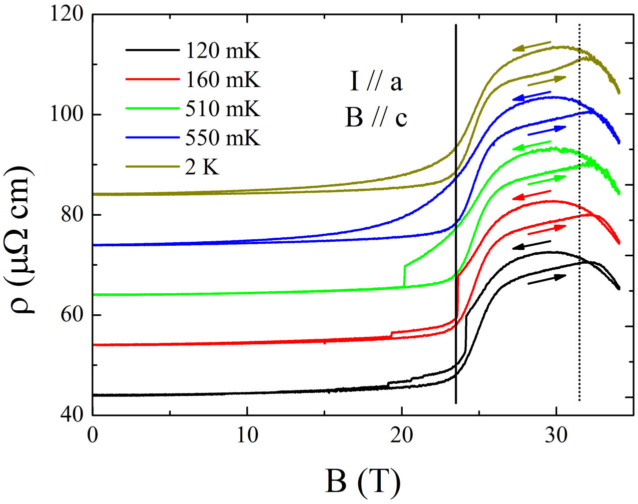

Figure 4.26: Magnetoresistivity of single crystalline UPt_2Si_2 with current applied along the a and magnetic field applied along the c axis at very low temperatures. Scale applies to 120 mK data, higher temperatures are shifted by 10 $\mu\Omega$cm for clarity. The solid and dotted lines indicate the phase transitions AFM I $\leftrightarrow$ III (B_{c1}) and III $\leftrightarrow$ V (B_{c2}) according to phase boundary lines in Fig. 4.24. For details see text.

First of all, consistently in both sets of magnetoresistivity data we find an increasing resistivity within phase III indicating either an increased electron scattering rate or a reduced charge carrier density. Furthermore, from a comparison of both sets of magnetoresistivity data and the phase transition AFM I $\leftrightarrow$ III at B_{c1} we can now identify the phase transition with the maximum curvature of $\rho(B)$, that is $\frac{\partial^2\rho}{\partial B^2} = max$. However, for the phase transitions AFM I $\leftrightarrow$ IV and AFM I $\leftrightarrow$ PM at elevated temperatures the situation is less clear. For the 8 K, 12 K, and 17 K data sets depicted in Fig. 4.25 the AFM I $\leftrightarrow$ IV phase boundary is crossed and the phase transition takes place below (8 K and 12 K) or above (17 K) the maximum in magnetoresistivity depending on the temperature. Thus, it seems impossible to define one unique feature in the magnetoresistivity data to define the AFM I $\leftrightarrow$ IV phase transition. Although, at first glance, there seems to be a small feature indicating the phase transition at 12 K and ≈ 24 T we cannot attribute this kink to the transition since at the same magnetic field the temperature stabilization was insufficient as it is depicted in Fig. 4.15 and thus the kink might as well be a result from the shifting temperature. Therefore we could not construct the AFM I $\leftrightarrow$ IV phase transition from our magnetoresistivity data. For the AFM I $\leftrightarrow$ PM phase transition depicted by the dotted arrows in Fig. 4.25 the situation becomes more consistent again. For all three temperatures depicted the phase transition takes place in a regime where $\rho(B)$ has negative slope and little or no curvature, that is $\frac{\partial\rho}{\partial B} < 0$ and $\frac{\partial^2\rho}{\partial B^2} \approx 0$. Keeping in mind the large slope of the phase boundary in Fig. 4.24 and the error bars in the temperatures defining this phase boundary the dotted arrows indicating the phase transition in Fig. 4.25 might as well be shifted by about 5 T. This possible shift is small enough to rule out $\frac{\partial^2\rho}{\partial B^2} = min$ as a definition of the phase boundary. However, from our data we can speculate that there is a linear regime in $\rho(B)$ in the PM phase at high magnetic fields. Since in our data this is true up to the highest accessible fields, in a second step we could define the magnetic field associated with the phase transition as the magnetic field where experimental data and a linear fit to $\rho(B)$ at highest magnetic fields deviate more than noise level. Due to the high noise levels in $\rho(B)$ and the large uncertainty in defining phase boundaries this way, we did not follow up on this idea in detail. However, regarding all the uncertainties of the definition given above, an estimate of the phase boundary from magnetoresistivity data consistent with our $R(T)$ data depicted in Fig. 4.12 is possible.

Another striking difference between the two magnetoresistivity data sets depicted in Figs. 4.25 and 4.26 is the occurrence of hysteresis in the latter. Generally, hysteresis is connected to a first order phase transition. Since we did not observe hysteresis in field sweeps up to 28 T the phase transition AFM I $\leftrightarrow$ III crossed in these measurements can not cause the hysteresis but the phase transition III $\leftrightarrow$ V at B_{c2} indicated by the dotted line in Fig. 4.26 has to be first order. The same observation of hysteresis and absence of hysteresis can also be made for one single sample in the same experimental setup with field sweeps from zero field into phase V and from zero field to phase III respectively as it is depicted in Fig. 4.27.

Since in high magnetic fields of the order of 30 T strong magnetic forces appear this phase transition might be induced by a magnetoelastic coupling which causes some structural deformation above 32 T. Obviously this field induced first order transition is very stable since at 2 K the hysteresis can be observed down to $\approx$ 10 T with decreasing magnetic field. Similarly we observed hysteresis in the magnetization depicted in Fig. 4.8. Different from the magnetoresistivity data in Fig. 4.26 two almost separate hysteretic regions around 24 T and 31 T are observed in these magnetization measurements for 1.5 K, and which become completely separated at 4.2 K. Around 27 T the difference between increasing and decreasing field is smallest for both measurements, the magnetization at 1.2 K and all magnetoresistivity data depicted Fig. 4.26. Since the magnetization was measured in pulsed magnetic fields while magnetoresistivity data was measured in constant fields we attribute this differences in the observed hysteresis to the different time scales involved. Obviously in the pulsed field measurements where the system is forced into phase V only for several milliseconds the magnetoelastically distorted state of the system is not completely established which results in a reduced hysteresis in these measurements. Contrary, with the DC magnetic fields applied for the magnetoresistivity measurements the system remains in phase V for several minutes allowing the system to relax further to the equilibrium state in this regime which then causes the observed more pronounced hysteresis.

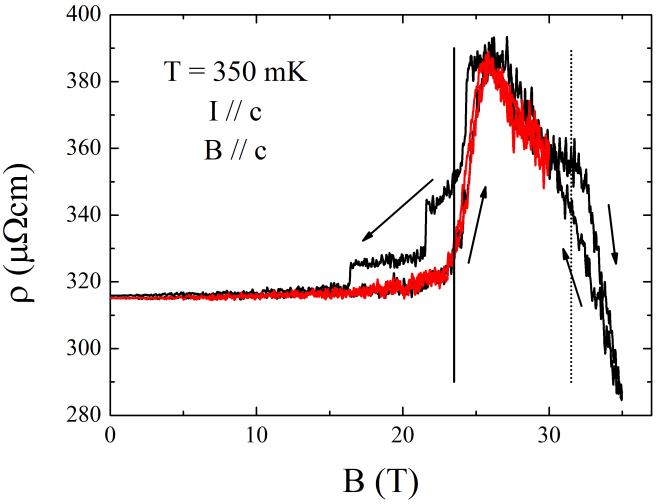

Figure 4.27: Magnetoresistivity of single crystalline UPt_2Si_2 with current and magnetic field applied along the c axis at 350 mK for field sweeps from zero field up to phase III and phase V. Resistivity data has been scaled to match experimental data from Figs. 4.14 and 4.25 at lowest temperatures for comparability. The solid and dotted lines indicate the phase transitions AFM I ↔ III (B_{c1}) and III ↔ V (B_{c2}) according to phase boundary lines in Fig. 4.24. For the black data the field sweep direction is indicated by arrows while for the red data no hysteresis above noise level was observed.

The origin of the steps with decreasing magnetic field below ≈ 530 mK in Figs. 4.26 and 4.27 is not yet completely resolved. Since the steps dissappear at elevated temperatures a thermal mechanism driving the system back to its antiferromagnetic ground state can most likely be ruled out. However, as a tentative explanation, these steps might possibly be caused by remaining strains in the sample due to the magnetoelastic coupling. Since the differences in $\rho(B)$ between increasing and decreasing magnetic field are biggest at lowest temperatures such strains can be expected to be largest at lowest temperatures in the same manner. If these assumptions are valid at some point upon decreasing field the strains become too large and the ground state of the system becomes lowest in energy which causes the system to return to this antiferromagnetic ground state. The successive smaller steps upon further decrease of the magnetic field at lowest temperatures (120 mK and 160 mK) indicate that in some domains of the sample the distorted high field state is more stable and the transition to the ground state occurs at lower fields. Although this explanation is not yet verified by separate measurements it can account for (i) the shift of the first (at highest field) step to lower magnetic fields with increasing temperature (ii) the appearance of consecutive smaller steps and (iii) the transformation into a continuous curve at elevated temperatures (above 530 mK) and is thus consistent with our data.

Further comparison of the magnetoresistivity data sets at 2 K depicted in Figs. 4.25 and 4.26 yields a different shape of the anomalies associated with the high field phases or phase transitions which is a result from the direction of applied current. While for the configuration with $I||c$ depicted in Fig. 4.25 we find a distinct maximum at $\approx$ 27 T within phase III for the situation with $I||a$ depicted in Fig. 4.26 we observe a strong increase of the resistivity upon entering phase III and which is followed by a tilted plateau inside phase III instead of the maximum observed for the previous configuration. Although the data depicted in Figs. 4.25 and 4.26 was measured on different samples we observed the same observation of different shapes of the anomalies in one single sample for different directions of applied current. We attribute these differences in the features indicating the phase transitions to the different physics along the a axis where we find a metallic conducting system compared to the c axis where we find a semimetallic state governed by the potential barriers due to the disordered layers which cause some degree of localization in this direction.

Other uranium and cerium based intermetallics, for instance URu_2Si_2, $CeRu_2Si_2$, UPt_3 and UPd_2Al_3, although they are discussed in a different physical context, show similarities with respect to novel field induced phases and metamagnetism [32, 34, 81–83, 86–90]. Usually these systems are discussed in the context of heavy fermions with a strong itinerant character, while UPt_2Si_2 appears to be much more localized, therefore a direct comparison does not seem to be appropriate. Still, some of the physical properties and features of the phase diagrams resemble those of UPt_2Si_2, possibly indicating a link between the properties of those rather itinerant systems and UPt_2Si_2.

Conversely, a comparison with more localized materials such as the Ising-type metamagnet $FeBr_2$ might yield further insight. At first glance, there appear to be similarities between our data in Fig. 4.24 and that of $FeBr_2$ [91]. Although this system belongs to a class of materials with different underlying physical mechanisms, the phase diagrams resemble each other. In $FeBr_2$ a paramagnetic (PM), an antiferromagnetic (AF) and a mixed phase (AF+PM) exist. If there were analogies between $FeBr_2$ and UPt_2Si_2, these phases would correspond to our phases PM, AFM I and III, with phase III being a mixed phase. For such a mixed phase the magnetization is expected to vary slowly with applied field due to the growth of the volume amount of the phase with higher magnetization at the cost of the second one. In addition, hysteresis should be observed in the whole field range of the mixed phase. Neither is observed in our experiments (Fig. 4.8), where two step-like metamagnetic transitions at the phase boundaries AFM I $\leftrightarrow$ III and III $\leftrightarrow$ V, together with hysteresis over a small field range occur. Therefore, we rule out an Ising-type scenario similar to that in $FeBr_2$ to account for our findings on UPt_2Si_2.

As already discussed for the *a* axis above, the magnetic phase diagram of an Ising metamagnet in longitudinal and transverse fields has also been calculated for the easy magnetic (here *c*) axis [80]. Again, for appropriate parameters, a crossover from a first to a second order phase transition is predicted, together with a phase boundary resembling that of our AFM phase I along the *c* axis. However, the calculations give no indication of additional high field phases as we have detected them above 24 T. Thus this model also cannot account for all the observed properties of UPt_2Si_2.

Rather than using spin reorientation models to account for our observations in UPt_2Si_2, we attribute the observed properties to Fermi surface effects. This interpretation is supported by three facts: First, the distinct increase in $\rho(\mathrm{T})$ just below T_N along the *c* axis indicates Fermi surface effects in UPt_2Si_2 to take place. As well, the second transition in fields $\approx$ 25 T $\|c$ axis observed in the resistivity, together with the signifcantly larger residual resistivity in this field range is indicative of Fermi surface effects. Secondly, as we have pointed out before, the high field magnetization cannot be accounted for by a localized crystal electric field scheme, but which instead must be treated in a more itinerant picture [59]. Thus, Fermi surface effects play a key role in understanding the high field properties of UPt_2Si_2. And third, the striking feature indicative of Fermi surface effects are our Hall effect measurements depicted in Figs. 4.21 and 4.22 where we see a large change of the Hall signal at the phase boundaries AFM I $\leftrightarrow$ III and III $\leftrightarrow$ V which can not be accounted for in a classical model even if we include anomalous contributions to the Hall effect. Thus, the Hall coefficient

$$R_H = \frac{1}{ne} \tag{4.9}$$

is significantly altered at these phase transitions which means, since the electron charge e is constant, that the charge carrier density at the Fermi energy n or $N(E_F)$ has to be modified. A strong modification of $N(E_F)$ on the other hand implies significant changes of the Fermi surface. Such strong changes of the Fermi surface are not necessarily but very likely transitions of the Lifshitz type as discussed in section 3.

An alternative, expanded approach to account for our observations might be found in the concept of different degrees of f-electron localization proposed for some uranium heavy fermions [48–50, 54, 55, 92]. Conceptually, for UPt_2Si_2 we might use this approach to produce a mixture of localized and itinerant views of the electronic structure in correlated electron materials. One might imagine that in band structure calculations some of the f-electron orbitals could be described as being localized, others being itinerant. Recently such calculations were carried out assuming a dual model with two f electrons being localized at the uranium site and one f electron being itinerant. In these calculations it was possible to change the topology of the resulting Fermi surfaces by shifting the Fermi energy only few meV [61]. Such small energy shifts are indeed induced by a strong magnetic field of the order of 30 T and thus a Lifshitz transition in UPt_2Si_2 seems to be very likely from an experimental and theoretical point of view.

Further experimental access to the new found field induced phases in UPt_2Si_2 as well as to gain further insight into the microscopy of these phases is difficult due to the high magnetic fields of up to 50 T involved. Such magnetic fields, with the fast changes in magnetic flux and the small time scales involved in pulsed field measurements, rule out many experimental techniques. Furthermore, quantum oscillation measurements via for instance the de Haas-van Alphen-effect, although usually being a technique applicable in high magnetic fields, can most likely not be carried out in UPt_2Si_2 due to the intrinsic disorder and the corresponding small electronic relaxation times which result in a small Dingle factor. Still, there might be possibilities to gain additional insight into the nature of the field induced phases. First, along the *c* axis (Fig. 4.24) the phases III, IV and V can be accessed by DC magnetic fields in certain laboratories. Here, additional techniques like NMR or specific heat could possibly be used to gain information on the local magnetic structure and on the first or second order nature of the of the observed transitions. Secondly, measurements of the ground state Fermi surface (in the AFM I phase), for instance with ARPES, might allow to observe structures close to the Fermi energy which might produce phase transitions as observed in high magnetic fields.

As conclusion we have performed high magnetic field magnetization, resistivity and Hall effect measurements in pulsed and static magnetic fields up to 52 T. From these measurements we derived the magnetic phase diagrams along the crystallographic *a* and *c* directions. A comparison to other materials and models discussed in the context of metamagnetism was carried out. A close inspection of apparent similarities ruled out that these materials and models could be used to explain the properties of UPt_2Si_2. Instead, we first proposed Fermi surface effects, which could be verified by an analysis of the Hall effect, to produce the field induced phases [60].

Following our argumentation in Ref. [60] Elgazzar *et al.* carried out density functional theory (DFT) calculations of the electronic structure and the Fermi surface of UPt_2Si_2. In their calculations best agreement between experimental data and theory was found for orbitally polarized mostly itinerant 5 f electrons. Furthermore, in some cases they found changes of the Fermi surface topology after applying only a small shift of the Fermi energy [66]. Both conclusions are in perfect agreement to our initial experiments.

In a second set of high magnetic field resistivity and Hall effect measurements we found even more experimental evidence for the important role of the Fermi surface in UPt_2Si_2. In particular, the Hall effect data can not be explained in terms of a constant Fermi surface since all models including an normal and anomalous contributions to the Hall effect fail to explain the high field phase transition at 32 T applied along the c axis. Thus, this Hall effect data can only be explained in terms of a significant change of the Fermi surface.

Motivated by these new high field experiments additional DFT calculations have been performed by Z. Çakir in the group of G. Zwicknagl taking into account the dual nature of the uranium 5 f electrons, that is a combination of localized and itinerant electrons. As in the calculations from Elgazzar *et al.* these calculations are also in best agreement with experimental data for partially itinerant f electrons. And again small shifts of the Fermi energy, corresponding to applied magnetic fields, cause a change of the Fermi surface topology and thus indicate Lifshitz type phase transitions [61, 66, 93].

Thus, we have presented experimental evidence that in contrast to previous publications treating UPt_2Si_2 as a localized system, UPt_2Si_2 is an itinerant system and that Fermi surface effects occur in high magnetic fields. Furthermore, we claim that the high field phase transition at 32 T applied along the c axis unequivocally is a Lifshitz transition and that most likely Fermi surface effects are also involved in the other high field phase transitions. Both claims are clearly supported by two independent DFT studies [61, 66, 93].

5 $U(Pd_{1-x}Pt_x)_3$

UPd_3 and $U(Pd_{1-x}Pt_x)_3$ are examples for a small class of materials where quadrupolar order is observed. In these systems the quadrupolar moments of the electronic wavefunctions can order in a ferro- or antiferroquadrupolar arrangement, as in the case of dipolar (magnetic) order. Well known compouds which exhibit ferroquadrupolar (FQ) order are for example TmCd, TmZn, $TmAu_2$ whereas antiferroquadrupolar (AFQ) order is observed in TMTe, $PrPb_3$, and CeB_6 among others [94–100].

In most systems quadrupolar order does not occur since usually the quadrupolar interactions are weak and thus the stronger dipolar (magnetic) interactions determine the physical properties. Additionally, the quadrupolar ordering temperatures are low due to the weak quadrupolar coupling and often magnetically ordered phases are also found for some temperatures. Furthermore, this leads to a high sensitivity of the quadrupolar ordered systems against doping in many cases. For some materials doping studies have been performed and the critical concentrations of the dopants destroying the quadrupolar order have been determined. These material systems with some of their properties are listed in table 5.1.

As can be seen most of these materials have low ordering temperatures and low critical doping concentrations x_c where quadrupolar order is suppressed. Only $Dy_{1-x}Y_xB_2C_2$ has a significantly higher ordering temperature and critical concentration. Still, within this series of materials UPd_3 is unique as none of the other compounds reacts as sensitively to doping as UPd_3 and no magnetic order is found. Only

Material	$T_Q\|_{x=0}$ (K)	x_c	Ref.
$Dy_{1-x}Y_xB_2C_2$	24.7	> 0.6	[101]
$Ce_{1-x}La_xB_6$	3.3	0.3	[102]
$Ce_{1-x}Pr_xB_6$	3.3	0.12	[103, 104]
$Ce_{1-x}Nd_xB_6$	3.3	0.12	[105]
$U_{1-x}Np_xPd_3$	7.8	$0.05 < x_c < 0.5$	[106]
$YbRu_2(Ge_{1-x}Si_x)_2$	10.2	< 0.02	[107]
$Pr_{1-x}La_xPb_3$	0.4	0.02	[108]
$U(Pd_{1-x}Pt_x)_3$	7.8	≈ 0.01	[109–111]

Table 5.1: Quadrupolar ordered systems for which doping series have been studied with ordering temperatures of the undisturbed systems and critical doping concentrations. For details see text.

$YbRu_2(Ge_{1-x}Si_x)_2$ might exhibit a similar sensitivity on doping although no experiments for samples with $x < 0.02$ have been published as yet.

The material system $U(Pd_{1-x}Pt_x)_3$ has been studied since the late 1980s. This system is particularly interesting since with the variation of the alloying parameter x it causes Pt $5d$ electrons to be introduced into the system, driving the uranium $5f$ electrons from a localized state in UPd_3 to an itinerant heavy-fermion state in UPt_3. While the lattice constants of both compounds are very similar ($a = 5.757$ Å and $c = 9.621$ Å in UPd_3 / $a = 5.752$ Å and $2c = 9.778$ Å in UPt_3) and therefore chemical pressure can be considered as irrelevant, the crystal structures of UPd_3 and UPt_3 are slightly different, with the $TiNi_3$ (double hexagonal close packed / dhcp / space group $P6_3/mmc$) structure in UPd_3 and the $MgCd_3$ (hexagonal close packed / hcp) structure in UPt_3. In between these structures of the pure compounds a 10-layer superstructure is found for $0.42 < x < 0.67$ [112, 113]. Since in the present study we investigate samples with $x \leq 0.01 = 1\%$ we are close to the limit of pure UPd_3. Thus, we will first discuss the properties of pure UPd_3 before considering $U(Pd_{1-x}Pt_x)_3$. Finally, the temperature and field evolution of the ordered phases of UPd$_3$ will be calculated in a mean-field-model which gives some implications on possible mechanisms to explain the observed properties of U(Pd$_{1-x}$Pt$_x$)$_3$.

5.1 Physical properties of UPd$_3$

Although the existence and crystallographic structure of the compound UPd$_3$ is known since the 1950s, detailed studies on this material were not published until the late 1970s [112]. Then, in an inelastic neutron scattering study strong signals from CEF levels were found indicating the localized nature of the uranium f electrons in the $5f^2$ state (U^{4+}) but no magnetic order was observed [114]. In the same year anomalies in the low temperature specific heat, resistivity and susceptibility as shown in Figs. 5.1 and 5.7 have been observed indicating two non-magnetic phase transitions at 6 and 7 K. Additionally, a quadrupolar origin of these phase transitions was first suggested and a comparison to an alternative scenario with antiferromagnetic order of small induced magnetic moments lead to the conclusion that quadrupolar order is in much better agreement with experimental data and is thus most likely in UPd$_3$ [115].

In a series of subsequent studies these phase transitions were studied in more detail with thermal expansion, neutron scattering, Hall effect, thermoelectric power, magnetoresistance, dHvA and other techniques. In inelastic neutron scattering studies by Shamir *et al.* strong signals with characteristics of Uranium CEF transitions were found and a CEF scheme for the uranium $5f$ electrons was proposed which was in good agreement with these experiments on UPd$_3$ [116–124].

Additionally, it was pointed out that for the Uranium atoms 5 different quadrupole moments are possible in this compound. These quadrupole moments are $O_{zz}(= O_2^0)$ which always has a finite non-zero value and

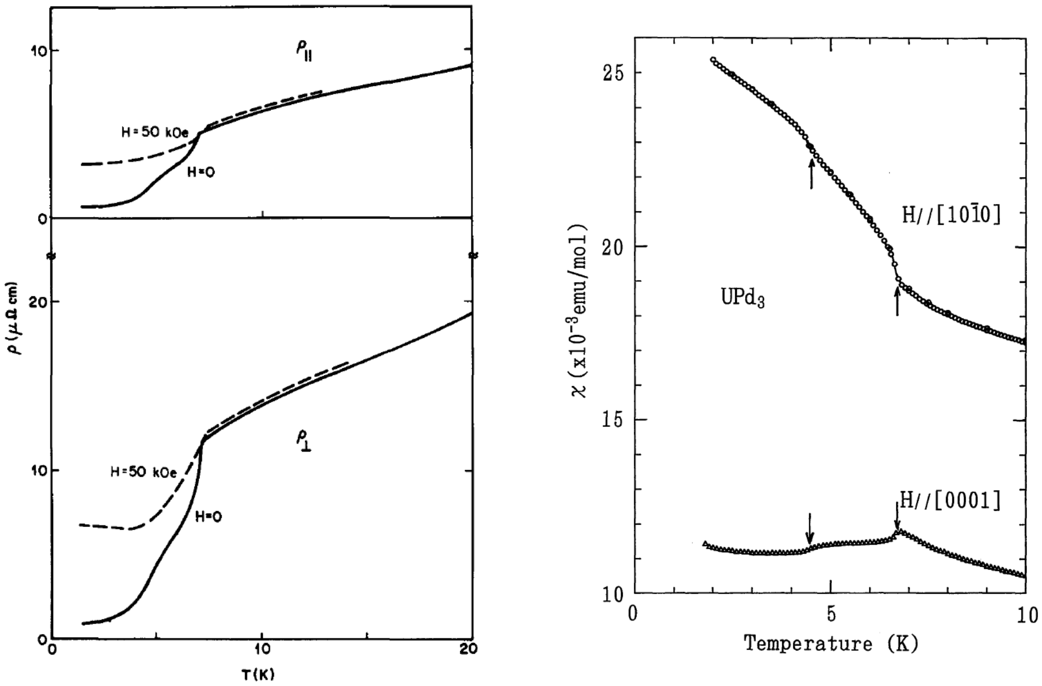

Figure 5.1: Anomalies in the resistivity and susceptibility indicating the T_1 and T_2 phase transitions in UPd$_3$ [115, 116] .

hence is not an order parameter of UPd$_3$ and O_{zx}, $O_{x^2-y^2}$, O_{xy} and O_{yz} which are zero at high temperatures and are thus possible order parameters [122]. A detailed explanation of the calculation of these moments will be given in section A.

Later, with very precise ultrasound and thermal expansion measurements on high quality samples as shown in Fig. 5.2, it was found that in UPd$_3$ there are not only three but four phase transitions at $T_0 = 7.6$ K, $T_{+1} = 6.9$ K, $T_{-1} = 6.7$ K and T_2 =4.4 K [9, 125–127].

In 2003, in a study by McEwen *et al.* the available experimental data was carefully reanalyzed and from the magnetic susceptibility and entropy changes at the four phase transitions it was concluded that the original CEF level scheme proposed by Buyers *et al.* is not completely

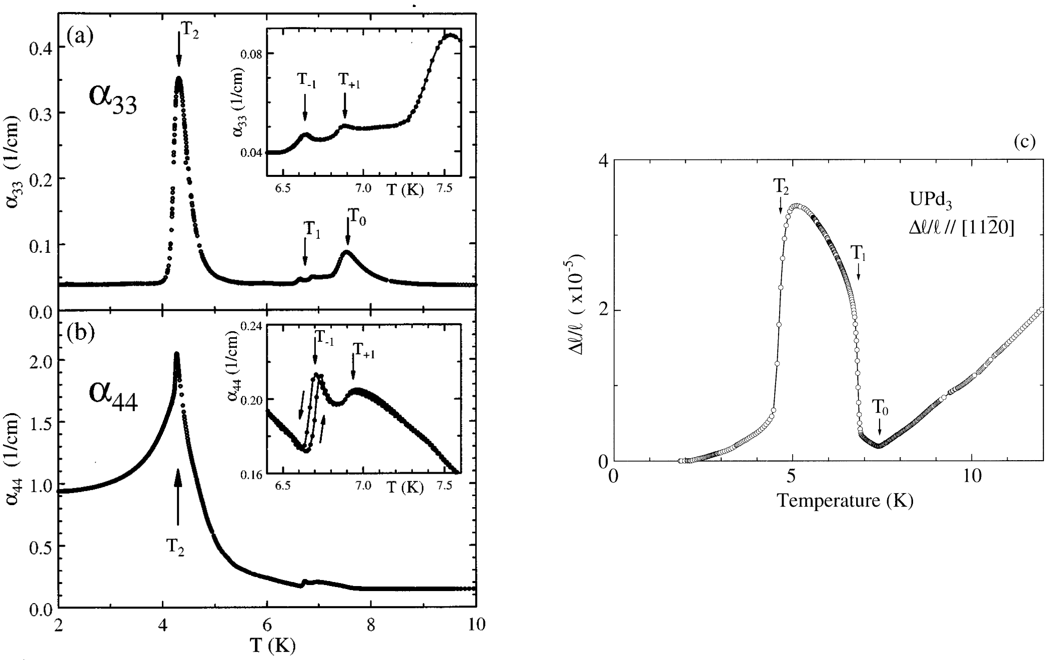

Figure 5.2: Anomalies in the ultrasound attenuation and thermal expansion indicating a total of four phase transitions in UPd$_3$ [9, 126].

to correct but has to be modified to agree with all experimental data. The low-lying CEF-levels for the two inequivalent Uranium sites (with local hexagonal and quasi-cubic symmetry) in the dhcp crystal structure of UPd$_3$ for the original and modified CEF schemes are shown in Fig. 5.3 [118, 128].

Since sample quality strongly influences the features observed in experimental data a magnetic phase diagram of UPd$_3$ was not published until Tokiwa *et al.* applied a wide range of experimental techniques to samples from the same high quality single crystal ingot and derived the phase diagrams depicted in Fig. 5.4 in 2001 [9].

In this extensive study previously reported results were verified including the ABAC stacking sequence of hexagonal planes along the c axis as it is depicted in Fig. 5.5 [130]. This structure causes two in-

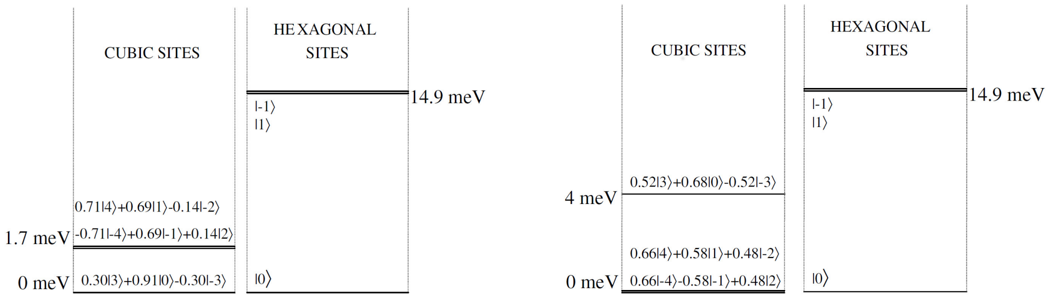

Figure 5.3: Proposed low-lying CEF levels in a CEF scheme with singlet (Buyers *et al.*, 1980, [129], left) and doublet (McEwen *et al.*, 2003, [128], right) ground state on the cubic uranium sites.

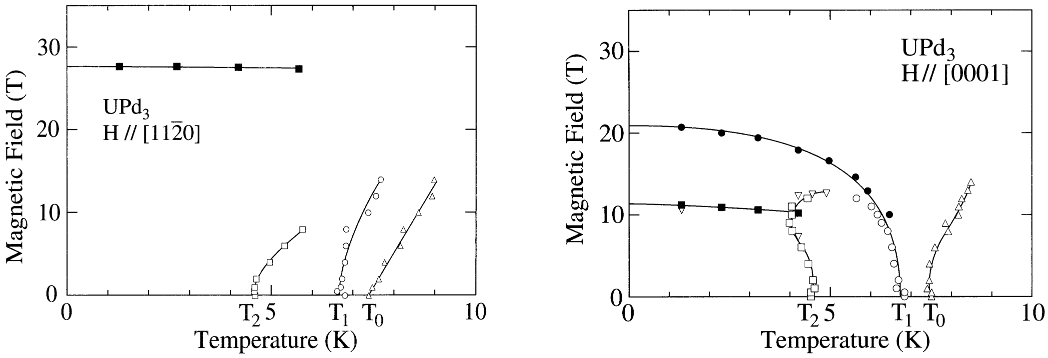

Figure 5.4: Experimentally determined phase diagrams for UPd$_3$ with a magnetic field applied along the a ([11$\bar{2}$0]) and c ([0001]) axes [9].

equivalent uranium sites of local hexagonal and cubic symmetry with smallest U-U distances of 4.11 Å for lattice constants of $a = 5.73$ Å and $c = 9.66$ Å [112, 130, 131]. The electronic specific heat coefficient was determined to $\gamma = 7.6$ mJ mole^{-1} K^{-2} indicating that the electronic correlations are relatively weak in this compound [9].

Finally, in a recent series of resonant X-Ray scattering studies the quadrupolar order parameters in UPd$_3$ could be determined to be $\langle O_{zx} \rangle$ and $\langle O_{x^2-y^2} \rangle$ in a ratio of 6:1 for $T_{+1} < T < T_0$, $\langle O_{xy} \rangle$ and $\langle O_{yz} \rangle$ in a ratio of 14:1 (8:1) for $T < T_2$ ($T_2 < T < T_{-1}$) and a combination

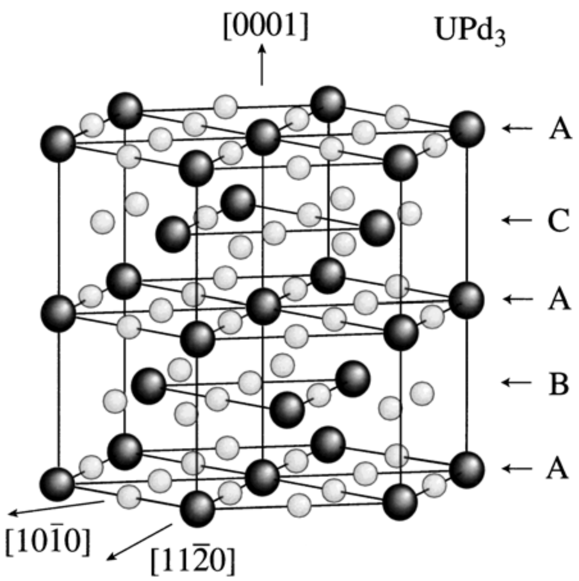

Figure 5.5: dhcp crystal structure of UPd$_3$ [9].

of all four between T_{-1} and T_{+1} [130–134]. A visualization of such a combination of order parameters is given in Fig. 5.6

In all these studies, together with ARPES and Core-Level photoelectron spectroscopy measurements as well as theoretical work, the uranium $5f$ electrons are found to be strongly localized in UPd$_3$, and in particular stronger than in any other uranium compound [135–137].

However, sample quality seems to be an issue in all these studies since ordering temperatures, lattice constants and other properties of the crystals vary. This sample quality dependence is best visualized by a comparison of published heat capacity data for single crystalline UPd$_3$ shown in Fig. 5.7.

In this comparison the large anomaly indicating the T_1 transition at $T \approx 6.5$ K is visible in all sets of data at slightly different temperatures but the smaller features indicating the transitions at T_0 and T_2 differ strongly and in fact are not found for all crystals studied in literature.

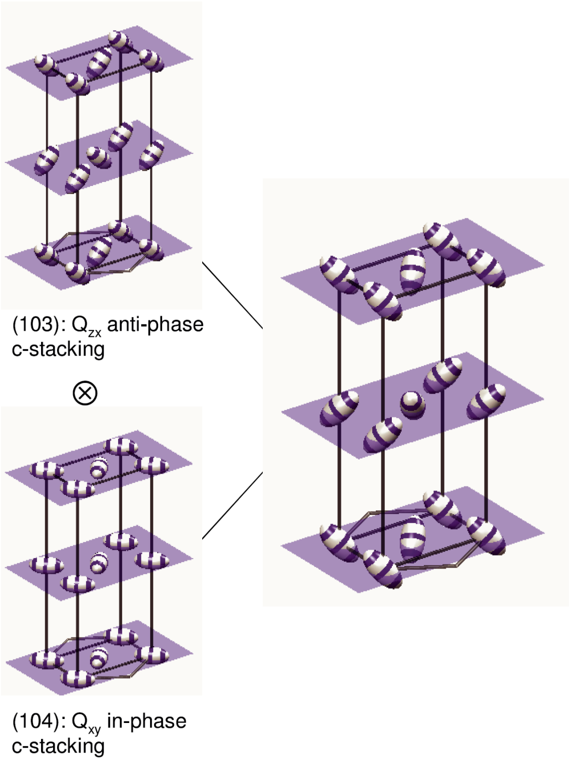

Figure 5.6: The orthorhombic unit cell of UPd_3 with the quadrupolar charge distributions on the quasi-cubic uranium sites for two different order parameters. Ellipsoids represent the distorted charge distribution causing the quadrupolar moments [131].

The same observation can as well be made for other physical properties of UPd_3. However, in all these studies at least some of the quadrupolar phases are found by the observation of some intrinsic anomalies of UPd_3, thus the existence of quadrupolar ordered phases seems to be stable against small crystal imperfections.

5.2 Influence of Pt in $U(Pd_{1-x}Pt_x)_3$

Since the crystal structures of UPd_3 (dhcp) and UPt_3 (hcp) are different, a crystallographic transition has to occur in the alloying series

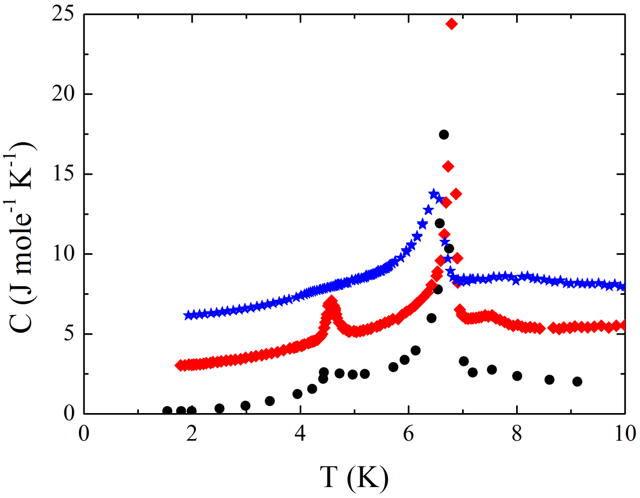

Figure 5.7: Published specific heat data of single crystalline UPd$_3$ from Andres *et al.* (black circles, [115]), Tokiwa *et al.* (red diamonds, [9]) and Walker *et al.* (blue stars, [111]). Red and blue data are shifted by 3 and 6 J mole^{-1} K^{-1} for clarity.

U(Pd$_{1-x}$Pt$_x$)$_3$. This transition was found in a range of $0.42 < x < 0.67$ where a 10-layer superstructure is observed in between the dhcp and hcp structures for the pure compounds. Additionally, electronic effects are also expected since in UPd$_3$ the overlap of the outer Pd $4d$ electron wavefunctions with uranium $5f$ electron wavefunctions is small and the latter are well localized. By the replacement of Pd with isoelectronic Pt $5d$ electrons with spatially much more extended wavefunctions are introduced into the system leading to a stronger hybridization of $5d$ and uranium $5f$ electrons [113]. This view is also supported by theoretical considerations where a fully localized $5f^2$ configuration is found in UPd$_3$ while in in UPt$_3$ only one f electron is localized [138].

As a result of this increasing $f-d$ hybridization the quadrupolar phase transitions in UPd$_3$ are found to depend very sensitively on Pt doping. Already at an alloying level of $x = 5\%$ no signatures of quadrupolar phase transitions are observable any more [109]. More recently, a closer inspection of the alloying dependence revealed that for Pt concentrations as small as $x = 0.5\%$ the quadrupolar ordering temperatures are reduced by about 40% compared to pure UPd$_3$ while already at $x = 1\%$ no long range order is observed any more [110]. On the other hand, the system is much more stable with respect to the replacement of uranium, where the ordering $5f$ wavefunctions are located, as for instance for Neptunium where long range order is still observed for 5% Np in (U$_{1-x}$Np$_x$)Pd$_3$ [106]. Interestingly, the superconducting state in UPt$_3$ exhibits a similar sensitivity to Pd alloying as the quadrupolar ordered phase in UPd$_3$ to Pt alloying and is suppressed already with 0.6% Pd or $x \leq 0.994$ [139–141].

5.3 Scaling of the transition temperatures in U(Pd$_{1-x}$Pt$_x$)$_3$

We have characterized U(Pd$_{1-x}$Pt$_x$)$_3$ samples with alloying levels of $x = 0.5\%$ and $x = 1\%$ by means of specific heat, resistivity, and susceptibility/magnetization measurements. In the specific heat measurements presented in Ref. [65] a strong reduction of the ordering temperatures T_1 to 4.5 K and T_2 to 2.5 K was observed already for alloying levels as low as $x = 0.5\%$. For $x = 1\%$ only a broad shoulder exists around ≈ 2.7 K indicating the absence of long-range order (LRO) but possible short-range order (SRO) below the further shifted T_1 transition. The same shift of ordering temperatures with increasing x was also observed in resistivity and susceptibility measurements. A comparison of experimental data to the theory of Fisher and Langer (Ref. [142]) which predicts a proportionality between specific heat c_p and the derivative of the electrical resistivity $\frac{\partial \rho}{\partial T}$ for second order phase transitions was performed and the theoretical predictions could be verified for the samples of $\mathrm{U(Pd_{1-x}Pt_x)_3}$ with $x = 0.5\%$ [65].

Since sample quality is an important issue in $\mathrm{UPd_3}$ and $\mathrm{U(Pd_{1-x}Pt_x)_3}$ (see discussed above) we have annealed the samples used in Ref. [65] for one week at 900°C in order to improve their quality [110]. This way structural disorder and defects should be reduced and signatures of phase transitions should become more clear and a possible suppression of ordering temperatures or long-range order should be reduced, hence the features indicating such transitions should become more pronounced. After the annealing procedure has been performed we reanalyzed our samples with resistivity and susceptibility measurements.

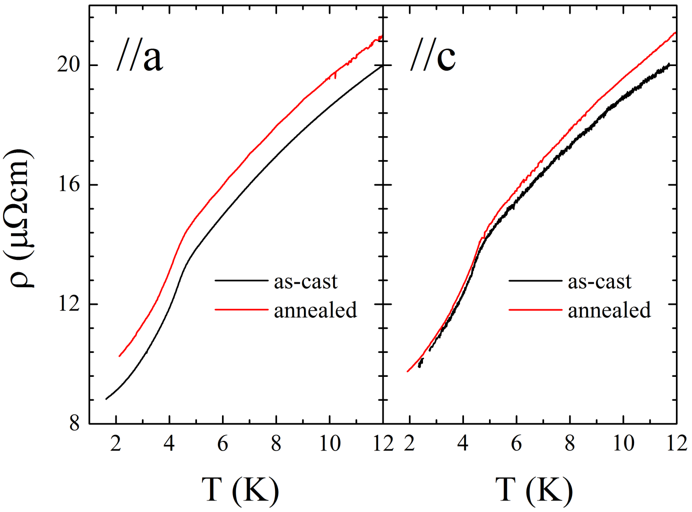

Figure 5.8: Resistivity of $\mathrm{U(Pd_{1-x}Pt_x)_3}$ with $x = 0.5\%$ measured along the crystallographic a and c directions before and after the annealing procedure has been performed [110].

Two exemplary data sets for the resistivity of a $x = 0.5\%$ and the susceptibility of a $x = 1\%$ sample before and after the annealing procedure are depicted in the Figs. 5.8 and 5.9. As in the depicted data sets, in all these measurements resistivity and susceptibility are only slightly altered between ascast and annealed samples. Moreover, in some samples the sample-quality seems to have decreased which is indicated by an increased resistivity (Fig 5.8). Of course the sample quality does not decrease due to the annealing process but the effect of microscopic cracks caused by the large temperature changes might be larger than the effect of an improved sample quality here. This is also reflected in the residual resistivity ratios and Curie-Weiss temperatures which are only slightly altered with incresed or decreased values after the annealing procedure being distributed randomly for all samples [110].

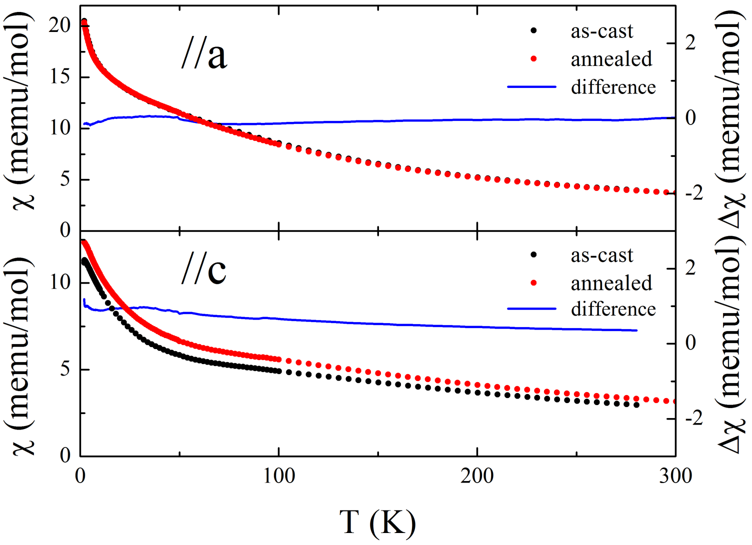

Figure 5.9: Susceptibility of $U(Pd_{1-x}Pt_x)_3$ with $x = 1\%$ measured along the crystallographic a and c directions in an applied magnetic field of $B = 0.1$ T before and after the annealing procedure has been performed [110].

Since we do not find significant changes in the resistivity and susceptibility of the annealed samples we conclude that the annealing procedure, although we can expect a decrease of structural disorder and defect densities, does not alter the electronic properties of $U(Pd_{1-x}Pt_x)_3$. Hence, the suppression of the ordering temperatures and long-range order with alloying is an intrinsic feature of U(Pd$_{1-x}$Pt$_x$)$_3$ [110]. Therefore we can now continue and determine the phase transition temperatures from our specific heat, resistivity and susceptility data following the procedures described in Ref. [65].

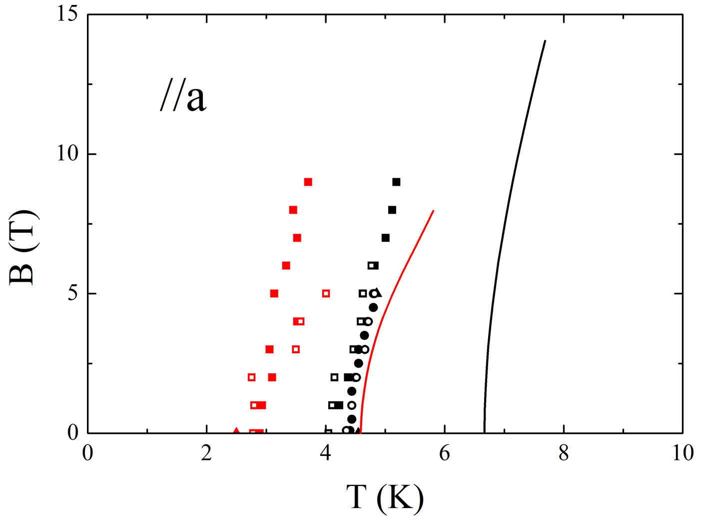

Figure 5.10: Magnetic phase diagram of U(Pd$_{1-x}$Pt$_x$)$_3$ with $x = 0.5\%$ for magnetic fields applied along the a axis [110]. Solid lines indicate the T_1 (black) and T_2 (red) transition temperatures of pure UPd$_3$ from Ref. [9]. Symbols of the same color are the respective transition temperatures of U(Pd$_{1-x}$Pt$_x$)$_3$ with $x = 0.5\%$ determined from specific heat (triangles), resistivity (squares) and susceptibility (circles) measurements in the as-cast (filled symbols) and annealed (open symbols) samples.

The resulting phase diagrams of a U(Pd$_{1-x}$Pt$_x$)$_3$ sample with $x = 0.5\%$ for magnetic fields applied along the a and c axes are depicted in the Figs. 5.10 and 5.11. A comparison to the transition temperatures found in pure UPd$_3$ (lines in the respective phase diagrams) reveals a close resemblance of the magnetic field dependence of the phase transition temperatures for $x = 0.5\%$ and pure UPd$_3$. This resemblance is even more emphasized when we renormalize all transition temperatures both for $x = 0$ and $x = 0.5\%$ with their respective T_1 transition temperatures. This is visualized in Fig. 5.12 for both crystallographic axes where we find good agreement for all transition temperatures although our transition temperatures are scattered due to the broadened and less pronounced features indicating the transition temperatures in U(Pd$_{1-x}$Pt$_x$)$_3$ with $x = 0.5\%$.

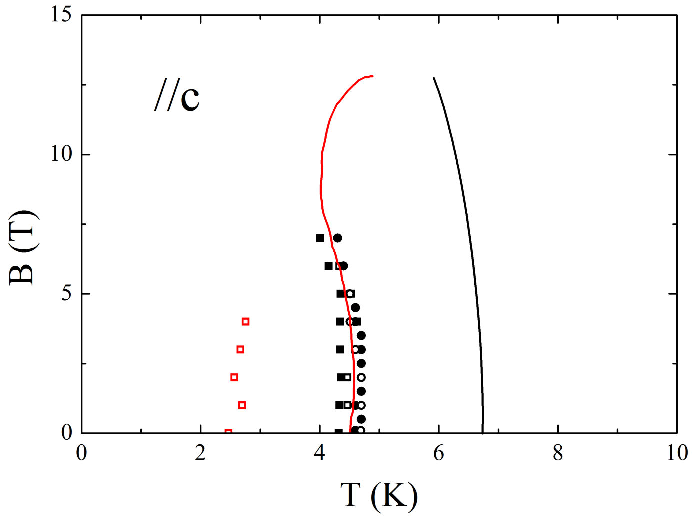

Figure 5.11: Magnetic phase diagram of U(Pd$_{1-x}$Pt$_x$)$_3$ with $x = 0.5\%$ for magnetic fields applied along the c axis [110]. Solid lines indicate the T_1 (black) and T_2 (red) transition temperatures of pure UPd$_3$ from Ref. [9]. Symbols of the same color are the respective transition temperatures of U(Pd$_{1-x}$Pt$_x$)$_3$ with $x = 0.5\%$ determined from specific heat (triangles), resistivity (squares) and susceptibility (circles) measurements in the as-cast (filled symbols) and annealed (open symbols) samples.

We can now continue and draw the alloying phase diagram for U(Pd$_{1-x}$Pt$_x$)$_3$ at low doping levels. Since we are limited to the T_1 and T_2 transition temperatures and samples with $x = 0.5\%$ and $x = 1\%$ together with reference data from Tokiwa *et al.* for pure UPd$_3$ (Ref. [9]) we simply assume a linear shift of the transition temperatures with increasing alloying level x. Now, at $x = 1\%$ we could not observe clear phase transitions any more but only broad features in specific heat measurements which indicate possible short range order. Thus between $x = 0.5\%$ and $x = 1\%$ the long-range order is replaced by a regime dominated by short-range order. From a linear extrapolation of the ordering temperatures found for $x = 0$ and $x = 0.5\%$ we expect the quadrupolar order to be completely suppressed with an alloying level of $x \approx 1.5\%$. The phase diagram put together this way is depicted in Fig. 5.13. Unfortunately no samples of this composition are available to verify the complete absence of ordered phases so we can not draw definite conclusions for this part of the phase diagram.

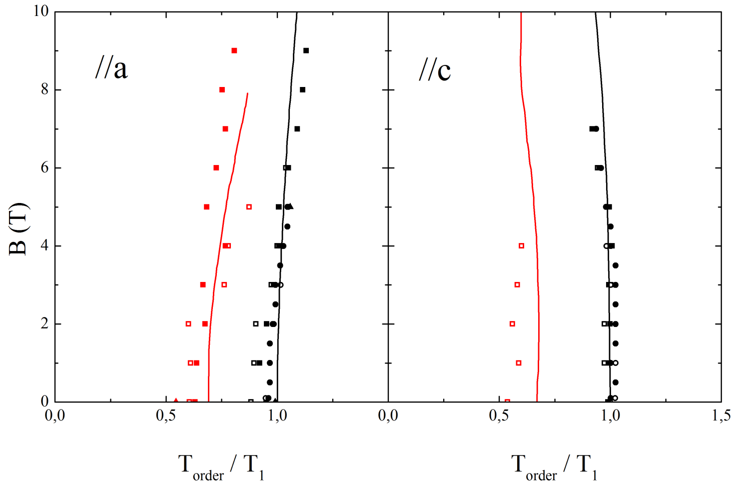

Figure 5.12: Magnetic phase diagram of $U(Pd_{1-x}Pt_x)_3$ with $x = 0.5\%$ for magnetic fields applied along the a and c axes with transition temperatures normalized to the T_1 transition temperatures in zero magnetic field for the respective alloying levels [110]. Solid lines indicate the T_1 (black) and T_2 (red) transition temperatures of pure UPd_3 from Ref. [9]. Symbols of the same color are the respective transition temperatures of $U(Pd_{1-x}Pt_x)_3$ with $x = 0.5\%$ determined from specific heat (triangles), resistivity (squares) and susceptibility (circles) measurements in the as-cast (filled symbols) and annealed (open symbols) samples.

Since the annealing process did not influence the measured physical properties of $U(Pd_{1-x}Pt_x)_3$ significantly we can rule out strong structural influences on the electronic properties in this compound. Hence, the observed shift of transition temperatures with alloying is an intrinsic feature of U(Pd$_{1-x}$Pt$_x$)$_3$. From the finding that the same features in our measurements on U(Pd$_{1-x}$Pt$_x$)$_3$ with $x = 0.5\%$ indicate the same phase transitions as in pure UPd$_3$, even though the features might be less clear and broadened, we concluded that the physical mechanisms are the same in both compounds. This interpretation is even more supported by the magnetic field dependency of the transition temperatures in samples with $x = 0.5\%$ since all parts of the magnetic phase diagram accessed in our measurements can be mapped onto the phase diagram of pure UPd$_3$ by a simple renormalization of the transition temperatures. Thus, it should be possible to extend models and explanations which are able to account for the observed properties of UPd$_3$ to the properties of U(Pd$_{1-x}$Pt$_x$)$_3$ as well. This ansatz will be limited to alloying levels of up to 0.5% since in our samples with $x = 1\%$ we could not observe long-range order any more.

5.4 Mean field modeling of UPd$_3$

The ansatz to model the physical properties of UPd$_3$ in a mean field model of the uranium CEF levels has been first used by Tokiwa *et al.* as described in Ref. [9]. In this study the crystal electric field, a Zeeman term and two mean field terms for the nonvanishing O_2^0 quadrupole-quadrupole interaction and ordering $\langle O_{zx} \rangle$ quadrupoles were taken into account. This way magnetization and the experimentally found dependence of the T_0 phase transition on an applied magnetic field along the c direction could be reproduced accurately. However, due to the limitation to one single order parameter the phase transitions at $T_{\pm 1}$ and T_2 were not included. Moreover, the resulting phase boundary in a $B-T-$phase diagram for the magnetic field applied along the a axis does not match

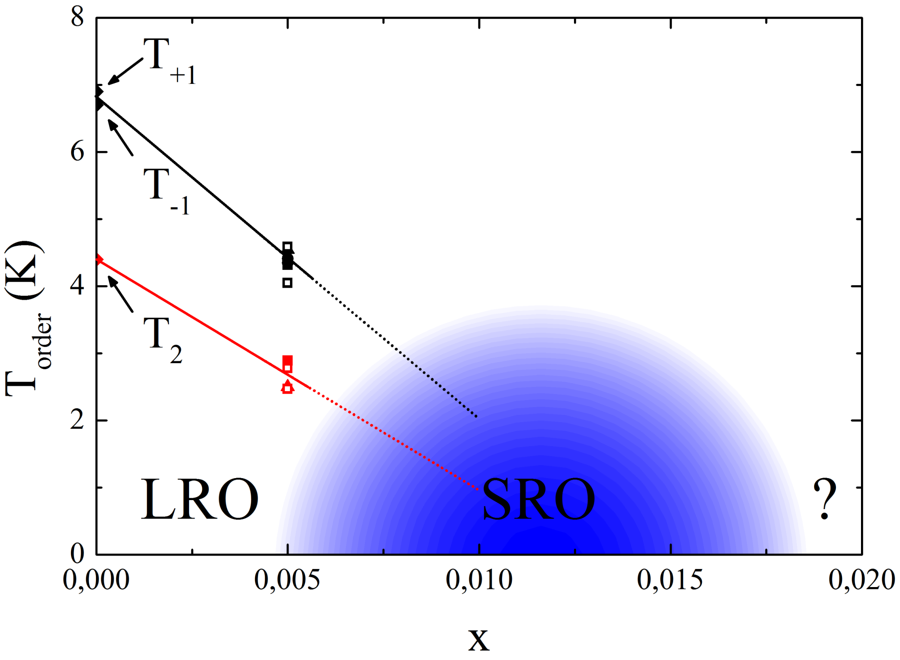

Figure 5.13: Alloying phase diagram of U(Pd$_{1-x}$Pt$_x$)$_3$. For small x long range order (LRO) is observed which is suppressed with increasing x and which causes the formation of a region with short range order (SRO). Ordering temperatures for $x = 0$ are taken from Ref. [9]. Black (red) symbols indicate the T_1 (T_2) transition temperatures determined from our specific heat (triangles), resistivity (squares) and susceptibility (circles) measurements in the as-cast (filled symbols) and annealed (open symbols) samples.

experimental data.

Since we have shown above that the physical mechanisms are the same for pure UPd$_3$ and U(Pd$_{1-x}$Pt$_x$)$_3$ at small alloying levels we have set up a similar mean field CEF model for UPd$_3$. Contrary to Tokiwa *et al.* we start with the single order parameter model only to check the validity of our calculations and continue with extended models including a combination of more possible order parameters until we finally allow for all 5 possible quadrupole moments in this compound.

To explore and parameterize the influence of platinum substitution in U(Pd$_{1-x}$Pt$_x$)$_3$ we calculated the order parameters and the magnetic phase diagram of pure UPd$_3$ within this mean field model following the ansatz of Tokiwa *et al.*. An almost identical model was previously proposed by McEwen *et al.* but the phase diagram was not calculated in detail [120]. Now, in such a model for pure UPd$_3$ it might be possible to either identify parameters which are critical for the AFQ order in this compound or to introduce some disturbance to the system which might have similar effects as an increased hybridization and result in a reduction of ordering temperatures as observed in the experiments on U(Pd$_{1-x}$Pt$_x$)$_3$. This way it might be possible to determine if U(Pd$_{1-x}$Pt$_x$)$_3$ can be treated in a completely localized picture or if at least to some degree hybridization and band structure effects have to be taken into account. Since the ordered quadrupole moments are localized at the quasi-cubic uranium sites only these CEF levels are taken into account. In all cases the Hamiltonian of the system has the form

$$H = H_{CEF} + H_Z - \sum_i K_i \left\langle O_i \right\rangle O_i \tag{5.1}$$

where the crystal electric field and Zeeman[1] terms are given by

$$H_{CEF} = B_2^0 O_2^0 + B_4^0 O_4^0 + B_4^3 O_4^3 + B_6^0 O_6^0 + B_6^3 O_6^3 + B_6^6 O_6^6 \tag{5.2}$$

and

$$H_Z = -g_J \mu_B J_z B \tag{5.3}$$

with K_i, $\langle O_i \rangle$ and O_i being the quadrupole-quadrupole interaction strength, the expectation value of the Quadrupole moment and the corresponding quadrupole Operator. B_p^q and O_p^q in the crystal electric field Hamiltonian H_{CEF} are the CEF parameters and the Stevens Operators,

---

[1] Here and in the following we write B instead of H for the magnetic field in the Zeeman term to prevent a misleading ambiguity with the Hamiltonian.

respectively. These and other necessary operators are discussed in more detail in Appendix A. g_J is the Landé-factor, μ_B and J_z are the Bohr magneton and the angular momentum operator and B is the applied magnetic field. CEF parameters for the CEF scheme proposed in Ref. [129] with a singlet ground state and an excited doublet 1.7 meV above which is shown in Fig. 5.14 are taken from Ref. [9]. To obtain CEF parameters for the CEF scheme proposed in Ref. [128] (Fig. 5.3) with a doublet ground state and an excited singlet at 4 meV the higher CEF levels were assumed to be at the same energy as in Ref. [9]. The CEF parameters were then calculated numerically to fit the energies of the CEF levels. The CEF parameters calculated this way are summarized in table 5.2.

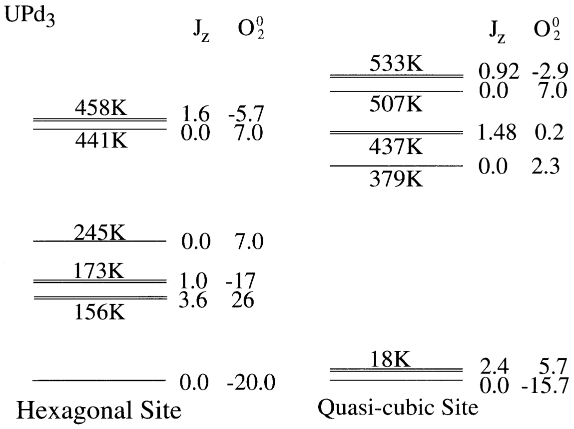

Figure 5.14: CEF-level scheme from Ref. [9] for UPd$_3$ according to neutron scattering data from Ref. [118].

Due to the trigonal symmetry of the quasi-cubic uranium sites only the B_k^q coefficients given in Eq. 5.2 may be non-zero. In general, for this structure also terms B_4^{-3}, B_6^{-3} and B_6^{-6} are allowed but an appropriate coordinate transformation can be applied so that these coefficients become zero [143]. Since CEF parameters were determined by a fit to given CEF energy levels these coefficients can be set to zero which implicitly

	singlet ground state K	 meV	doublet ground state K	 meV
B_2^0	3.13	0.270	-7.013	-0.8480
B_4^0	-0.130	-0.0112	-0.07550	-0.002407
B_4^3	2.57	0.221	-2.902	-0.1347
B_6^0	0.00346	0.000298	0.002585	0.0001575
B_6^3	0.0628	0.00541	0.005943	0.002570
B_6^6	0.0311	0.00268	0.02744	0.004537

Table 5.2: CEF parameters for the two CEF schemes depicted in Fig. 5.3 in K and meV. Parameters for the singlet ground state scheme are taken from Ref. [9]. Parameters for the doublet ground state scheme are calculated assuming the three lowest CEF states at the energies given in Ref. [128]; for details see text.

includes the correct coordinate transformation [144].

For the Landé-factor we find

$$g_J = 1 + \frac{j(j+1) - l(l+1) + s(s+1)}{2j(j+1)} = \frac{5}{4} \tag{5.4}$$

with $s = 1$, $l = 5$ and $j = 4$ according to Hund's rule in the $5f^2$ state of uranium in UPd$_3$ [145]. In our study the magnetic field B was assumed to be in the z-direction, thus along the c axis of UPd$_3$, in all cases.

It has to be noted that in this model until now only interactions between identical quadrupoles are taken into account. Thus, no mixed terms of the form

$$K_{ij} \langle O_i \rangle O_j \tag{5.5}$$

are considered which could cause stronger interference between competing order parameters presented in the calculations in section 5.4.2. It has already been argued earlier that such terms might be necessary to get a better quantitative understanding of UPd$_3$ [120]. However, to our knowledge such studies have not been published which is most likely due to the large number of additional free coupling constants involved in such a scenario.

With the Hamiltonian given in Eq. 5.1 we can now calculate the CEF levels with their corresponding J_z, O_2^0 values as well as the expectation values $\langle O_i \rangle$. The calculations are straightforward with the CEF states and energies being the Eigenvectors $|n\rangle$ and Eigenvalues E_n of H and $J_{z,n}$ and $O_{2,n}^0$ for each CEF level given by:

$$J_{z,n} = \langle n| J_z |n\rangle \qquad O_{2,n}^0 = \langle n| O_2^0 |n\rangle . \tag{5.6}$$

To determine the order parameters $\langle O_i \rangle$ we calculate the free energy of the system

$$F(\langle O_i \rangle , B, T) = -k_B T \ln \left(\sum_n e^{-\frac{E_n}{k_B T}} \right) + \sum_i \frac{|K_i|}{2} \langle O_i \rangle^2 \tag{5.7}$$

which is then minimized numerically in order to find the order parameters $\langle O_i \rangle$ for a given set of coupling constants, magnetic field and temperature. With all these values known we can then calculate the magnetization

$$M = \langle J_z \rangle = \frac{\sum_n J_{z,n} e^{-\frac{E_n}{k_B T}}}{\sum_n e^{-\frac{E_n}{k_B T}}}. \tag{5.8}$$

The program code to perform these calculations is included in Appendix B for one examplary case, namely the model used in chapter 5.4.2

5.4.1 Single order parameter models

To test our model and the reliability of the implemented numerical funtions we first calculated the model given in Ref. [9] and compared our results with published ones. Additionally, we tried to use the same Hamiltonian with different CEF parameters which reproduce the CEF level scheme proposed by McEwen *et al.* [128]. In a further step, we then exchanged the $\langle O_{zx} \rangle$ order parameter with $\langle O_{xy} \rangle$ before allowing for multiple order parameters in order to possibly reproduce the $T_{\pm1}$ and T_2 phase boundaries in the magnetic phase diagram .

Since the lowest CEF levels have a considerable $O^0_{2,n}$ moment a term taking into account the O^0_2-O^0_2-interaction is included in all models. Additionally, the expectation value $\langle O^0_2\rangle$ of the system is always non-zero since it arises from the uniaxial $3J_z - J(J+1)$ term, hence this is not an order parameter in UPd$_3$ [122].

$\langle O_{zx}\rangle$ order parameter with singlet ground state

The model implemented first is the one used by Tokiwa *et al.* in Ref. [9] with only an $\langle O_{zx}\rangle$ order parameter. The Hamiltonian of this system is given by

$$H = H_{CEF} + H_Z - K^0_2 \langle O^0_2\rangle O^0_2 - K_{zx} \langle O_{zx}\rangle O_{zx}, \tag{5.9}$$

with the CEF parameters from the first columns of table 5.2 and the coupling contants $K^0_2 = 0.01$ K and $K_{zx} =$ -0.19 K. For the CEF states we find our CEF energies to agree well with published data while some differences appear in $J_{z,n}$ and $O^0_{2,n}$. Since the Hamiltonian and all parameters involved are identical this is not expected. The whole set of parameters together with reference data is summarized in table 5.3.

The origin of the observed discrepancies is not clear but the CEF energies agree very well. Additionally, the $J_{z,n}$ and $O^0_{2,n}$ parameters are similar in sign and magnitude for the low energy states which determine the low temperature properties of UPd$_3$. Since our phase diagram and magnetization calculated using this CEF parameters agree very well with the ones from Ref. [9] (compare Figs. 5.16 and 5.17) we believe our model, despite these discrepancies to published values, to be correct. The remaining differences might possibly be explained by the use of different numerical routines with different precision resulting in different

$\|n\rangle$	type	Energy		$J_{z,n}$		$O^0_{2,n}$	
		Ref.	Calc.	Ref.	Calc.	Ref.	Calc.
$\|8\rangle, \|7\rangle$	doublet	533 K	533 K	0.92	0.92	-2.9	4.5
$\|6\rangle$	singlet	507 K	508 K	0.0	0.0	7.0	7.0
$\|5\rangle, \|4\rangle$	doublet	437 K	437 K	1.48	0.05	0.2	-1.8
$\|3\rangle$	singlet	379 K	379 K	0.0	0.0	2.3	5.0
$\|2\rangle, \|1\rangle$	doublet	18 K	18 K	2.4	2.1	5.7	0.3
$\|0\rangle$	singlet	0 K	0 K	0.0	0.0	-15.7	-18.0

Table 5.3: Calculated energies, $J_{z,n}$ and $O^0_{2,n}$ values for the CEF states calculated in a singlet ground state scheme. Shown are our data (Calc.) and Reference data (Ref.) from Tokiwa *et al.* [9]. For details see text.

parameters or by an accidental permutation of the calculated values in Ref. [9].

In a next step we can now calculate the ordering parameter $\langle O_{zx}\rangle$ in this model for different temperatures and applied magnetic fields. All order parameters calculated here and in the following have no units since we define the corresponding angular momentum operators given in Appenix A without $\hbar$, corresponding to the definition $\hbar = 1$. Positive (negative) signs of the expectation values correspond to an elongation (shortening) of the quadrupolar charge distribution in the respective direction. Contrary to published results with the same CEF parameters and coupling constants no quadrupolar order, hence no $\langle O_{zx}\rangle \neq 0$, is observed. In contrast, upon changing the coupling constant K_{zx} from -0.19 K to -3.10 K $\widehat{=}$ -0.267 meV we find a quadrupolar ordered phase with order parameter $\langle O_{zx}\rangle$. The sign of the order parameter Without an applied magnetic field the order parameter is developing below an ordering temperature of 6.83 K as depicted in Fig. 5.15 and as it was found in Ref. [9].

With these parameters we can now calculate the magnetic phase diagram and the magnetization at $T = 4.2$ K using Eqs. 5.7 and 5.8.

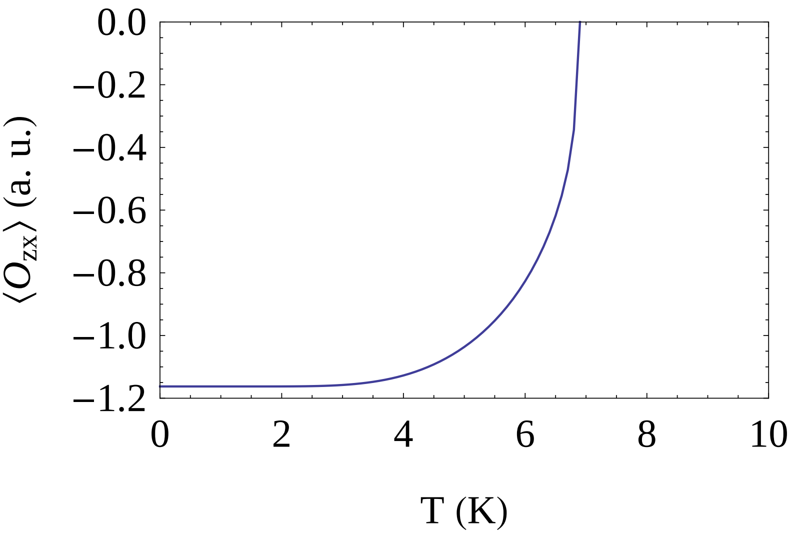

Figure 5.15: Ordering parameter $\langle O_{zx} \rangle$ vs. temperature in zero magnetic field with coupling constants K_2^0 = 0.01 K and K_{zx} = -0.267 meV $\widehat{=}$ -3.10 K chosen to reproduce results from Tokiwa *et al.* [9].

Our results, together with the results of Tokiwa *et al.* from Ref. [9] are depicted in the Figs. 5.16 and 5.17.

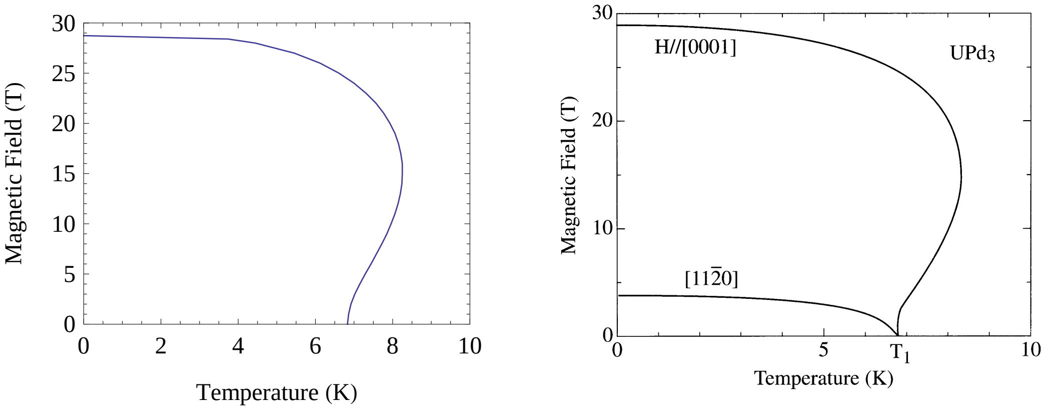

Figure 5.16: Quadrupolar phase diagram calculated in a mean field model of UPd$_3$ with ordering parameter $\langle O_{zx} \rangle$. On the left calculations from this study for a field applied along the c ([0001]) axis are shown, on the right data from Ref. [9]. For details see text.

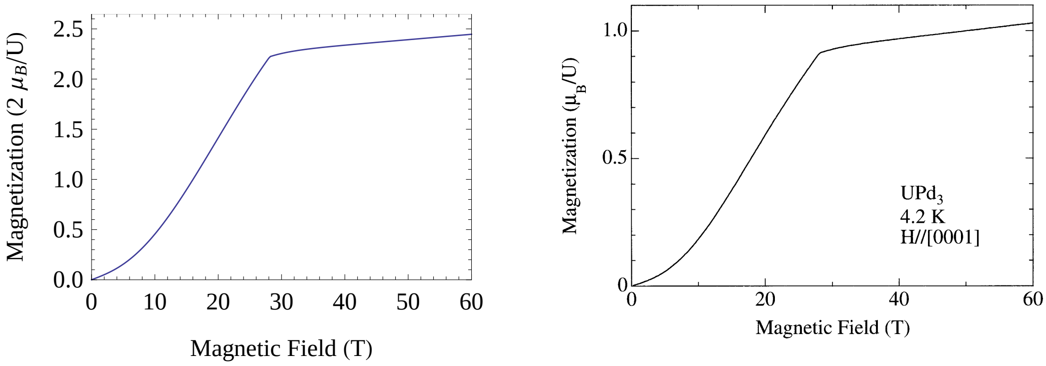

Figure 5.17: Magnetization of UPd$_3$ at T = 4.2 K calculated in this study (left) and from Ref. [9] (right). For details see text.

As can be seen, for this set of CEF parameters and coupling constants, we find a very good agreement of the phase diagrams and magnetization curves. The factor of 2 in our calculated magnetization results from the fact that we have set $M = \langle J_z \rangle$ and only considered the uranium atoms on quasi-cubic sites while neglecting the other half on hexagonal sites. Thus, when taking into account all U atoms the magnetization must be divided by two. From this comparison we conclude that despite the differences in some parameters mentioned above (compare Table 5.3) our model quantitatively and qualitatively reproduces results from Tokiwa *et al.* very well and is therefore correct.

Next, to study the influence of the coupling constants on the phase diagram we have slightly altered the coupling constants, each time leaving one coupling constant (K_2^0 or K_{zx}) unaltered. Some of these phase diagrams with the corresponding parameters are depicted in Fig. 5.18.

From this diagram it is seen that K_{zx} determines the overall ordering temperature and the magnetic field which is necessary to destroy the quadrupolar order. Conversely, K_2^0 does not alter the high field phase boundary but only slightly changes the ordering temperature at low magnetic fields. For a constant value of K_2^0 this shift of the ordering

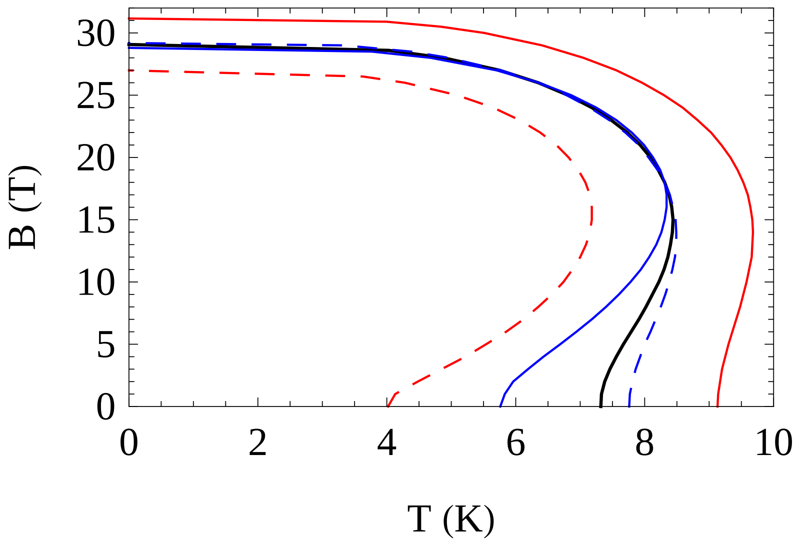

Figure 5.18: Quadrupolar phase diagrams in the simple $\langle O_{zx} \rangle$-model for different coupling constants. Black line calculated with K_2^0 = 0.009 K and K_{zx} = -0.271 meV to reproduce experimental data. Blue and red lines are results for decreased (dashed) and increased (solid) coupling strengths K_2^0 (blue, 0.006 and 0.015 K) and K_{zx} (red, -0.240 and -0.300 meV.

temperature is bigger for smaller values of K_{zx}. Additionally, we find a very interesting result: With K_2^0 = 0.009 K, we obtain a threshold value of K_{zx} = -0.238 meV below which in zero magnetic field no quadrupolar order is observed anymore. For stronger quadrupole-quadrupole interaction (decreasing K_{zx}) the ordering temperature is significantly increased. For instance, this leads to an ordering temperature of 9.13 K already for K_2^0 = 0.009 K and K_{zx} = -0.300 meV. Thus, we conclude that (i) K_{zx} is the more important parameter determining if quadrupolar order occurs at all while K_2^0 only changes the phase boundary and (ii) the system reacts very sensitively to small changes in K_{zx}, especially to a reduction of the coupling constant.

Since the $\langle O_{zx} \rangle$ order parameter is associated with the phase transition at T_0 we finally adjusted the coupling constants to K_2^0 = 0.009 K and K_{zx} = -0.271 meV $\widehat{=}$ -3.14 K. With these values we find the best agreement between our calculated phase boundary and the measured data from Tokiwa *et al.* (Ref. [9]) as it is depicted in Fig. 5.19

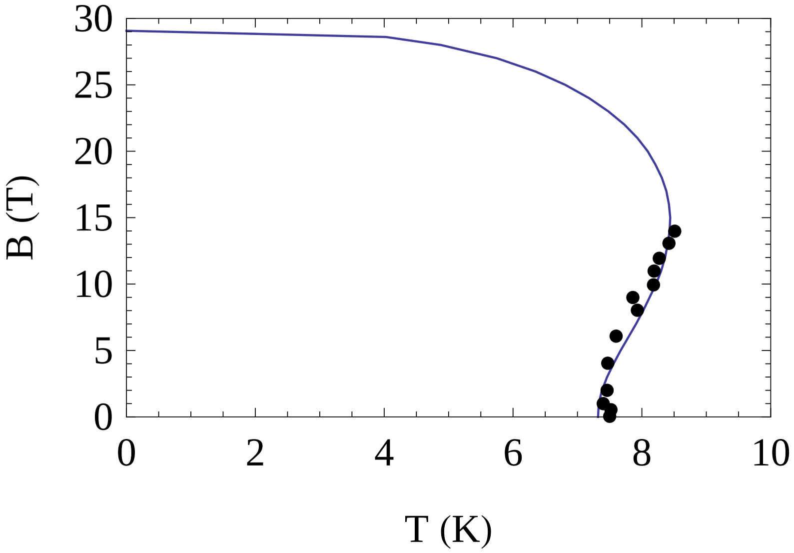

Figure 5.19: Calculated T_0 phase boundary for K_2^0 = 0.009 K and K_{zx} = -3.14 K (solid line), together with the experimental data from Ref. [9].

Finally, for these values of K_2^0 and K_{zx} we have calculated the order parameter $\langle O_{zx} \rangle$ as function of both temperature and magnetic field to visualize the $\langle O_{zx} \rangle$-ordered phase. This set of data is depicted in Fig. 5.20. Here, again we find the phase boundary where $\langle O_{zx} \rangle$ becomes non-zero as it was already depicted in Fig. 5.19. Additionally, two anomalies are observed: First, the order parameter does not constantly increase upon reduction of temperature and/or magnetic field as it is expected for a simple ordered phase but has a minimum value of $\langle O_{zx} \rangle$ = -1.84 at low temperatures around $B \approx$ 16 T marked by the green dot in Fig. 5.15. And second, at low temperatures and in high magnetic fields around $\approx$ 28 T we observe an abrupt change of sign in $\langle O_{zx} \rangle$which corresponds to the change of an elongated to a shortened quadrupolar charge distribution or vice versa .

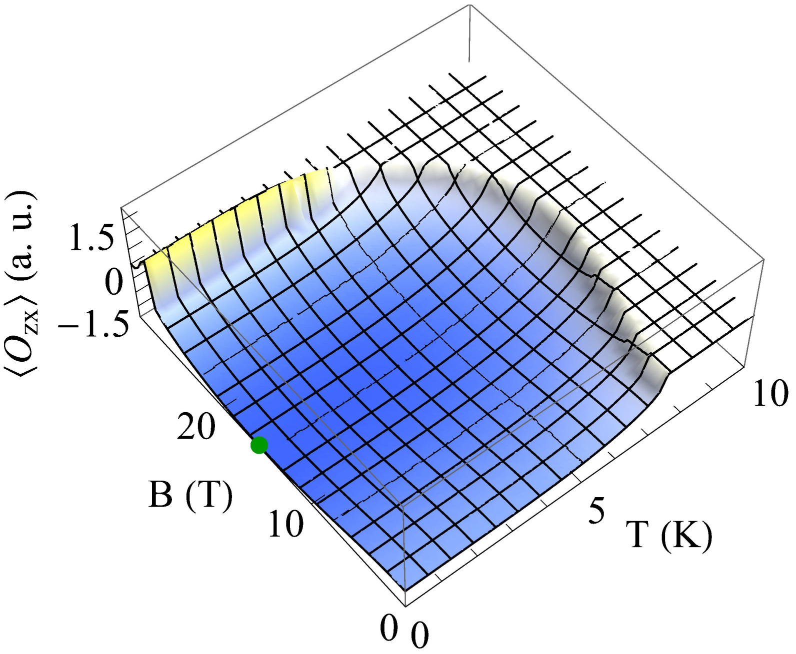

Figure 5.20: The $\langle O_{zx} \rangle$ order parameter vs. temperature and an applied magnetic field for K_2^0 = 0.009 K and K_{zx} = -0.271 meV. The green dot indicates the minimum of the ordering parameter.

$\langle O_{zx} \rangle$ order parameter with doublet ground state

To check the validity of the CEF model with a doublet ground state as proposed by McEwen *et al.* we used the same Hamiltonian as in the previous chapter (Eq. 5.9) but with the altered CEF parameters from table 5.2 [128]. With these parameters we can now again calculate the energies, $J_{z,n}$ and $O_{2,n}^0$ values of the CEF states and compare these to the values found in a singlet ground state scheme. The full set of values obtained this way is summarized in table 5.4

We see that in this scenario the ground state has now become a doublet with an excited singlet at 4 meV or 46 K above as intended by the

Type		Energy		$J_{z,n}$		$O_{2,n}^0$	
$\vert s\rangle$	$\vert d\rangle$	$\vert s\rangle$	$\vert d\rangle$	$\vert s\rangle$	$\vert d\rangle$	$\vert s\rangle$	$\vert d\rangle$
doublet	doublet	533 K	533 K	0.92	1.8	4.5	-5.0
singlet	singlet	508 K	507 K	0.0	0.0	7.0	-10.6
doublet	doublet	437 K	437 K	0.05	1.8	-1.8	-6.6
singlet	singlet	379 K	379 K	0.0	0.0	5.0	7.0
doublet	singlet	18 K	46 K	2.1	0.0	0.3	-2.4
singlet	doublet	0 K	0 K	0.0	3.0	-18.0	14.6

Table 5.4: Calculated energies, $J_{z,n}$ and $O_{2,n}^0$ values for the CEF states calculated in a singlet ($|s\rangle$) and a doublet ($|d\rangle$) ground state scheme. For details see text.

modification of the CEF parameters with the fitting routine described above. Additionally, $J_{z,n}$ and $O_{2,n}^0$ changed as well. If we suppose that this doublet ground state model proposed by McEwen *et al.* in Ref. [128] is correct and calculate the phase diagram we would expect to get similar results as for the CEF scheme with a singlet ground state [128]. However, due to the change of CEF levels the coupling constants need to be altered to produce identical transition temperatures as the singlet ground state model.

As expected, for an appropriate choice of coupling constants we find a quadrupolar ordered phase at low temperatures. However, contrary to our expectations we do not find an increasing ordering temperature upon increasing the applied magnetic field as it is observed experimentally. In our analysis for all combinations of K_2^0 and K_{zx} coupling constants tested we always find a reduction of the ordering temperature upon increasing magnetic field. Additionally, in all cases the order parameter increases with reduction of magnetic field and/or temperature. A typical phase diagram and a plot of order parameter vs. temperature and applied field with coupling constants K_2^0 and K_{zx} are shown in Fig. 5.21. Since K_2^0 has very little effect on this phase diagram we employed the value used in the previous sections. K_{zx} = -0.252 meV has been adjusted to reproduce the ordering temperature of $T_0 = 7.8$ K in zero magnetic field. With these parameters the magnetic field of 4.4 T necessary to supress the quadrupolar order at low temperatures is around one order of magnitude smaller than in the CEF model with a singlet ground state and in the experimental data.

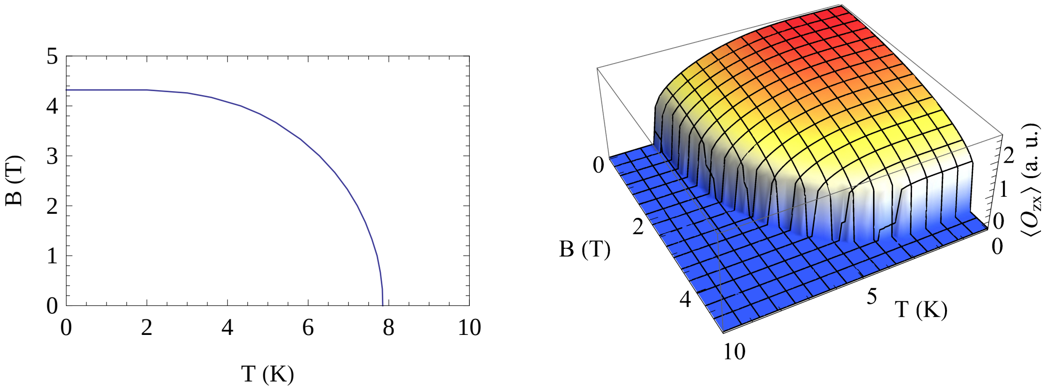

Figure 5.21: Quadrupolar phase diagram and $\langle O_{zx} \rangle$ vs. temperature and applied magnetic field in a doublet ground state CEF scheme for $K_2^0 = 0.009$ K and $K_{zx} = -0.252$ meV.

From these calculations we conclude that, at least in a mean field model, the doublet ground state CEF scheme can not be used to explain the experimentally observed properties of UPd$_3$ while the singlet ground state scheme yields good agreement. Thus, in the following, we will only use the singlet ground state CEF model with the CEF parameters from Tokiwa *et al.* given in Ref. [9] which are depicted in table 5.2.

$\langle O_{xy} \rangle$ order parameter

Now that we have established a basic mean field model which can qualitatively and semiquantitatively account for the observed phase transition at T_0 we will expand this model. In a first step, we exchange the $\langle O_{zx} \rangle$ order parameter with $\langle O_{xy} \rangle$ which is the primary order parameter in the quadrupolar phases below T_1 [131]. Thus, it might be possible to obtain a qualitative understanding of the T_1 and/or T_2 phase transitions. The Hamiltonian of the system then writes as

$$H = H_{CEF} + H_Z - K_2^0 \langle O_2^0 \rangle O_2^0 - K_{xy} \langle O_{xy} \rangle O_{xy} \tag{5.10}$$

where again we take $K_2^0 = 0.009$ K which was found to be in best agreement with experimental data in section 5.4.1 and try different K_{xy}. For all parameter sets we find two equivalent minima at $\pm \langle O_{xy} \rangle$ in the free energy. We have assumed $\langle O_{xy} \rangle > 0$ and plotted the order parameter $\langle O_{xy} \rangle$ vs. temperature and magnetic field for $K_{xy} = 0.208$meV in Fig. 5.22.

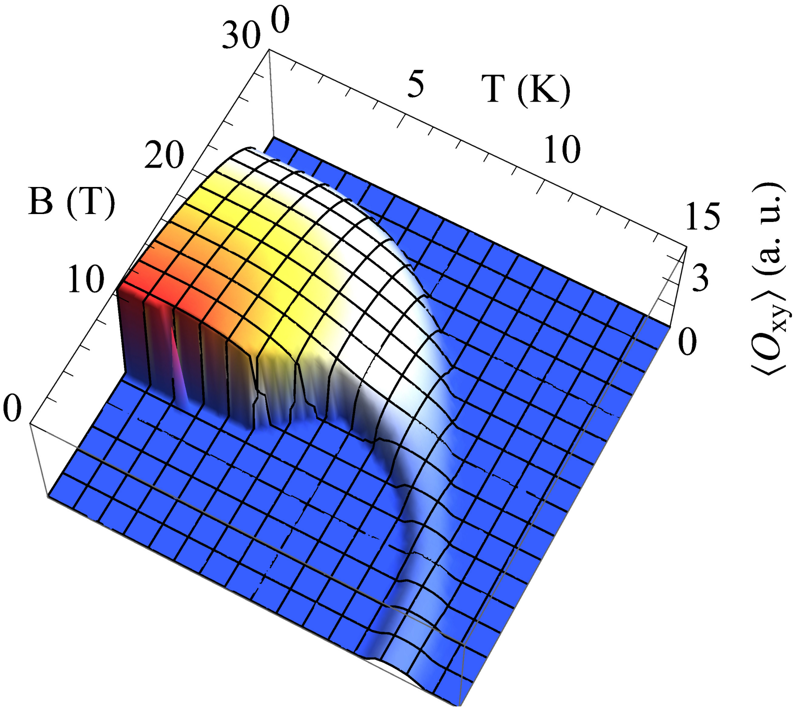

Figure 5.22: $\langle O_{xy} \rangle$ order parameter vs. temperature and an applied magnetic field for $K_{xy} = 0.208$meV.

This phase diagram is quite unusual since we observe a phase which has an order parameter which is non-zero only in a finite temperature and magnetic field range. For small temperatures as well as for small magnetic fields, however, this phase is not stable. Qualitatively such a phase resembles the phase between T_1 and T_2 from the phase diagram in Fig. 5.4, although ordering temperatures are too large by a factor of ≈ 2.

Furthermore, for the case of an $\langle O_{xy} \rangle$-ordered phase we find some very interesting features when varying the K_{xy} coupling constant. First, similar to the observation for the $\langle O_{zx} \rangle$-model, we find a threshold value of $K_{xy} = 0.2074$ meV below which we do not observe any ordered phase in zero magnetic field. Interestingly, this ordered phase is not suppressed to zero with decreasing K_{xy} but vanishes around 12.5 K. Second, the dependence of the ordering temperature on K_{xy} is enormous. While the lower transition temperature is only shifted moderately the upper transition temperature becomes very large already at $K_{xy} = 0.220$ meV ($T_{Ord} = 18$ K). This is shown in Fig. 5.23 where the order parameter $\langle O_{xy} \rangle$ without applied magnetic field is plotted for different values of K_{xy} vs. temperature.

Thus, we find that we have only an extremely narrow interval of K_{xy} values which gives reasonable ordering temperatures. Furthermore, if we assume that the phase between T_1 and T_2 found in UPd$_3$ can be described with this model, the K_{xy} coupling constant is very close to the found threshold value. Thus, the system is even more sensitive to changes of K_{xy} than to changes of K_{zx} which we already found to be very delicate to adjust correctly.

5.4.2 Multiple order parameter models

Since we have now established a model which allows to obtain a qualitative and semiquantitative understanding of some of the properties for single phases of UPd$_3$ we now want to refine our model and allow for multiple competing order parameters. This way our model should reflect

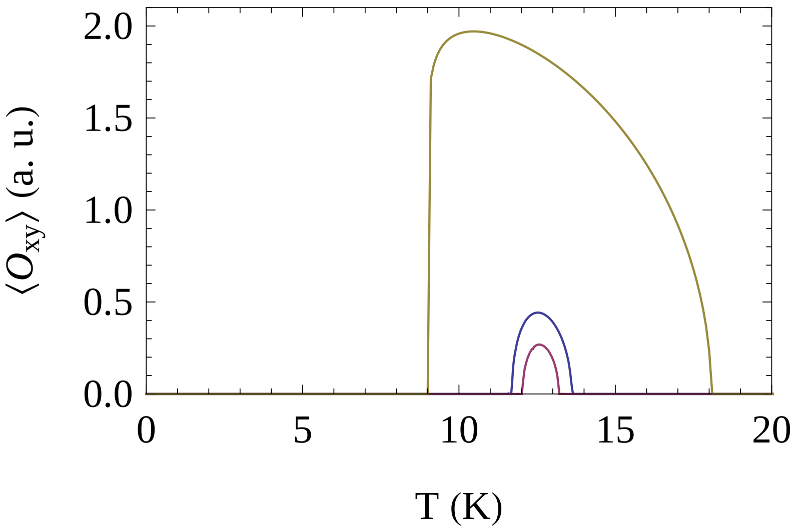

Figure 5.23: $\langle O_{xy} \rangle$ order parameter vs. temperature for coupling constants K_{xy} of 2.076, 2.080 and 2.200 meV (small to large ordered $\langle O_{xy} \rangle$ moment) in zero magnetic field. For details see text.

more appropriately real UPd$_3$ with its complex phase diagram. Before combining different order parameters we will first discuss the symmetry properties of the quadrupole operators which has some implications on the selection of interesting order parameter combinations instead of a random choice.

Symmetry of the quadrupole operators

Since the quadrupole operators O_{zx}, $O_{x^2-y^2}$, O_{xy} and O_{yz} determine the low-temperature magnetic phase diagram it is instructive to calculate them in the basis of the Eigenstates $|n\rangle$ of the system in the absence of order parameters and magnetic field. To do this we take a transformation matrix U which diagonalizes H_{CEF} so that

$$H_{CEF,diagonal} = U^{-1} H_{CEF} U = \begin{pmatrix} E_1 & 0 & \cdots & 0 \\ 0 & \ddots & \ddots & \vdots \\ \vdots & \ddots & \ddots & 0 \\ 0 & \cdots & 0 & E_9 \end{pmatrix} \tag{5.11}$$

and apply this transformation to our quadrupole operators. Since only the three lowest CEF levels contribute significantly at low temperatures we can reduce these matrices to the upper left 3x3 submatrices which determine the physics of the three low energy CEF states to get an impression of how these operators influence the system[2]. We then find that these matrices have the form

$$O_{zx,red} = \begin{pmatrix} 0 & A & -A \\ A & 0 & B \\ -A & B & 0 \end{pmatrix} \qquad O_{x^2-y^2,red} = \begin{pmatrix} 0 & A' & -A' \\ A' & 0 & B' \\ -A' & B' & 0 \end{pmatrix} \tag{5.12a}$$

$$O_{xy,red} = -\frac{1}{2} \begin{pmatrix} 0 & iA' & iA' \\ -iA' & 0 & iB' \\ -iA' & -iB' & 0 \end{pmatrix} \qquad O_{yz,red} = \begin{pmatrix} 0 & iA & iA \\ -iA & 0 & iB \\ -iA & -iB & 0 \end{pmatrix} \tag{5.12b}$$

As we can see and as it was already pointed out by McEwen *et al.* in Ref. [128] there exist only 2 symmetries of these operators which are shared by a pair of quadrupole operators each [128]. That are the symmetries shared by O_{zx} and $O_{x^2-y^2}$, and by O_{xy} and O_{yz}, respectively. This implies that a non-zero expectation value of one order parameter leads to a finite expectation value of the second order parameter with the same symmetry.

In case we take the complete hamiltonian H instead of H_{CEF} in Eq. 5.11 and allow for a magnetic field the situation becomes more complex.

---

[2] This reduction to a 3x3 matrix is only done here to better visualize the symmetry properties of the operators. All numerical calculations were performed using the full 9x9 matrices including magnetic field and order parameters.

Since the degeneracy of the doublet is lifted a third value (C/C') replaces $-A/-A'$ and the diagonal elements may become non-zero because of $\langle O_i \rangle = \mathrm{Tr}(O_i)$.

However, the finding that the pairs of quadrupole operators with same symmetry become zero or non-zero together remains true even in this general case. This will be shown in more detail in the following sections where we allow terms for quadrupole operators of the same symmetry in the Hamiltonian.

$\langle O_{zx} \rangle$ and $\langle O_{x^2-y^2} \rangle$ order parameters

If we now combine our primary order parameter $\langle O_{zx} \rangle$ at the T_0 phase transition with $\langle O_{x^2-y^2} \rangle$ which has the same symmetry, the Hamiltonian of the system becomes

$$\begin{aligned} H = H_{CEF} + H_Z - K_2^0 \langle O_2^0 \rangle O_2^0 \\ - K_{zx} \langle O_{zx} \rangle O_{zx} - K_{x^2-y^2} \langle O_{x^2-y^2} \rangle O_{x^2-y^2}. \end{aligned} \tag{5.13}$$

For the coupling constants we start with $K_2^0 = 0.009$ K and $K_{zx} =$ -0.271 meV, which produces good agreement with experimental data for the single-order-parameter model, and try different $K_{x^2-y^2}$. We find that already for a very small $K_{x^2-y^2} = 0.0001$ meV we find an order parameter $\langle O_{x^2-y^2} \rangle$ which has comparable magnitude to $\langle O_{zx} \rangle$. Upon reduction of $K_{x^2-y^2}$ below 0.0001 meV $\langle O_{x^2-y^2} \rangle$ is not significantly altered. Instead, with increasing $K_{x^2-y^2}$ above 0.0001 meV $\langle O_{x^2-y^2} \rangle$ becomes significantly larger, in particular larger than $\langle O_{zx} \rangle$.

Since Walker *et al.* experimentally found a ratio of 6:1 for $\langle O_{zx} \rangle$: $\langle O_{x^2-y^2} \rangle$ (Ref. [131]) we take a small value of $K_{x^2-y^2} = 0.0001$ meV which in our model gives $\langle O_{zx} \rangle : \langle O_{x^2-y^2} \rangle \approx$ 1:1 and is thus the closest agreement we find to Ref. [131]. Even for smaller $K_{x^2-y^2}$ this ratio remains almost unchanged. Since the ordering temperatures are slightly shifted to 7.3 K with $K_{zx} =$ -0.271 meV by including a second

$\langle O_{x^2-y^2}\rangle$ order parameter we modify K_{zx} to -0.278 meV to compensate for this shift. For this set of coupling constants ($K_2^0 = 0.009$ K, K_{zx} = -0.278 meV and $K_{x^2-y^2}$ = 0.0001 meV) we have plotted both order parameters vs. temperature in zero magnetic field in Fig. 5.24. In Fig. 5.25 both order parameters are shown for different temperatures and magnetic fields.

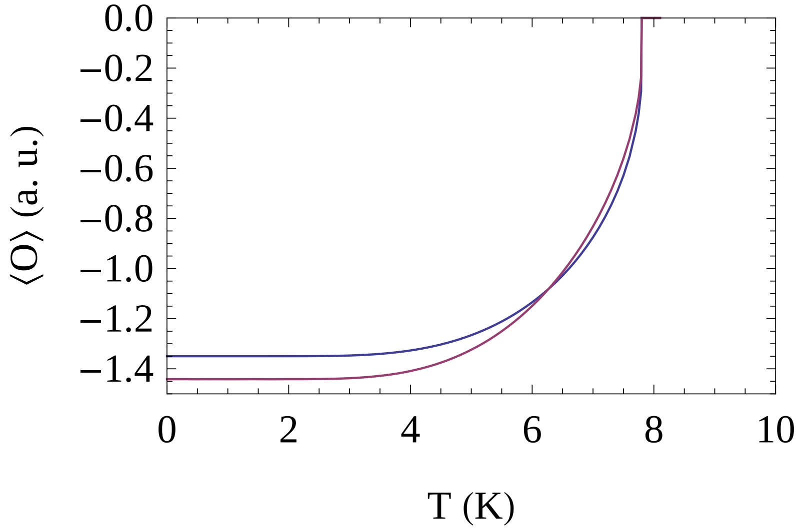

Figure 5.24: $\langle O_{zx}\rangle$ (blue) and $\langle O_{x^2-y^2}\rangle$ (purple) order parameters for a set of coupling constants $K_2^0 = 0.009$ K, K_{zx} = -0.278 meV and $K_{x^2-y^2}$ = 0.0001 meV chosen to reproduce the experimentally determined transition temperature T_0.

We find that both order parameters, $\langle O_{zx}\rangle$ and$\langle O_{x^2-y^2}\rangle$, become zero or non-zero simultaneously which is consistent with our symmetry considerations in section 5.4.2 and Ref. [128].

Although we get slightly shifted ordering temperatures (or coupling constants) and a different ratio of ordering parameters than proposed the phase diagram remains almost identical to the one found with only an $\langle O_{zx}\rangle$ order parameter in section 5.4.1. We thus conclude that the mixed $\langle O_{zx}\rangle$-$\langle O_{x^2-y^2}\rangle$-model is more complex than the simple $\langle O_{zx}\rangle$-model but has no additional features and hence gives qualitatively the

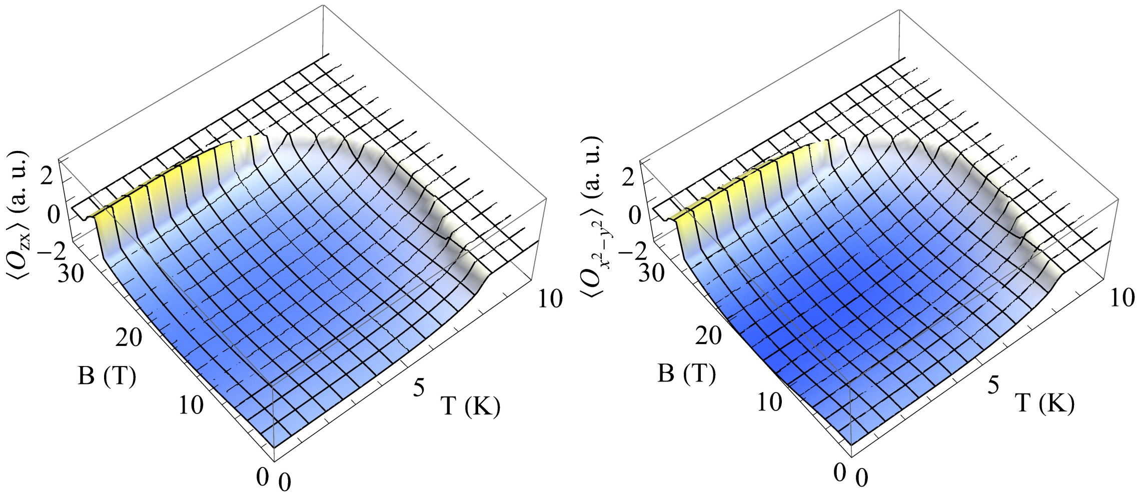

Figure 5.25: $\langle O_{zx} \rangle$ and $\langle O_{x^2-y^2} \rangle$ order parameters for the two-parameter mean field model.

same and quantitatively very similar results. Therefore, to understand UPd$_3$ it seems not to be necessary to include an $O_{x^2-y^2}$-term.

$\langle O_{xy} \rangle$ and $\langle O_{yz} \rangle$ order parameters

Similar to the previous case we now consider the second pair of ordering parameters of the same symmetry, $\langle O_{xy} \rangle$ and$\langle O_{yz} \rangle$. In this case the Hamiltonian is

$$H = H_{CEF} + H_Z - K_2^0 \langle O_2^0 \rangle O_2^0 - K_{xy} \langle O_{xy} \rangle O_{xy} - K_{yz} \langle O_{yz} \rangle O_{yz}. \quad (5.14)$$

As in the previous section we find a very small shift of the ordering temperatures due to the second $\langle O_{yz} \rangle$ order parameter. Since here the shift is less than 0.1 K we do not adjust the K_{xy} coupling constant but maintain $K_{xy} = 0.208$ meV. Again, when varying the additional K_{yz} coupling constant we find an approximately constant ratio $\langle O_{xy} \rangle : \langle O_{yz} \rangle$ of $\approx$ 4:1 for very small values of K_{yz}. For larger values of K_{yz} this ratio becomes smaller, thus it is moving farther from the experimentally found values of 8:1 and 14:1 for the quadrupolar ordered phases at $T < T_2$ and

$T_2 < T < T_1$, respectively [131]. Therefore, we set $K_{yz} = 0.0001$ meV and calculate the order parameters vs. temperature without and with applied magnetic field as it is depicted in Figs. 5.26 and 5.27. Again, for $\langle O_{xy} \rangle$ we find two equivalent minima in the free energy and assume $\langle O_{xy} \rangle > 0$.

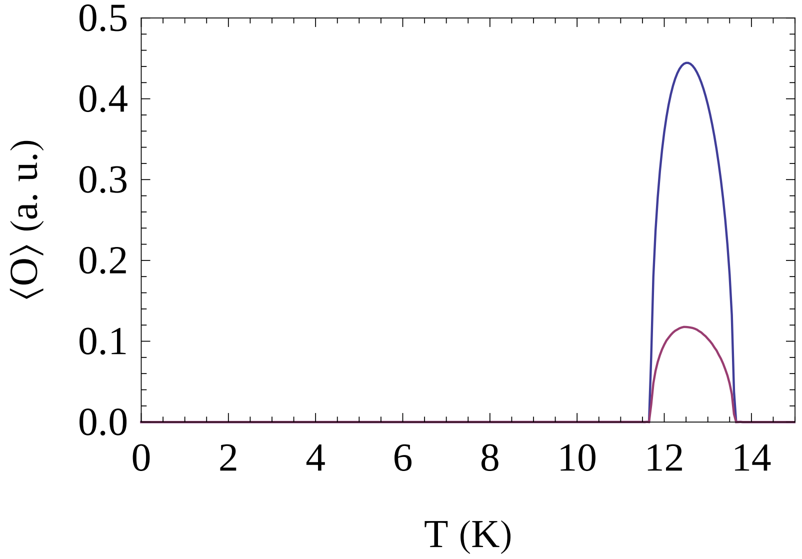

Figure 5.26: $\langle O_{xy} \rangle$ (blue) and $\langle O_{yz} \rangle$ (purple) order parameters for a set of coupling constants $K_2^0 = 0.009$ K, $K_{xy} = 0.208$ meV and $K_{yz} = 0.0001$ meV.

For the mixed $\langle O_{xy} \rangle$-$\langle O_{yz} \rangle$-model we find, similar to the $\langle O_{zx} \rangle$-$\langle O_{x^2-y^2} \rangle$-model, that the ordering parameters become zero or non-zero simultaneously which again is consistent with our symmetry considerations and Ref. [128]. As in the $\langle O_{zx} \rangle$-$\langle O_{x^2-y^2} \rangle$ case the introduction of a second order parameter of the same symmetry does not alter the results of the mean field model qualitatively, and even quantitative changes are neglegible here. Hence, at this point it does not seem to be necessary to include an O_{yz} operator in the Hamiltonian to further study UPd$_3$.

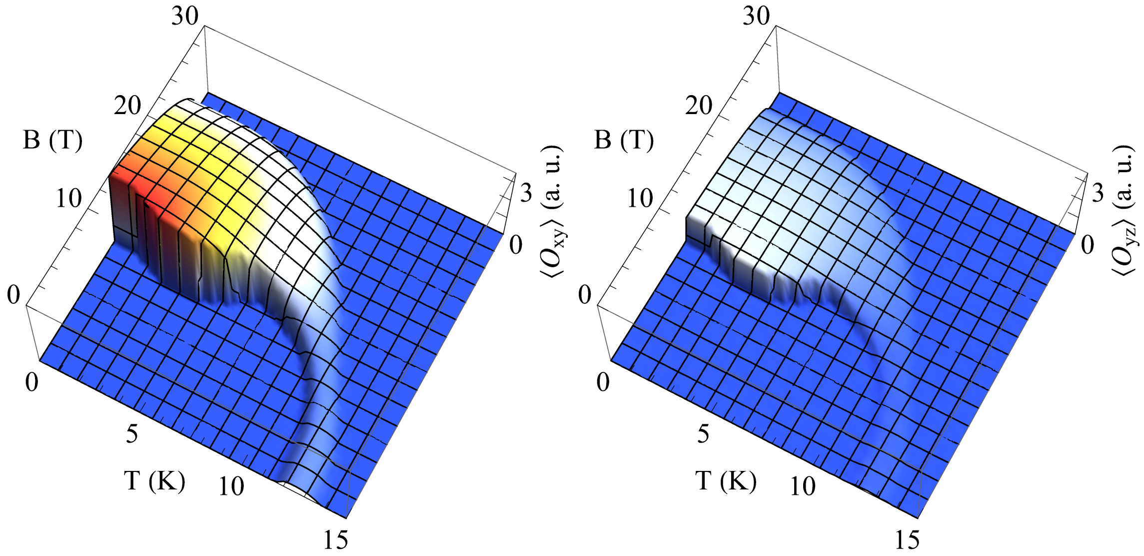

Figure 5.27: $\langle O_{xy} \rangle$ and $\langle O_{yz} \rangle$ order parameters for the 2-parameter mean field model.

$\langle O_{zx} \rangle$ and $\langle O_{xy} \rangle$ order parameters

Since we have now studied the interaction of order parameters of the same symmetry and found the differences to the single-order-parameter-models to be small we will now combine quadrupole operators with different symmetry. Since the dominant quadrupole moments found experimentally are $\langle O_{zx} \rangle$ and $\langle O_{xy} \rangle$ we will include these two in the Hamiltonian which is then

$$H = H_{CEF} + H_Z - K_2^0 \langle O_2^0 \rangle O_2^0 - K_{zx} \langle O_{zx} \rangle O_{zx} - K_{xy} \langle O_{xy} \rangle O_{xy}. \quad (5.15)$$

This Hamiltonian might give rise to multiple quadrupolar ordered phases in one model. However, since the expectation value of one order parameter influences the Eigenvalues of H and thus the expectation value of the other order parameter, some interaction between these order parameters is possible. As in the previous sections we set K_2^0 to 0.009 K which reproduced experimental data in the single order parameter $\langle O_{zx} \rangle$-model.

Further, we then varied the K_{zx} and K_{xy} coupling constants, starting with the parameters found to be suitable for the single order parameter models. Since we found that changing K_{xy} has very little influence on the $\langle O_{zx}\rangle$-ordered phase we first left K_{xy} at 0.208 meV while only varying K_{zx}.

Without an applied magnetic field we can find two phases which are either separated by a temperature range without any order parameter or directly connected to each other depending on the choice of coupling constants. Some examples for this behaviour are depicted in Fig 5.28.

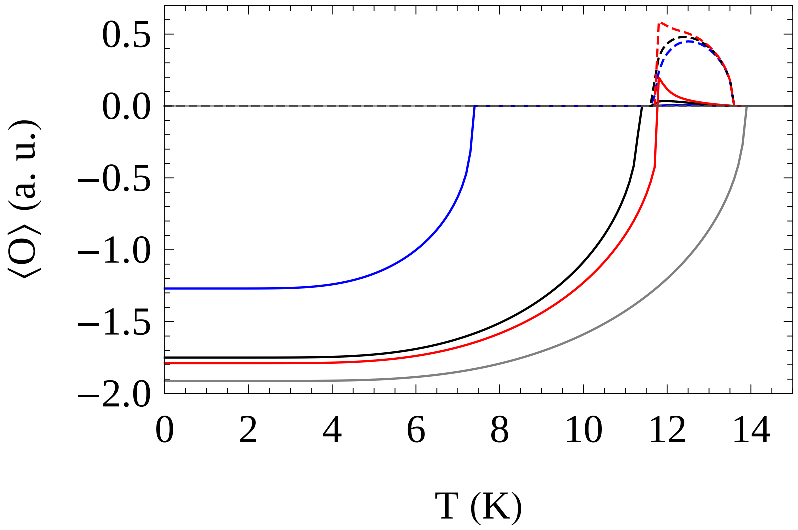

Figure 5.28: $\langle O_{zx}\rangle$ (solid) and $\langle O_{xy}\rangle$ (dashed) oder parameters for $K_2^0 = 0.009$ K, $K_{xy} = 0.208$ meV and K_{zx} = -0.271 (blue), -0.340 (black), -0.350 (red) and -0.390 meV (gray) calculated in the $\langle O_{zx}\rangle$-$\langle O_{xy}\rangle$-mean field model.

Again, as in the single order parameter models, we find threshold values of K_{zx} = -0.237 meV and K_{xy} = 0.2075 meV below which no ordered phases exist. However, now we always find $\langle O_{zx}\rangle > 0$ when $\langle O_{xy}\rangle$ becomes non-zero. Interestingly, this is also the case when K_{zx} is smaller than the threshold value. For such a combination of parameters we find $\langle O_{zx}\rangle = 0$ at low temperatures and $\langle O_{zx}\rangle > 0$ within the $\langle O_{xy}\rangle$-

ordered phase (black lines in Fig. 5.28).

Since in experiments on UPd$_3$ below T_0 finite order parameters are found at all temperatures we first set our coupling constants to K_{zx} = -0.350 meV and K_{xy} = 0.208 meV in order to get low ordering temperatures and a finite order parameter for all temperatures below the highest ordering temperature. With these parameters we can now calculate $\langle O_{zx}\rangle$ and $\langle O_{xy}\rangle$ for all temperatures and magnetic fields, and which is shown in Fig. 5.29.

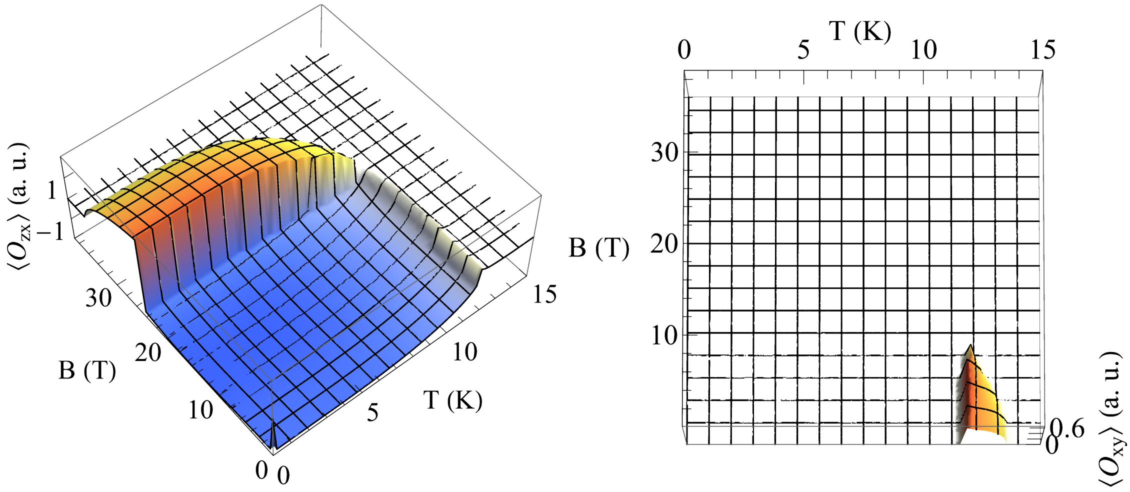

Figure 5.29: $\langle O_{zx}\rangle$ and $\langle O_{xy}\rangle$ order parameters for the set of coupling constants $K_2^0 = 0.009$ K, K_{zx} = -0.350 meV and K_{xy} = 0.208 meV.

From this calculation, we find multiple ordered phases with different order parameters. In particular, we observe that the outer phase boundary of the $\langle O_{zx}\rangle \neq 0$ phase is not significantly influenced by the vanishing additional phases at higher magnetic fields or temperatures. Moreover, we observe a region 10 T $< B <$ 20 T where a direct transition from the $\langle O_{zx}\rangle < 0$ ordered phase to the disordered state exists, thus the $\langle O_{xy}\rangle$-ordered and the $\langle O_{zx}\rangle > 0$-ordered phases are not directly connected for this set of coupling constants.

Since the mean field model would resemble the phase diagram of UPd$_3$ more closely if the high field and high temperature phases ($\langle O_{zx}\rangle > 0$ and $\langle O_{xy}\rangle > 0$) would be directly connected we increased K_{xy} in order to find a possible connection between both phases. Therefore, the order parameters for a different set of coupling constants of $K_2^0 = 0.009$ K, K_{zx} = -0.344 meV and K_{xy} = 0.230 meV are depicted in Fig. 5.30.

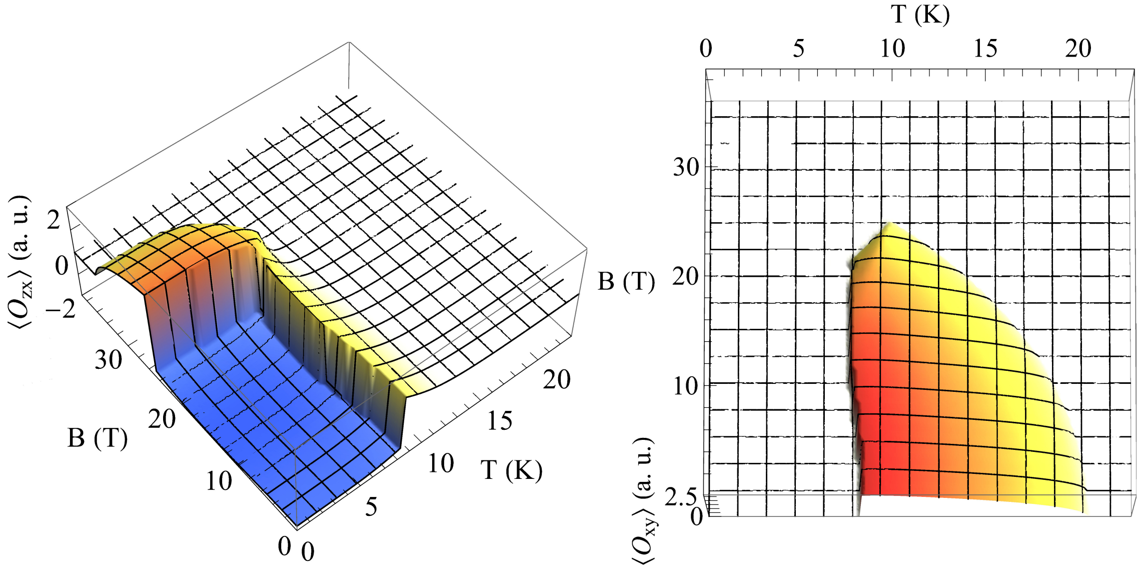

Figure 5.30: $\langle O_{zx}\rangle$ and $\langle O_{xy}\rangle$ order parameters for the set of coupling constants $K_2^0 = 0.009$ K, K_{zx} = -0.344 meV and K_{xy} = 0.230 meV.

In contrast to the previous case, now we find a connection of the high field and high temperature phases. However, the zero field ordering temperatures have also increased significantly to ≈ 21 K, which is even above the experimentally observed ordering temperatures in UPd$_3$ than those obtained with the smaller K_{xy}. Nevertheless, ordering temperatures are still reasonable and of the same order of magnitude as experimentally observed. Interestingly, in this combination of coupling constants we do not observe a continuous phase transition line as in the simple

$\langle O_{zx}\rangle$ ordered phase before, but now two points exist at which three phase transition lines join with discontinuous slopes. Additionally the lower phase transition in zero field is now shifted to lower temperatures with an applied magnetic field, in contrast to the previous case where it was shifted to higher temperatures. These phase diagrams will be discussed in more detail in section 5.5.

$\langle O_{zx}\rangle$, $\langle O_{x^2-y^2}\rangle$, $\langle O_{xy}\rangle$and $\langle O_{yz}\rangle$ order parameters

In order to test if the two omitted order parameters $\langle O_{x^2-y^2}\rangle$ and $\langle O_{yz}\rangle$ have a significant influence on the $\langle O_{zx}\rangle$- and $\langle O_{xy}\rangle$-ordered phases in the $\langle O_{zx}\rangle$-$\langle O_{xy}\rangle$-model we have calclulated the order parameters for the full set of considered quadrupole operators in a final step. The Hamiltonian of the system now becomes

$$\begin{aligned} H =& H_{CEF} + H_Z - K_2^0 \langle O_2^0\rangle O_2^0 \\ & - K_{zx} \langle O_{zx}\rangle O_{zx} - K_{x^2-y^2} \langle O_{x^2-y^2}\rangle O_{x^2-y^2} \\ & - K_{xy} \langle O_{xy}\rangle O_{xy} - K_{yz} \langle O_{yz}\rangle O_{yz}. \end{aligned} \tag{5.16}$$

where we have set the coupling constants to the values $K_2^0 = 0.009$ K, K_{zx} = -0.278 meV, K_{xy} 0.208 meV, $K_{x^2-y^2} = 0.0001$ meV and $K_{yz} = 0.0001$ meV that were found to give reasonable results in the mixed $\langle O_{zx}\rangle$-$\langle O_{xy}\rangle$-, $\langle O_{zx}\rangle$-$\langle O_{x^2-y^2}\rangle$- and $\langle O_{xy}\rangle$-$\langle O_{yz}\rangle$-models. The whole set of ordered parameters vs. temperature and applied magnetic field is shown in Fig. 5.31

In these plots we do not observe significant differences to the simpler $\langle O_{zx}\rangle$-$\langle O_{xy}\rangle$-model. Again, ordering temperatures and magnetic fields are shifted slightly due to the additional order parameters, and order parameters of the same symmetry become zero or non-zero simultanously. But as expected, the overall phases diagram is not altered significantly.

Thus, in the mean field modelling under consideration here, it is justified to omit the $\langle O_{x^2-y^2}\rangle$ and $\langle O_{yz}\rangle$ order parameters to explore the

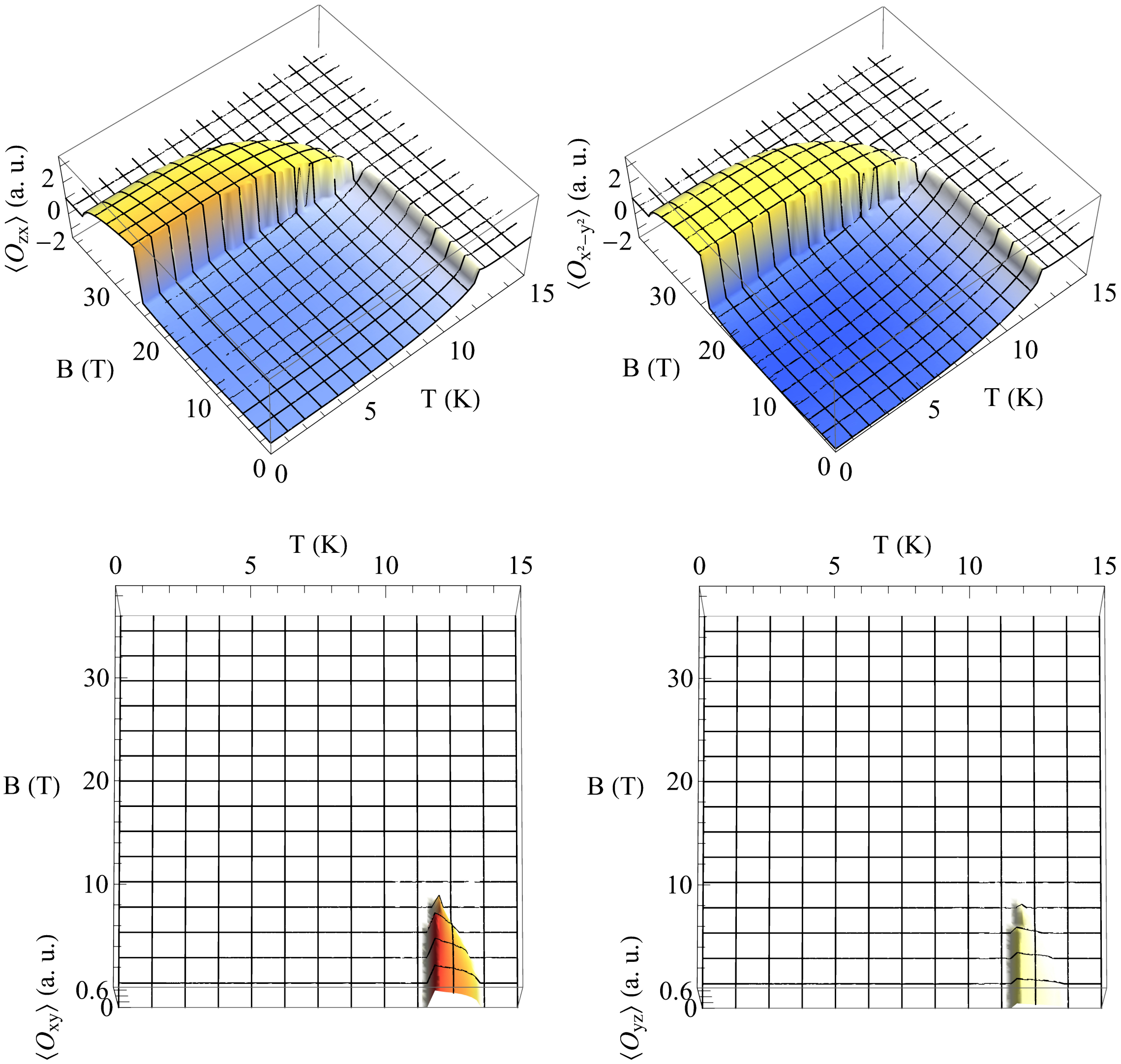

Figure 5.31: Different order parameters vs. temperature and magnetic field for a mean field model including $\langle O_{zx}\rangle$, $\langle O_{x^2-y^2}\rangle$, $\langle O_{xy}\rangle$ and $\langle O_{yz}\rangle$ as possible order parameters.

properties of UPd$_3$. This is extremely helpful, in particular in the numerical calculations, since with the full set of order parameters the numerical routines become very time-consuming and unstable, often ending up only at a local minimum of the free energy.

5.5 Discussion

Now, we will further focus on the $\langle O_{zx}\rangle$-$\langle O_{xy}\rangle$-models. In a next step, we can draw schematic phase diagrams for the two scenarios corresponding to the two the different sets of coupling constants discussed above. These are depicted in Fig. 5.32. Obviously, the phase diagram on the right in Fig. 5.32 resembles the experimental phase diagram more closely, we will thus continue by comparing the right schematic phase digram with the experimental one.

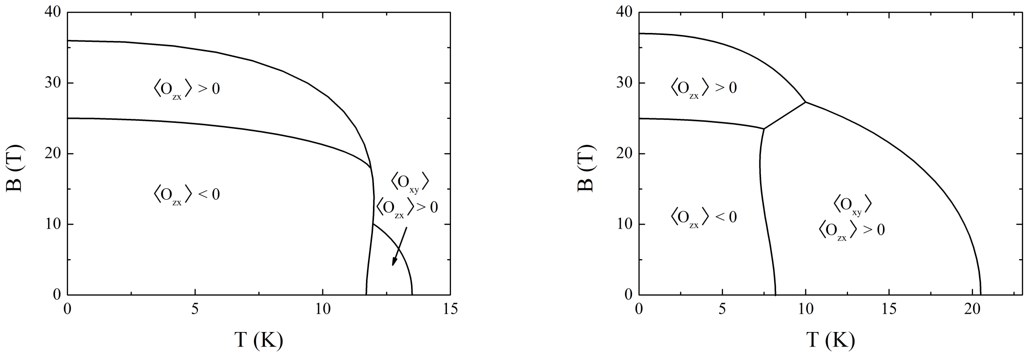

Figure 5.32: Schematic magnetic phase diagrams of UPd_3 from mean field models including $\langle O_{zx}\rangle$ and $\langle O_{xy}\rangle$ order parameters for different sets of coupling constants and magnetic fields applied along the *c* axis; for details see text.

In this comparison of the phase diagrams found in the mean field model (Figs. 5.29 and 5.32) and experimentally (Fig. 5.4 [9]) we observe a complex phase diagram in both cases, and which partially resemble each other. Still there are some differences. To better visualize the resemblances and differences we plot our schematic mean field model phase diagram together with the experimentally found one from Tokiwa *et al.* (Ref. [9]) which we have extended with the quadrupolar order parameters as determined by Walker *et al.* (Ref. [131]). This comparison is depicted in Fig. 5.33.

For both, experiment as modelling at very low temperatures, we find 2 phase transitions upon increasing magnetic field. Instead, in zero field with increasing temperature we find only 2 phase transitions in our model when adjusting the coupling constants to have a finite order parameter at all temperatures below the highest ordering temperature, while in experiments three phase transitions[3] are observed. When adjusting the coupling constants in our model to reproduce three phase transitions we always find a temperature range without any order parameter, which means we separate the $\langle O_{zx}\rangle$ and $\langle O_{xy}\rangle$ ordered phases in our schematic phase diagram which as well does not reproduce the experimental data correctly. Depending on the choice of coupling constants the phase transition at lower temperatures in zero field (from the $\langle O_{xy}\rangle$- to the $\langle O_{zx}\rangle < 0$ ordered phase) can be shifted either to higher or lower temperatures with an applied magnetic field.

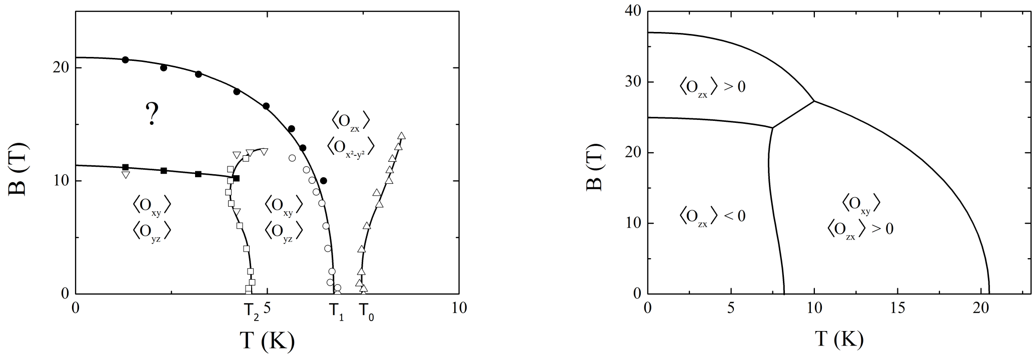

Figure 5.33: Experimentally determined magnetic phase diagram for fields applied along the c axis from Ref. [9] with the quadrupolar order parameters included as determined in Ref. [131] (left, below T_1 and T_2 order parameters are identical but with changing ratio at T_2) and respective schematic phase diagram as determined in a mean field model including $\langle O_{zx}\rangle$ and $\langle O_{xy}\rangle$ order parameters with the coupling constants chosen to resemble experimental data.

If we take into account the types of order parameters we find an-

---

[3] Here we treat the T_{-1} and T_{+1} phase transitions as one T_1 phase transition

other difference: In experiments it was shown that the dominant order parameters of the different phases are $\langle O_{zx} \rangle$ for $T_1 < T < T_0$ and $\langle O_{xy} \rangle$ for $T < T_1$ while in our model we find for the ordering temperatures $T_{\langle O_{xy} \rangle} > T_{\langle O_{zx} \rangle}$ [131]. However, especially the schematic phase diagram with increased K_{xy} (Figs. 5.32 or 5.33, right) closely resembles the area of the phase diagram below T_1 and T_2 although all temperatures and magnetic fields are too large by a factor of 2-3 and the order parameter at lowest temperatures in zero field is different. However, if we neglect the different order parameters between experiment and modeling and identify our calculated phase transitions in the mean field model with T_1 and T_2 we find no signatures of the T_0 transition at higher temperatures in our calculations. Given this assignment of the transition temperatures is true from our calculations we would expect the experimentally found field induced phase from 12 to 21 T for which the quadrupolar order parameters have not yet been identified to be similar to the phase at lower fields but with a change of sign of the order parameter at 12 T.

All together, our mean field models yield very good results for a single $\langle O_{zx} \rangle$ order parameter in agreement with experimental data. For the single $\langle O_{xy} \rangle$ order parameter we obtain a good qualitative description of a phase with an order parameter only for finite temperatures and/or magnetic fields which resembles the quadrupolar ordered phase between T_1 and T_2. And finally, for models with multiple order parameters, we find a complex quadrupolar phase diagram with multiple ordered phases which resembles the experimentally found ones although some differences still exist.

We thus conclude that the studied mean field models indeed do reflect the physics of UPd$_3$ although quantitative results are strongly dependent on the choice of coupling constants, especially in models with multiple order parameters. Hence, the choice of coupling constants might already be the explanation for the observed quantitative differences. Unfortunately, since testing different coupling constants is very time consuming only a limited number of combinations of coupling constants could be tested and the "correct" set of coupling constants might not have been found yet. Another possible reason for the differences between calculations and experiments is that we omitted mixed terms as in Eq. 5.5 that allow for a direct interaction between different quadrupoles. Including such terms might change the phase diagram but at the cost of additional coupling constants which again makes the calculations less stable and much more time-consuming.

Since our mean field models can qualitatively account for some of the properties of UPd_3 the question arises how to explain the observed strong reduction of ordering temperatures in $U(Pd_{1-x}Pt_x)_3$ upon increased alloying level x in this model? And furthermore, is it possible to explain the absence of long-range order within the same model, or do we have to propose that this model breaks down between the alloying parameters $x = 0.5\%$ and $x = 1\%$? In the following we will discuss two possibilities to explain the experimentally observed properties: First (i), a glass-like scenario where clusters of undisturbed neighbouring UPd_3 unit cells become disturbed by Pt and too small for long-range order. And second (ii), a scenario where the increasing hybridization between Pt $5d$ and U $5f$ electrons causes the observed changes.

From our calculations we find a threshold value for all coupling constants very close to the values used. This way, in our model, even a small reduction of the coupling constants by some percent would lead to a complete suppression of the ordered phases and an even smaller reduction could already cause a strong reduction of ordering temperatures as observed. This finding is independent of the reason for a reduced quadrupole-quadrupole coupling, but the question arises about the microscopic origin of this reduction?

If we now assume in a first model (i), that we have a glass-like state where the platinum content in U(Pd$_{1-x}$Pt$_x$)$_3$ leads to the reduction of the effective quadrupole-quadrupole interaction strengths, whatever the mechanism of this reduction might be, then the clusters of ordered undisturbed UPd$_3$ become smaller due to the added Pt content until no long range order is observed any more and the clusters are decoupled. This would be consistent with the observations of suppression of long range order with increasing x [110, 111].

We have two inequivalent U sites (hexagonal and quasi-cubic) in UPd$_3$ while the quadrupolar order takes place only on the quasi-cubic sites. With every 200th Pd atom exchanged with Pt at $x = 0.5\%$ and each U atom surrounded by 12 Pd or Pt atoms we already find that every 17th ($\approx \frac{200}{12}$) U atom has one neighbouring Pt atom in U(Pd$_{1-x}$Pt$_x$)$_3$ at $x = 0.5\%$. This means that for one arbitrary direction in the crystal every second to third U atom is influenced by neighbouring Pt even if we assume that only shortest uranium-paladium distances need to be taken into account. Since our model assumes an interaction between the quadrupoles situated at the quasi-cubic uranium sites we additionally need neighbouring undisturbed quasi-cubic U sites to observe order exactly as in UPd$_3$. With every 17th U atom being situated next to a Pd or Pt atom and 6 neighbouring U sites for the quasi-cubic symmetry of the ordering U sites this means that only about 60% of the ordering U sites are undisturbed and surrounded by other undisturbed U atoms and are hence in exactly the same environent as in UPd$_3$. In other words this means that long range order should already be strongly influenced by alloying levels as low as $x = 0.5\%$ while possible short range order is influenced very little. If we additionally assume that the quadrupole-quadrupole coupling might be influenced by atoms in between the ordering quadrupoles and that in the dhcp crystal structure the non ordering hexagonal U sites with additional Pd (Pt) atoms are situated in between the ordering quasi-cubic sites the situation might become even worse. Thus, in this scenario of a glass-like state many of the U atoms are influenced already for Pt conenctrations as low as 0.5% in $U(Pd_{1-x}Pt_x)_3$. However, still some of the quasi-cubic U sites are undisturbed and also surrounded by undisturbed neighbouring U atoms and should order as in UPd_3. On the other hand the quadrupolar order for small x is long range order and might be strongly influenced by the formation of smaller undisturbed domains as described above and ordering temperatures might thus be strongly influenced by the introduction of platinum in the system.

If we extend this explanation to the $U(Pd_{1-x}Pt_x)_3$ samples with $x = 1\%$ we find already every 8th U atom next to a Pt atom which is equivalent to every second U atom in an arbitrary direction being influenced by a neighbouring Pt atom. This causes a situation where it is already highly improbable to find a U atom which is only surrounded by Pd atoms and which additionally has neighbouring U atoms for which the same is true. Now, if we assume that it is necessary to find such an arrangement of completely undisturbed U sites to produce long range order we would expect long range order to be suppressed with $x = 1\%$ as it is observed in the experiments.

Furthermore, since we consider a direct exchange between neighbouring quadrupoles which is not mediated by other atoms or electrons the Pt atoms should only have little effect, in particular since only one out of 12 Pd atoms is exchanged with Pt. On the other hand, due to the spatially more extent Pt $5d$ wavefunctions the U $5f$ electrons could indeed be influenced and might for instance be tilted. If we consider UPd_3 as a system where the Pd $4d$ wavefunctions are too small to have an effect on the U $5f$ electrons then indeed one single Pt atom in the surrounding could cause a difference in the quadrupole moment of the centering U atom. However, since at $x = 0.5\%$ still some of the quasi-cubic U sites are undisturbed we would expect to see order as in UPd_3 at least for some domains unless we propose that the quadrupolar order at undisturbed U sites is already suppressed when only neighbouring quasi-cubic or non-ordering U atoms are influenced by Pt atoms. Of course the ordering temperatures might be reduced due to the smaller spatial extent of the homogenuously and undisturbed ordered domains. On the other hand, if we assume such an extreme sensitivity of the quadruplar coupling to the alloying parameter x, this high sensitivity should lead to a complete suppression of order for the doubled Pt content at $x = 1\%$. This in contrast to the specific heat data where we still osberve a broad anomaly indicating short range order at $x = 1\%$.

Thus, it is possible to explain the observed reduction of ordering temperatures at $x = 0.5\%$ and the suppression of long range-order at $x = 1\%$ in a glass-like picture but this requires to assume an extraordinary strong effect of the Pt atoms in $U(Pd_{1-x}Pt_x)_3$. From our and published data we can not finally rule out this scenario, although it seems very unlikely due to this enormous effect of Pt alloying, which can hardly be explained by a simple physical mechanism in a localized electronic picture of $U(Pd_{1-x}Pt_x)_3$.

In the second scenario (ii) proposed by Walker *et al.* we can assume that the introduction of platinum in $U(Pd_{1-x}Pt_x)_3$ drives the system from the strongly localized $5f$-state in UPd_3 in the direction of UPt_3 which is an itinerant $5f$ system. Thus, in $U(Pd_{1-x}Pt_x)_3$, the introduction of Platinum with its spatially more extent Pt $5d$ electron wavefunctions causes a small hybridization of the Pt $5d$ electrons with the uranium $5f$ electrons and induces a small itinerant character of the $5f$ electrons [111]. In this picture now, the quasi-free conduction (Pt $5d$) electrons can be described with Bloch-functions which extend over the whole crystal. Due to the hybridization of these electrons with the localized U $5f$ states then an interaction is present which equally influences all U atoms and all quadrupole-quadrupole interactions. In particular, all ordering U atoms on the quasi-cubic sites are influenced identically by the Pt and thus the effective quadrupole-quadrupole interaction is most likely modified. Thus it seems possible that via such a mechanism a small amount of Pt in $U(Pd_{1-x}Pt_x)_3$ leads to a small reduction of the coupling constant at all sites which then causes a strong reduction of the ordering temperatures since all coupling constants are close to the threshold values found in the mean field models. In this scenario the strong suppression of ordering temperatures in $U(Pd_{1-x}Pt_x)_3$ samples with $x = 0.5\%$ is a result from the coupling constant being slightly reduced towards the threshold value. Between $x = 0.5\%$ and $x = 1\%$ the coupling is further reduced and drops below the threshold value resulting in a complete suppression of long range order in the $x = 1\%$ sample. If this scenario including hybridization of the $5f$ and $5d$ electrons really causes the strong reduction of ordering temperatures observed this indicates that the band structure and its hybridization with the localized $5f$ electrons is very important in order to understand the quadrupolar ordered phases in $U(Pd_{1-x}Pt_x)_3$.

Hence, in this second scenario the onset of hybridization leads to a small change of quadrupolar coupling constants. This small change (reduction) drives all coupling constants closer towards the threshold value and thus causes a very strong reduction of ordering temperatures at $x = 0.5\%$ and the suppression of long-range order at $x = 1\%$ as observed. Since we do not need to assume any extraordinary strong or uncommon effects but only effects that have been proposed previously, together with the strong sensitivity of UPd_3 to small changes of the coupling constants we found in our mean field models, we believe that this is the correct scenario to explain the observed properties of $U(Pd_{1-x}Pt_x)_3$. However, we have to mention that the proximity of the coupling constants to the threshold value is a peculiarity of UPd_3 and

$U(Pd_{1-x}Pt_x)_3$ in both scenarios.

In this chapter we have calculated the quadrupolar order parameters of UPd_3 in different mean field models assuming different possible order parameters. We find that the combination of order parameters of the same symmetry gives almost identical results to the models with only one order parameter. In contrast, the combination of order parameters of different symmetry ($\langle O_{zx}\rangle$ and $\langle O_{xy}\rangle$) gives rise to different qudrupolar ordered phases and a complex phase diagram with the specific phase boundaries being strongly dependent on the choice of coupling constants. In all cases we find a threshold value of the coupling constants below which no order is observed. Furthermore, for both order parameters this threshold value is very close to the coupling constants used to obtain reasonably low ordering temperatures. The observed strong reduction of ordering temperatures in $U(Pd_{1-x}Pt_x)_3$ compared to UPd_3 has been discussed in a glass-like picture and in a scenario where the increasing hybridization between platinum $5d$ and uranium $5f$ electrons is the origin of these changes. Although at this point with the available data no definite conclusion on the physical mechanism reducing the ordering temperatures can be drawn we propose the second scenario including increasing hybridization to be correct since no extraordinary (strong) effects need to be proposed.

6 Summary and Outlook

In this thesis two $5f$ electron systems, UPt_2Si_2 and $U(Pd_{1-x}Pt_x)_3$, have been studied in detail using experimental techniques in extreme environments as well as mean field CEF calculations. Previously, both materials were widely treated as model systems for localized uranium $5f$ electrons in the literature.

For UPt_2Si_2 we have shown that absolute numbers of experimental results depend on the sample quality and the part of the single crystal ingot measured while the features appearing in these measurements do not. In particular, we could observe features in magnetization which have been published by Amitsuka *et al.* previously [58]. Thus, we concluded that our signatures of phase transitions are intrinsic features of UPt_2Si_2 from which we constructed the magnetic phase diagram which contains multiple new field induced phases in high magnetic fields. A comparison to other materials which exhibit partially similar physical properties or phase diagrams ruled out the models applied to these other materials to explain our observed properties of UPt_2Si_2. Additionally, in the resistivity and Hall effect we observed distinct signs of Fermi surface effects. Altogether our findings for UPt_2Si_2 are contrary to the expectations for a simple localized f electron system. Hence, we concluded that UPt_2Si_2 has to be treated at least as a partially if not completely itinerant electron system and that our observed phase transitions are accompanied by changes of the Fermi surface. This conclusion is in agreement with very recent electronic band structure calculations of UPt_2Si_2 [61, 66]. Alltogether, it seems very likely that we have observed one of the rare examples of a field driven Lifshitz transition in UPt_2Si_2 at least at the phase transition from phase III to V. Unfortunately, the origin of the other phase transitions is still unresolved due to the limited access with more sophisticated experimental techniques but one may speculate that the Fermi surface plays an important role in these transitions as well.

The localized f electron system UPd_3, which is one of the rare examples of compounds where quadrupolar order is observed, served as a starting point for the alloying series $U(Pd_{1-x}Pt_x)_3$. While the localized picture of UPd_3 has been tested and verified in many publications the strong reduction of ordering temperatures measured in $U(Pd_{1-x}Pt_x)_3$ for doping levels as low as $x = 0.5\%$ and $x = 1\%$ on the non-ordering Pd sites contradicts this local moment picture at first glance. Thus, we set up multiple strictly localized mean field models including magnetic field dependent CEF levels to test if such models could reproduce the experimentally observed phase diagrams and possibly explain the strong reduction of ordering temperatures upon doping. First, in a simple model we could reproduce results from Tokiwa *et al.* proving the reliability of our model [9]. Using a different CEF scheme proposed later by McEwen et al. we found no special features, in particular no stabilization of the ordered phase upon increasing magnetic field, which lead to the conclusion that the original CEF scheme proposed by Buyers *et al.* seems to be more appropriate [128, 129]. Using the CEF scheme from Buyers *et al.* in an extended model allowing for multiple competing order parameters we could qualitatively reproduce parts of the quadrupolar phase diagram of UPd_3 for an appropriate choice of coupling constants although minor differences still exist. The most obvious distinction being a different sequence of order parameters upon reduction of temperature than measured by Walker *et al.* [131].

A detailed analysis of the influence of the coupling constants on our calculated phase diagrams revealed critical coupling constants below which no quadrupolar order develops. This critical coupling strength is close to the values used to obtain reasonable results. Thus, the strong reduction of ordering temperatures found in experiments might either be explained by a glass-like state which is extraordinary sensitive to $5d$ electrons due to Pt doping or by the onset of hybridization between f and conduction electrons, which causes a reduction of the quadrupole-quadrupole interactions, driving the coupling constants to their threshold values. At this point, it is not possible to finally decide which scenario describes $\mathrm{U(Pd_{1-x}Pt_x)_3}$ more adequately although the hybridization scenario seems to be much simpler and hence more appropriate. To distinguish both scenarios it would be desirable to have detailed band structure calculations of $\mathrm{UPd_3}$ or $\mathrm{U(Pd_{1-x}Pt_x)_3}$ in an itinerant scenario and compare these to experimental results. Furthermore, one could try to do resonant x-ray scattering on $\mathrm{U(Pd_{1-x}Pt_x)_3}$ as it was done on $\mathrm{UPd_3}$ in order to decide this open question. Unfortunately both approaches were beyond the reach of this thesis.

In conclusion we have presented measurements and calculations on the two uranium $5f$ electron systems $\mathrm{UPt_2Si_2}$ and $\mathrm{U(Pd_{1-x}Pt_x)_3}$ which mostly have been treated as localized systems in the literature. In contrast, we could show that $\mathrm{UPt_2Si_2}$ has to be treated as an itinerant system and which might be one of the few materials where magnetic field induced Lifshitz transitions can be observed. For $\mathrm{U(Pd_{1-x}Pt_x)_3}$ the case is less clear but our observations can be explained by the pecularity that the quadrupolar coupling constants are very close to a critical value and that the onset of hybridization between localized f and conduction electrons drives these couplings towards their critical values. This scenario seems to be much more likely than other exotic scenarios. Thus, if in this two materials itinerancy is present ($\mathrm{UPt_2Si_2}$) or seems to be important ($\mathrm{U(Pd_{1-x}Pt_x)_3}$), one may speculate that some level of itinerancy might be much more widespread in the uranium compounds than expected or published so far. Moreover, since many arguments and models are similar for most actinide and rare earth compounds this might be true for the whole group of metallic $4f$ and $5f$ systems. Thus, including Fermi surface effects or some degree of itinerancy might help to get a deeper understanding of many of these materials.

A Dipole, Quadrupole and Stevens operators

Since the uranium in UPd$_3$ is in the $5f^2$ configuration we have $j = 4$ with 9 possibilities for m_j. Thus, all operators are 9x9 matrices in this basis. For this configuration the dipolar J operators are

$$J_z = \begin{pmatrix} -4 & 0 & 0 & 0 & 0 & 0 & 0 & 0 & 0 \\ 0 & -3 & 0 & 0 & 0 & 0 & 0 & 0 & 0 \\ 0 & 0 & -2 & 0 & 0 & 0 & 0 & 0 & 0 \\ 0 & 0 & 0 & -1 & 0 & 0 & 0 & 0 & 0 \\ 0 & 0 & 0 & 0 & 0 & 0 & 0 & 0 & 0 \\ 0 & 0 & 0 & 0 & 0 & 1 & 0 & 0 & 0 \\ 0 & 0 & 0 & 0 & 0 & 0 & 2 & 0 & 0 \\ 0 & 0 & 0 & 0 & 0 & 0 & 0 & 3 & 0 \\ 0 & 0 & 0 & 0 & 0 & 0 & 0 & 0 & 4 \end{pmatrix}, \tag{A.1}$$

$$J_+ = \begin{pmatrix} 0 & 0 & 0 & 0 & 0 & 0 & 0 & 0 & 0 \\ 2\sqrt{2} & 0 & 0 & 0 & 0 & 0 & 0 & 0 & 0 \\ 0 & \sqrt{14} & 0 & 0 & 0 & 0 & 0 & 0 & 0 \\ 0 & 0 & 3\sqrt{2} & 0 & 0 & 0 & 0 & 0 & 0 \\ 0 & 0 & 0 & 2\sqrt{5} & 0 & 0 & 0 & 0 & 0 \\ 0 & 0 & 0 & 0 & 2\sqrt{5} & 0 & 0 & 0 & 0 \\ 0 & 0 & 0 & 0 & 0 & 3\sqrt{2} & 0 & 0 & 0 \\ 0 & 0 & 0 & 0 & 0 & 0 & \sqrt{14} & 0 & 0 \\ 0 & 0 & 0 & 0 & 0 & 0 & 0 & 2\sqrt{2} & 0 \end{pmatrix} \text{ and} \tag{A.2}$$

$$J_- = \begin{pmatrix} 0 & 2\sqrt{2} & 0 & 0 & 0 & 0 & 0 & 0 & 0 \\ 0 & 0 & \sqrt{14} & 0 & 0 & 0 & 0 & 0 & 0 \\ 0 & 0 & 0 & 3\sqrt{2} & 0 & 0 & 0 & 0 & 0 \\ 0 & 0 & 0 & 0 & 2\sqrt{5} & 0 & 0 & 0 & 0 \\ 0 & 0 & 0 & 0 & 0 & 2\sqrt{5} & 0 & 0 & 0 \\ 0 & 0 & 0 & 0 & 0 & 0 & 3\sqrt{2} & 0 & 0 \\ 0 & 0 & 0 & 0 & 0 & 0 & 0 & \sqrt{14} & 0 \\ 0 & 0 & 0 & 0 & 0 & 0 & 0 & 0 & 2\sqrt{2} \\ 0 & 0 & 0 & 0 & 0 & 0 & 0 & 0 & 0 \end{pmatrix}. \tag{A.3}$$

From these dipolar operators we can now calculate the quadrupole operators. With

$$J_x = \frac{1}{2}(J_+ + J_-) \qquad J_y = \frac{1}{2i}(J_+ - J_-) \tag{A.4}$$

and

$$X = j(j+1)I = 20I \tag{A.5}$$

where I is the 9 x 9 identity matrix we get

$$\begin{aligned} O_{xy} &= \frac{1}{2}(J_xJ_y + J_yJ_x) && \text{(A.6a)} \\ O_{yz} &= \frac{1}{2}(J_yJ_z + J_zJ_y) && \text{(A.6b)} \\ O_{zx} &= \frac{1}{2}(J_zJ_x + J_xJ_z) && \text{(A.6c)} \\ O_{x^2-y^2} &= J_x^2 - J_y^2 && \text{(A.6d)} \\ O_{3z^2-r^2} &= 3J_z^2 - X && \text{(A.6e)} \end{aligned}$$

We find that $O_{3z^2-r^2}$ has only diagonal elements while the other four matrices have only non-diagonal elements. Thus, $O_{3z^2-r^2}$ shifts the energies of the CEF levels while the other operators mix them.

To calculate the CEF levels in Eqns. 5.1 and 5.2 we need to know the Stevens operators O_p^q which are given by

$$\begin{aligned}
O_2^0 &= 3J_z^2 - X && \text{(A.7a)}\\
O_4^0 &= 35J_z^4 - (30X - 25)J_z^2 + 3X^2 - 6X && \text{(A.7b)}\\
O_4^3 &= \frac{1}{4}\left((J_+^3 + J_-^3)J_z + J_z(J_+^3 + J_-^3)\right) && \text{(A.7c)}\\
O_6^0 &= 231J_z^6 - (315X - 735)J_z^4 + (105X^2 - 525X + 294)J_z^2 - 5X^3 + 40X^2 - 60X && \text{(A.7d)}\\
O_6^3 &= \frac{1}{4}\left((J_+^3 + J_-^3)(11J_z^3 - (3X + 59)J_z) + (11J_z^3 - (3X + 59)J_z)(J_+^3 + J_-^3)\right) && \text{(A.7e)}\\
O_6^6 &= \frac{1}{2}\left(J_+^6 + J_-^6\right) && \text{(A.7f)}
\end{aligned}$$

These Stevens operators are representations of certain potential functions for which the states are Eigenstates of the angular momentum operators and have been first calculated by K. W. H. Stevens [4]. Later these operators equivalents were tabulated for more potential functions [1, 146, 147].

B Program code for mean field calculations

Here now the program code shown in Figs. B.1 to B.9 is discussed which was used to calculate the mixed $\langle O_{zx}\rangle$-$\langle O_{xy}\rangle$ mean field model for UPd$_3$ in section 5.4.2. This code was developed for the 64 bit version of Wolfram Mathematica® 8.0.1.0 and can be extended or reduced easily to calculate the other mean field models studied. In most cases the calculations were put in the `Manipulate` environment to study the influence of different parameters or change the plotting regions quickly. However, in some cases this results in aborted calculations where only `$Aborted` is shown as result. If this happens changing one parameters value, for example from 0 (exact 0) to 0. (zero with machines numerical precision), forces Mathematica to recalculate the output and show correct results.

First of all, the necessary constants and operators have to be defined. The code to do this is shown in Fig. B.1 where the J and O matrices as well as the necessary Stevens Operators are constructed and calculated according to Eqs. A.1-A.7. In the follwing the Boltzmann constant (in units of meV K^{-1}), Landé-factor g_j (Eq. 5.4), and the Bohr Magneton (in units of meV T^{-1}) are defined. Finally, the CEF parameters from Tokiwa *et al.* are defined and calculated in meV [9].

From these operators in a next step the Hamiltonian is constructed as defined in Eqs. 5.1, 5.2 and 5.3 which is shown in Fig. B.2. Additionally, the initial coupling constants are defined which later serve as starting

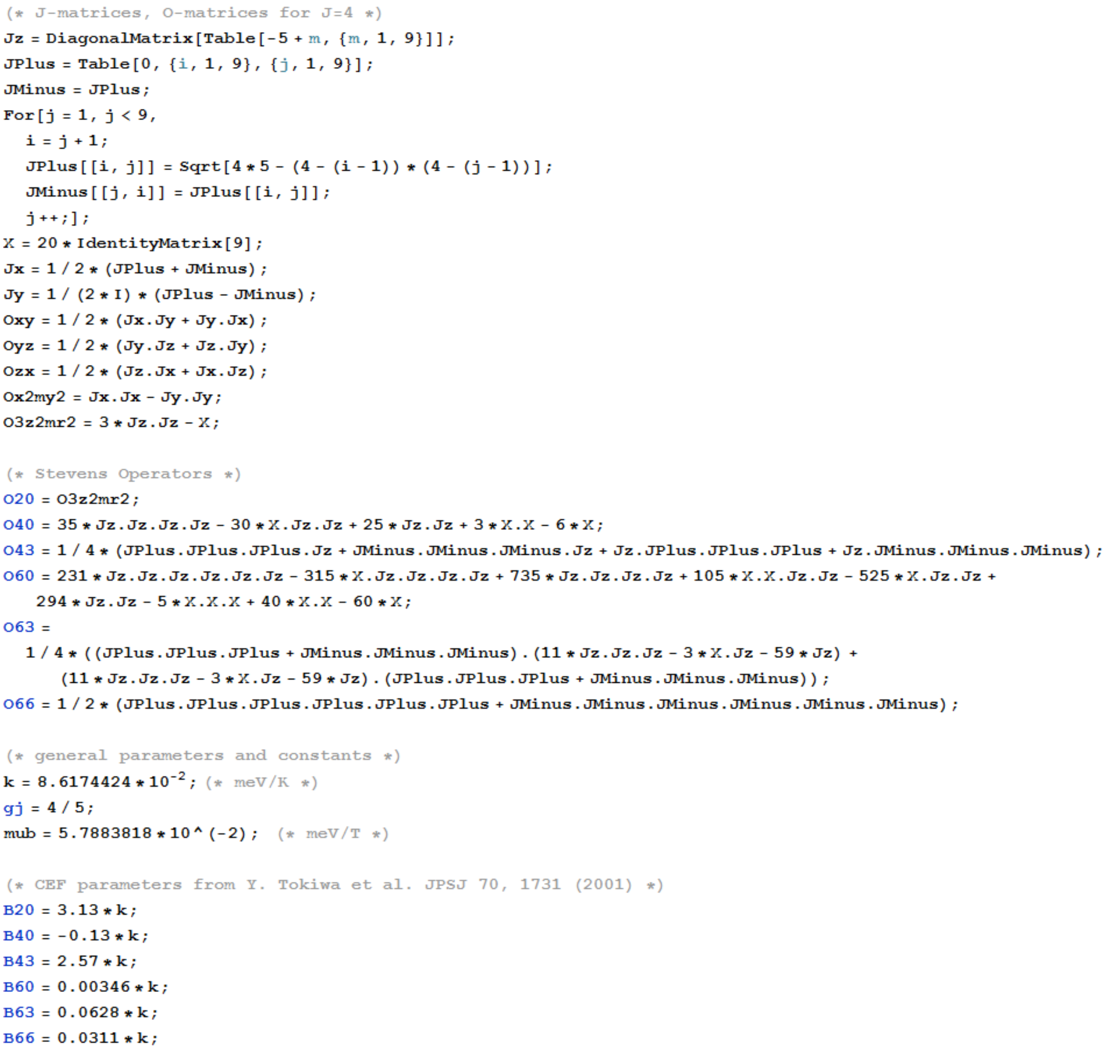

```
(* J-matrices, O-matrices for J=4 *)
Jz = DiagonalMatrix[Table[-5 + m, {m, 1, 9}]];
JPlus = Table[0, {i, 1, 9}, {j, 1, 9}];
JMinus = JPlus;
For[j = 1, j < 9,
  i = j + 1;
  JPlus[[i, j]] = Sqrt[4 * 5 - (4 - (i - 1)) * (4 - (j - 1))];
  JMinus[[j, i]] = JPlus[[i, j]];
  j++;];
X = 20 * IdentityMatrix[9];
Jx = 1 / 2 * (JPlus + JMinus);
Jy = 1 / (2 * I) * (JPlus - JMinus);
Oxy = 1 / 2 * (Jx.Jy + Jy.Jx);
Oyz = 1 / 2 * (Jy.Jz + Jz.Jy);
Ozx = 1 / 2 * (Jz.Jx + Jx.Jz);
Ox2my2 = Jx.Jx - Jy.Jy;
O3z2mr2 = 3 * Jz.Jz - X;

(* Stevens Operators *)
O20 = O3z2mr2;
O40 = 35 * Jz.Jz.Jz.Jz - 30 * X.Jz.Jz + 25 * Jz.Jz + 3 * X.X - 6 * X;
O43 = 1 / 4 * (JPlus.JPlus.JPlus.Jz + JMinus.JMinus.JMinus.Jz + Jz.JPlus.JPlus.JPlus + Jz.JMinus.JMinus.JMinus);
O60 = 231 * Jz.Jz.Jz.Jz.Jz.Jz - 315 * X.Jz.Jz.Jz.Jz + 735 * Jz.Jz.Jz.Jz + 105 * X.X.Jz.Jz - 525 * X.Jz.Jz +
   294 * Jz.Jz - 5 * X.X.X + 40 * X.X - 60 * X;
O63 =
  1 / 4 * ((JPlus.JPlus.JPlus + JMinus.JMinus.JMinus).(11 * Jz.Jz.Jz - 3 * X.Jz - 59 * Jz) +
     (11 * Jz.Jz.Jz - 3 * X.Jz - 59 * Jz).(JPlus.JPlus.JPlus + JMinus.JMinus.JMinus));
O66 = 1 / 2 * (JPlus.JPlus.JPlus.JPlus.JPlus.JPlus + JMinus.JMinus.JMinus.JMinus.JMinus.JMinus);

(* general parameters and constants *)
k = 8.6174424 * 10^-2; (* meV/K *)
gj = 4 / 5;
mub = 5.7883818 * 10 ^ (-2);  (* meV/T *)

(* CEF parameters from Y. Tokiwa et al. JPSJ 70, 1731 (2001) *)
B20 = 3.13 * k;
B40 = -0.13 * k;
B43 = 2.57 * k;
B60 = 0.00346 * k;
B63 = 0.0628 * k;
B66 = 0.0311 * k;
```

Figure B.1: Mathematica code for the calculation of the used operators and constant definitions.

values in the `Manipulate` environments.

Next, with the code shown in Fig. B.3, the Hamiltonian is displayed and for all CEF states the energies are calculated in absolute meV and in K above the ground state. Additionally $J_{z,n}$ and $O^0_{2,n}$ values are shown for the given parameter set and the CEF levels are plotted vs. applied

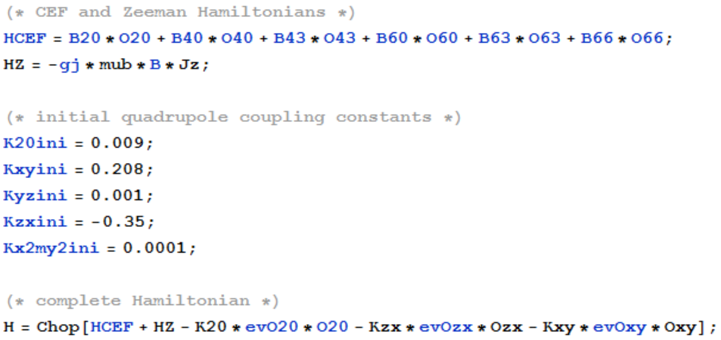

```
(* CEF and Zeeman Hamiltonians *)
HCEF = B20 * O20 + B40 * O40 + B43 * O43 + B60 * O60 + B63 * O63 + B66 * O66;
HZ = -gj * mub * B * Jz;

(* initial quadrupole coupling constants *)
K20ini = 0.009;
Kxyini = 0.208;
Kyzini = 0.001;
Kzxini = -0.35;
Kx2my2ini = 0.0001;

(* complete Hamiltonian *)
H = Chop[HCEF + HZ - K20 * evO20 * O20 - Kzx * evOzx * Ozx - Kxy * evOxy * Oxy];
```

Figure B.2: Mathematica code to calculate Hamiltonian and define initial coupling constants.

magnetic field with all order parameters assumed to be zero.

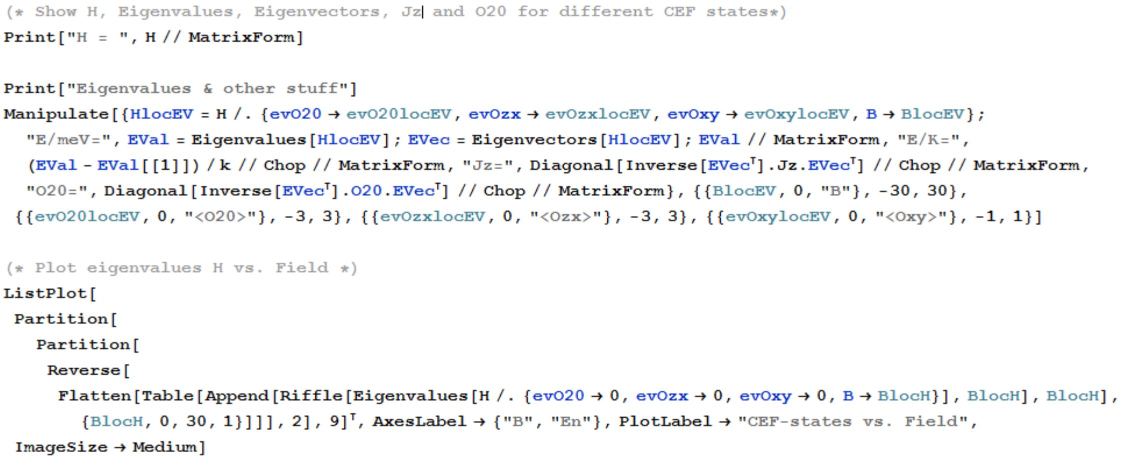

```
(* Show H, Eigenvalues, Eigenvectors, Jz| and O20 for different CEF states*)
Print["H = ", H // MatrixForm]

Print["Eigenvalues & other stuff"]
Manipulate[{HlocEV = H /. {evO20 → evO20locEV, evOzx → evOzxlocEV, evOxy → evOxylocEV, B → BlocEV};
  "E/meV=", EVal = Eigenvalues[HlocEV]; EVec = Eigenvectors[HlocEV]; EVal // MatrixForm, "E/K=",
  (EVal - EVal[[1]]) / k // Chop // MatrixForm, "Jz=", Diagonal[Inverse[EVecᵀ].Jz.EVecᵀ] // Chop // MatrixForm,
  "O20=", Diagonal[Inverse[EVecᵀ].O20.EVecᵀ] // Chop // MatrixForm}, {{BlocEV, 0, "B"}, -30, 30},
 {{evO20locEV, 0, "<O20>"}, -3, 3}, {{evOzxlocEV, 0, "<Ozx>"}, -3, 3}, {{evOxylocEV, 0, "<Oxy>"}, -1, 1}]

(* Plot eigenvalues H vs. Field *)
ListPlot[
 Partition[
   Partition[
    Reverse[
     Flatten[Table[Append[Riffle[Eigenvalues[H /. {evO20 → 0, evOzx → 0, evOxy → 0, B → BlocH}], BlocH], BlocH],
       {BlocH, 0, 30, 1}]]]], 2], 9]ᵀ, AxesLabel → {"B", "En"}, PlotLabel → "CEF-states vs. Field",
 ImageSize → Medium]
```

Figure B.3: Mathematica code to calculate the CEF state Energies in meV and K with their corresponding $J_{z,n}$ and $O^0_{2,n}$ values and plot CEF energies vs. applied magnetic field.

Before calculating the order parameters all necessary functions have to be definded which is shown in Figs. B.4 and B.5. First, the function `Mag` is implemented which gives the solution for the Magnetization M according to Eq. 5.8 when `Mag=0`. Next, the functions to calculate the free energy using Eq. 5.7 are defined. Here, the same function is defined repeatedly using different function names (`FE`, `FEDP0`, …) since otherwise the different `Manipulate` environments interact with each other when the same function is used. By using different function names all calculations work independently as supposed.

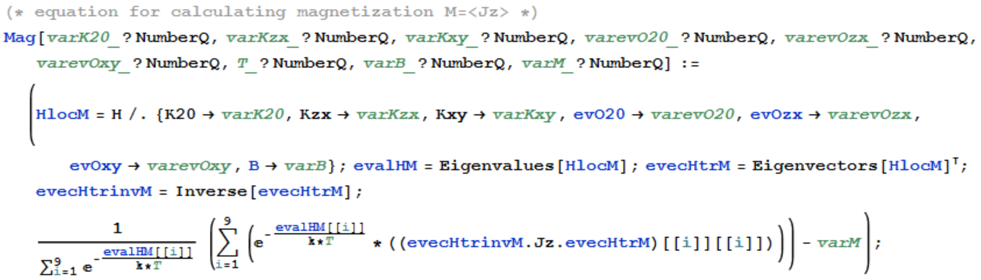

```
(* equation for calculating magnetization M=<Jz> *)
Mag[varK20_?NumberQ, varKzx_?NumberQ, varKxy_?NumberQ, varevO20_?NumberQ, varevOzx_?NumberQ,
  varevOxy_?NumberQ, T_?NumberQ, varB_?NumberQ, varM_?NumberQ] :=
 (HlocM = H /. {K20 → varK20, Kzx → varKzx, Kxy → varKxy, evO20 → varevO20, evOzx → varevOzx,
     evOxy → varevOxy, B → varB}; evalHM = Eigenvalues[HlocM]; evecHtrM = Eigenvectors[HlocM]ᵀ;
  evecHtrinvM = Inverse[evecHtrM];
  1/(Σ_{i=1}^9 e^(-evalHM[[i]]/(k*T))) (Σ_{i=1}^9 (e^(-evalHM[[i]]/(k*T)) * ((evecHtrinvM.Jz.evecHtrM)[[i]][[i]]))) - varM);
```

Figure B.4: Mathematica code to define a function for calculating the magnetization M.

In the function definitions it is important to include `?NumberQ` behind all variables since this way the function is only evaluated if pure numbers are given as an argument. Otherwise Mathematicas internal routines try to simplify the expression before putting in numbers which leads to an error due to the complexity of the calculations.

Since here the numerical minimization of the free energy is a rather complex calculation, different methods for minimization might give different results since not always the global but only a local minimum of the free energy is found. Also, the calculation times differ noticeably. Thus, the code in Fig. B.6 was included and evaluated from time to time to check the stability and calculation times of different minimzation methods.

In general, `"RandomSearch"` seems to always find the correct minimum but is rather slow. If there are two equivalent minima for one given set of parameters always the same solution is found reproducably with `"RandomSearch"` but minimal changes of the parameters might end up in the second minimum. All other methods are much faster but less

```
(* Free energy calculation *)
(* The same equation with different names is needed for every calculation to prevent interference
 between functions when using Manipulate *)
FE[varK20_?NumberQ, varKzx_?NumberQ, varKxy_?NumberQ, varevO20_?NumberQ, varevOzx_?NumberQ,
   varevOxy_?NumberQ, T_?NumberQ, varB_?NumberQ] :=
  -k * T * Log[Total[e^(-Eigenvalues[H/.{K20→varK20,Kzx→varKzx,Kxy→varKxy,evO20→varevO20,evOzx→varevOzx,evOxy→varevOxy,B→varB}]/(k*T))]] +
   Abs[varK20] / 2 * varevO20^2 + Abs[varKzx] / 2 * varevOzx^2 + Abs[varKxy] / 2 * varevOxy^2;
FEDP0[varK20_?NumberQ, varKzx_?NumberQ, varKxy_?NumberQ, varevO20_?NumberQ, varevOzx_?NumberQ,
   varevOxy_?NumberQ, T_?NumberQ, varB_?NumberQ] :=
  -k * T * Log[Total[e^(-Eigenvalues[H/.{K20→varK20,Kzx→varKzx,Kxy→varKxy,evO20→varevO20,evOzx→varevOzx,evOxy→varevOxy,B→varB}]/(k*T))]] +
   Abs[varK20] / 2 * varevO20^2 + Abs[varKzx] / 2 * varevOzx^2 + Abs[varKxy] / 2 * varevOxy^2;
FEDP1[varK20_?NumberQ, varKzx_?NumberQ, varKxy_?NumberQ, varevO20_?NumberQ, varevOzx_?NumberQ,
   varevOxy_?NumberQ, T_?NumberQ, varB_?NumberQ] :=
  -k * T * Log[Total[e^(-Eigenvalues[H/.{K20→varK20,Kzx→varKzx,Kxy→varKxy,evO20→varevO20,evOzx→varevOzx,evOxy→varevOxy,B→varB}]/(k*T))]] +
   Abs[varK20] / 2 * varevO20^2 + Abs[varKzx] / 2 * varevOzx^2 + Abs[varKxy] / 2 * varevOxy^2;
FEDP2[varK20_?NumberQ, varKzx_?NumberQ, varKxy_?NumberQ, varevO20_?NumberQ, varevOzx_?NumberQ,
   varevOxy_?NumberQ, T_?NumberQ, varB_?NumberQ] :=
  -k * T * Log[Total[e^(-Eigenvalues[H/.{K20→varK20,Kzx→varKzx,Kxy→varKxy,evO20→varevO20,evOzx→varevOzx,evOxy→varevOxy,B→varB}]/(k*T))]] +
   Abs[varK20] / 2 * varevO20^2 + Abs[varKzx] / 2 * varevOzx^2 + Abs[varKxy] / 2 * varevOxy^2;
FEDP3[varK20_?NumberQ, varKzx_?NumberQ, varKxy_?NumberQ, varevO20_?NumberQ, varevOzx_?NumberQ,
   varevOxy_?NumberQ, T_?NumberQ, varB_?NumberQ] :=
  -k * T * Log[Total[e^(-Eigenvalues[H/.{K20→varK20,Kzx→varKzx,Kxy→varKxy,evO20→varevO20,evOzx→varevOzx,evOxy→varevOxy,B→varB}]/(k*T))]] +
   Abs[varK20] / 2 * varevO20^2 + Abs[varKzx] / 2 * varevOzx^2 + Abs[varKxy] / 2 * varevOxy^2;
FEDP4[varK20_?NumberQ, varKzx_?NumberQ, varKxy_?NumberQ, varevO20_?NumberQ, varevOzx_?NumberQ,
   varevOxy_?NumberQ, T_?NumberQ, varB_?NumberQ] :=
  -k * T * Log[Total[e^(-Eigenvalues[H/.{K20→varK20,Kzx→varKzx,Kxy→varKxy,evO20→varevO20,evOzx→varevOzx,evOxy→varevOxy,B→varB}]/(k*T))]] +
   Abs[varK20] / 2 * varevO20^2 + Abs[varKzx] / 2 * varevOzx^2 + Abs[varKxy] / 2 * varevOxy^2;
FEOT[varK20_?NumberQ, varKzx_?NumberQ, varKxy_?NumberQ, varevO20_?NumberQ, varevOzx_?NumberQ,
   varevOxy_?NumberQ, T_?NumberQ, varB_?NumberQ] :=
  -k * T * Log[Total[e^(-Eigenvalues[H/.{K20→varK20,Kzx→varKzx,Kxy→varKxy,evO20→varevO20,evOzx→varevOzx,evOxy→varevOxy,B→varB}]/(k*T))]] +
   Abs[varK20] / 2 * varevO20^2 + Abs[varKzx] / 2 * varevOzx^2 + Abs[varKxy] / 2 * varevOxy^2;
FEM[varK20_?NumberQ, varKzx_?NumberQ, varKxy_?NumberQ, varevO20_?NumberQ, varevOzx_?NumberQ,
   varevOxy_?NumberQ, T_?NumberQ, varB_?NumberQ] :=
  -k * T * Log[Total[e^(-Eigenvalues[H/.{K20→varK20,Kzx→varKzx,Kxy→varKxy,evO20→varevO20,evOzx→varevOzx,evOxy→varevOxy,B→varB}]/(k*T))]] +
   Abs[varK20] / 2 * varevO20^2 + Abs[varKzx] / 2 * varevOzx^2 + Abs[varKxy] / 2 * varevOxy^2;
FEPD[varK20_?NumberQ, varKzx_?NumberQ, varKxy_?NumberQ, varevO20_?NumberQ, varevOzx_?NumberQ,
   varevOxy_?NumberQ, T_?NumberQ, varB_?NumberQ] :=
  -k * T * Log[Total[e^(-Eigenvalues[H/.{K20→varK20,Kzx→varKzx,Kxy→varKxy,evO20→varevO20,evOzx→varevOzx,evOxy→varevOxy,B→varB}]/(k*T))]] +
   Abs[varK20] / 2 * varevO20^2 + Abs[varKzx] / 2 * varevOzx^2 + Abs[varKxy] / 2 * varevOxy^2;
```

Figure B.5: Mathematica code to define functions for calculating the free energy of the system.

reliable, so these other methods were used when possible but critical areas of parameter space were calculated using `"RandomSearch"`.

Next, the most important part of the calculations is performed using

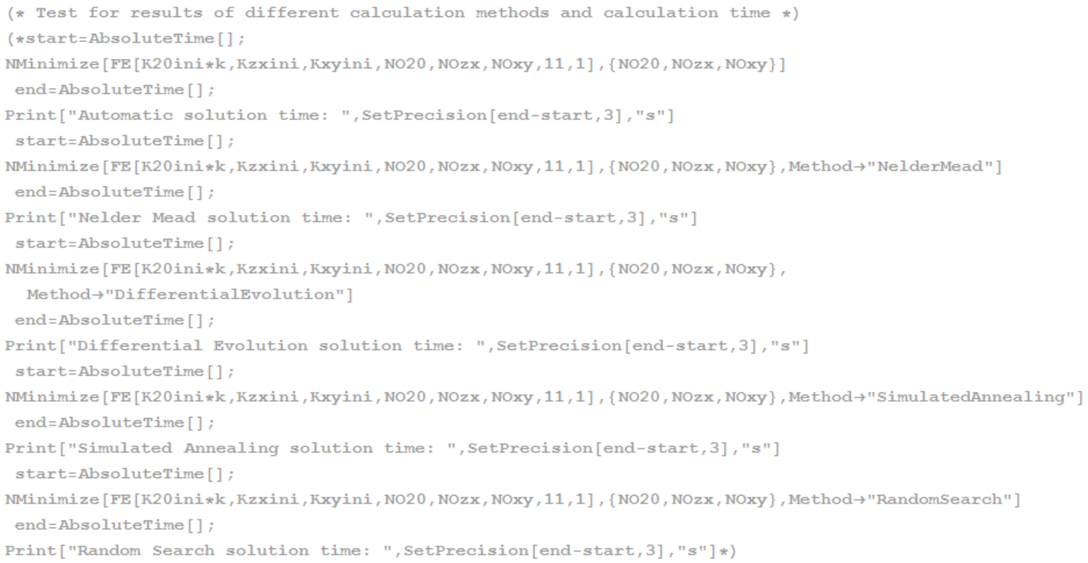

```
(* Test for results of different calculation methods and calculation time *)
(*start=AbsoluteTime[];
NMinimize[FE[K20ini*k,Kzxini,Kxyini,NO20,NOzx,NOxy,11,1],{NO20,NOzx,NOxy}]
 end=AbsoluteTime[];
Print["Automatic solution time: ",SetPrecision[end-start,3],"s"]
 start=AbsoluteTime[];
NMinimize[FE[K20ini*k,Kzxini,Kxyini,NO20,NOzx,NOxy,11,1],{NO20,NOzx,NOxy},Method→"NelderMead"]
 end=AbsoluteTime[];
Print["Nelder Mead solution time: ",SetPrecision[end-start,3],"s"]
 start=AbsoluteTime[];
NMinimize[FE[K20ini*k,Kzxini,Kxyini,NO20,NOzx,NOxy,11,1],{NO20,NOzx,NOxy},
  Method→"DifferentialEvolution"]
 end=AbsoluteTime[];
Print["Differential Evolution solution time: ",SetPrecision[end-start,3],"s"]
 start=AbsoluteTime[];
NMinimize[FE[K20ini*k,Kzxini,Kxyini,NO20,NOzx,NOxy,11,1],{NO20,NOzx,NOxy},Method→"SimulatedAnnealing"]
 end=AbsoluteTime[];
Print["Simulated Annealing solution time: ",SetPrecision[end-start,3],"s"]
 start=AbsoluteTime[];
NMinimize[FE[K20ini*k,Kzxini,Kxyini,NO20,NOzx,NOxy,11,1],{NO20,NOzx,NOxy},Method→"RandomSearch"]
 end=AbsoluteTime[];
Print["Random Search solution time: ",SetPrecision[end-start,3],"s"]*)
```

Figure B.6: Mathematica code to compare solutions and calculation times of different methods for numerical minimzation.

the code shown in Fig. B.7. Here, first, the free energy of the system is minimzed for an initial set of coupling constants, temperature and applied magnetic field giving the free energy of the system and the expectation values $\langle O_2^0 \rangle$, $\langle O_{zx} \rangle$ and $\langle O_{xy} \rangle$ of the qudrupole moments. With these expectation values in a next step the magnetization is calculated. Second, a similar calculation is done to find the expectation values which are then used as a parameter to plot the free energy landscape. Since here we have three expectation values as parameters this plot is split in two with $\langle O_2^0 \rangle$ on the x axis in both cases and $\langle O_{zx} \rangle$ and $\langle O_{xy} \rangle$ on the y axes with the third parameter for each plot coming from the numerical minimization. This way it is possible to check visually if the numerical minimization found the global or only a local minimum. Third, the same plots are generated but this time with user-specified expectation values. These plots are necessary in case one order parameter has two equivalent minima. Then it is possible to manually check the second equivalent minimum which might give a different result for the second order parameter. With the combination of these plots it is possible to determine the correct solution of the calculations in all cases, even if the numerical minimization routine does not find the global minimum reliably or to check if two equivalent minima exist.

```
(* Find global minimum in free energy and calculate M for single point using RandomSearch
 which proved to be most stable and reliable *)
Manipulate[
 {sing = NMinimize[FE[K20sing * k, Kzxsing, Kxysing, NO20sing, NOzxsing, NOxysing, T, B],
     {NO20sing, NOzxsing, NOxysing}, Method → "RandomSearch"]; sing // Chop,
   FindRoot[Mag[K20sing * k, Kzxsing, Kxysing, NO20sing /. sing[[2]], NOzxsing /. sing[[2]],
       NOxysing /. sing[[2]], T, B, M] == 0, {M, 1}] // Chop} // MatrixForm, {{K20sing, K20ini, "K20"}, 0, 0.02},
 {{Kzxsing, Kzxini, "Kzx"}, -0.5, 0}, {{Kxysing, Kxyini, "Kxy"}, 0, 0.5}, {{T, 1}, 0.001, 20}, {{B, 0}, -30, 30}]

(* Make density plots to check visually for correct minima in free energy *)
Manipulate[
 {DPsol = NMinimize[FEDP0[K20DP1 * k, KzxDP1, KxyDP1, NO20DP1, NOzxDP1, NOxyDP1, TDP1, BDP1],
    {NO20DP1, NOzxDP1, NOxyDP1}, Method → "RandomSearch"],
  DensityPlot[FEDP1[K20DP1 * k, KzxDP1, KxyDP1, O20, Ozx, NOxyDP1 /. DPsol[[2]], TDP1, BDP1],
   {O20, O20min, O20max}, {Ozx, -Ozxrange, Ozxrange}, AxesLabel → {"O20", "Ozx"},
   ColorFunction → "TemperatureMap", MeshFunctions → {#3 &}, Mesh → 20, ImageSize → Medium,
   PlotLabel → "Energy vs. <O20> (x) and <Ozx> (y)"],
  DensityPlot[FEDP2[K20DP1 * k, KzxDP1, KxyDP1, O20, NOzxDP1 /. DPsol[[2]], Oxy, TDP1, BDP1],
   {O20, O20min, O20max}, {Oxy, -Oxyrange, Oxyrange}, AxesLabel → {"O20", "Oxy"},
   ColorFunction → "TemperatureMap", MeshFunctions → {#3 &}, Mesh → 20, ImageSize → Medium,
   PlotLabel → "Energy vs. <O20> (x) and <Oxy> (y)"]}, {{K20DP1, K20ini, "K20"}, 0, 0.02},
 {{KzxDP1, Kzxini, "Kzx"}, -0.5, 0}, {{KxyDP1, Kxyini, "Kxy"}, 0, 0.5}, {{TDP1, 1, "T"}, 0.001, 20},
 {{BDP1, 0, "B"}, -30, 30}, {{O20min, -20}, -50, 0}, {{O20max, -6}, 0, 50}, {{Ozxrange, 3}, 0, 5},
 {{Oxyrange, 1.5}, 0, 5}]

(* Same with expectation values manually in case NMinimize does give only one of 2 symmetric minima *)
Manipulate[
 {DensityPlot[FEDP3[K20DP2 * k, KzxDP2, KxyDP2, O20, Ozx, OxyDP2, TDP2, BDP2], {O20, O20min, O20max},
   {Ozx, -Ozxrange, Ozxrange}, AxesLabel → {"O20", "Ozx"}, ColorFunction → "TemperatureMap",
   MeshFunctions → {#3 &}, Mesh → 20, ImageSize → Medium, PlotLabel → "Energy vs. <O20> (x) and <Ozx> (y)"],
  DensityPlot[FEDP4[K20DP2 * k, KzxDP2, KxyDP2, O20, OzxDP2, Oxy, TDP2, BDP2], {O20, O20min, O20max},
   {Oxy, -Oxyrange, Oxyrange}, AxesLabel → {"O20", "Oxy"}, ColorFunction → "TemperatureMap",
   MeshFunctions → {#3 &}, Mesh → 20, ImageSize → Medium, PlotLabel → "Energy vs. <O20> (x) and <Oxy> (y)"]},
 {{K20DP2, K20ini, "K20"}, 0, 0.02}, {{KzxDP2, Kzxini, "Kzx"}, -0.5, 0}, {{KxyDP2, Kxyini, "Kxy"}, 0, 0.5},
 {{TDP2, 1, "T"}, 0.001, 20}, {{BDP2, 0, "B"}, -30, 30}, {{OxyDP2, 0, "Oxy in O20-Ozx Plot"}, -5, 5},
 {{OzxDP2, 0, "Ozx in O20-Oxy Plot"}, -5, 5}, {{O20min, -20}, -50, 0}, {{O20max, -6}, 0, 50},
 {{Ozxrange, 3}, 0, 5}, {{Oxyrange, 1.5}, 0, 5}]
```

Figure B.7: Mathematica code to calculate the expectation values of the quadrupole operators for a given set of parameters and check the validity of the found solutions.

When the correct solutions are found, with the code in Fig. B.8, plots for the order parameters vs. temperature and magnetization vs.

applied magnetic field are calculated with B or T as parameter. Here, assumptions are included in the numerical minimization in order to find the previously determined correct minima for $\langle O_{zx} \rangle$ and exclude one of two equivalent minima for $\langle O_{xy} \rangle$, so that the faster automatically determined minimization routine can be used.

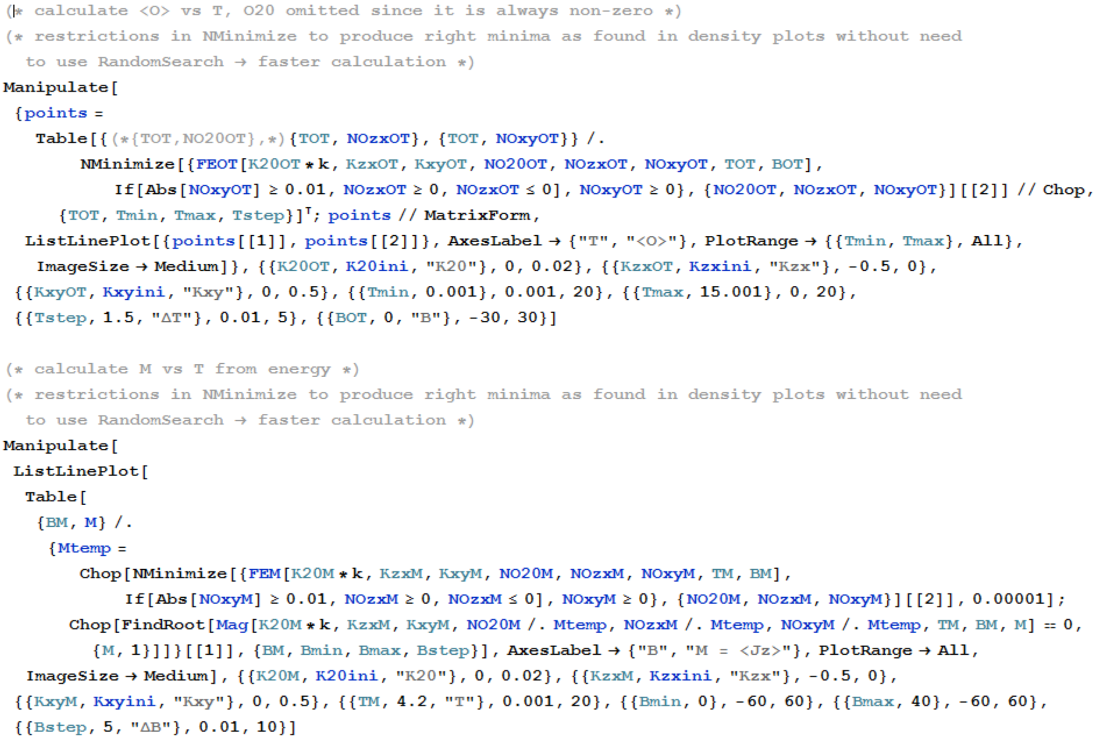

```
(* calculate <O> vs T, O20 omitted since it is always non-zero *)
(* restrictions in NMinimize to produce right minima as found in density plots without need
  to use RandomSearch → faster calculation *)
Manipulate[
 {points =
   Table[{(*{TOT,NO20OT},*){TOT, NOzxOT}, {TOT, NOxyOT}} /.
       NMinimize[{FEOT[K20OT * k, KzxOT, KxyOT, NO20OT, NOzxOT, NOxyOT, TOT, BOT],
          If[Abs[NOxyOT] ≥ 0.01, NOzxOT ≥ 0, NOzxOT ≤ 0], NOxyOT ≥ 0}, {NO20OT, NOzxOT, NOxyOT}][[2]] // Chop,
     {TOT, Tmin, Tmax, Tstep}]ᵀ; points // MatrixForm,
  ListLinePlot[{points[[1]], points[[2]]}, AxesLabel → {"T", "<O>"}, PlotRange → {{Tmin, Tmax}, All},
   ImageSize → Medium]}, {{K20OT, K20ini, "K20"}, 0, 0.02}, {{KzxOT, Kzxini, "Kzx"}, -0.5, 0},
 {{KxyOT, Kxyini, "Kxy"}, 0, 0.5}, {{Tmin, 0.001}, 0.001, 20}, {{Tmax, 15.001}, 0, 20},
 {{Tstep, 1.5, "ΔT"}, 0.01, 5}, {{BOT, 0, "B"}, -30, 30}]

(* calculate M vs T from energy *)
(* restrictions in NMinimize to produce right minima as found in density plots without need
  to use RandomSearch → faster calculation *)
Manipulate[
 ListLinePlot[
  Table[
   {BM, M} /.
    {Mtemp =
       Chop[NMinimize[{FEM[K20M * k, KzxM, KxyM, NO20M, NOzxM, NOxyM, TM, BM],
           If[Abs[NOxyM] ≥ 0.01, NOzxM ≥ 0, NOzxM ≤ 0], NOxyM ≥ 0}, {NO20M, NOzxM, NOxyM}][[2]], 0.00001];
      Chop[FindRoot[Mag[K20M * k, KzxM, KxyM, NO20M /. Mtemp, NOzxM /. Mtemp, NOxyM /. Mtemp, TM, BM, M] == 0,
        {M, 1}]]}[[1]], {BM, Bmin, Bmax, Bstep}], AxesLabel → {"B", "M = <Jz>"}, PlotRange → All,
  ImageSize → Medium], {{K20M, K20ini, "K20"}, 0, 0.02}, {{KzxM, Kzxini, "Kzx"}, -0.5, 0},
 {{KxyM, Kxyini, "Kxy"}, 0, 0.5}, {{TM, 4.2, "T"}, 0.001, 20}, {{Bmin, 0}, -60, 60}, {{Bmax, 40}, -60, 60},
 {{Bstep, 5, "ΔB"}, 0.01, 10}]
```

Figure B.8: Mathematica code to generate plots of order parameters vs. temperature and magnetization vs. applied magnetic field.

Finally, the code in Fig. B.9 is used to calculate a complete set of ordering parameters vs. temperature and magnetic field. Again, assumptions are included in the numerical minimization so that the faster routines can be used. Since this calculations are still very time consuming a small time measurement routine is included to help estimating the duration of more detailed calculations.

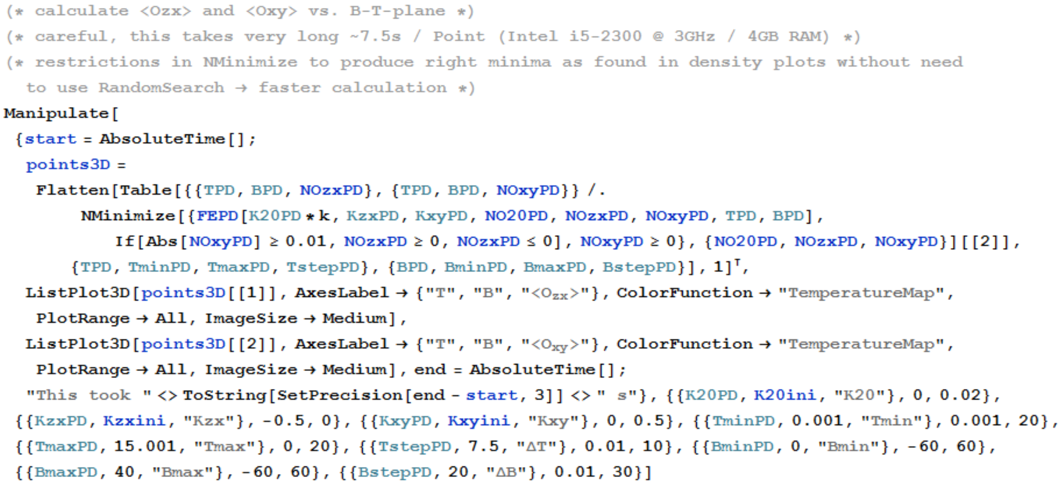

```
(* calculate <Ozx> and <Oxy> vs. B-T-plane *)
(* careful, this takes very long ~7.5s / Point (Intel i5-2300 @ 3GHz / 4GB RAM) *)
(* restrictions in NMinimize to produce right minima as found in density plots without need
  to use RandomSearch → faster calculation *)
Manipulate[
 {start = AbsoluteTime[];
  points3D =
   Flatten[Table[{{TPD, BPD, NOzxPD}, {TPD, BPD, NOxyPD}} /.
        NMinimize[{FEPD[K20PD * k, KzxPD, KxyPD, NO20PD, NOzxPD, NOxyPD, TPD, BPD],
            If[Abs[NOxyPD] ≥ 0.01, NOzxPD ≥ 0, NOzxPD ≤ 0], NOxyPD ≥ 0}, {NO20PD, NOzxPD, NOxyPD}][[2]],
      {TPD, TminPD, TmaxPD, TstepPD}, {BPD, BminPD, BmaxPD, BstepPD}], 1]ᵀ,
  ListPlot3D[points3D[[1]], AxesLabel → {"T", "B", "<Ozx>"}, ColorFunction → "TemperatureMap",
   PlotRange → All, ImageSize → Medium],
  ListPlot3D[points3D[[2]], AxesLabel → {"T", "B", "<Oxy>"}, ColorFunction → "TemperatureMap",
   PlotRange → All, ImageSize → Medium], end = AbsoluteTime[];
  "This took " <> ToString[SetPrecision[end - start, 3]] <> " s"}, {{K20PD, K20ini, "K20"}, 0, 0.02},
 {{KzxPD, Kzxini, "Kzx"}, -0.5, 0}, {{KxyPD, Kxyini, "Kxy"}, 0, 0.5}, {{TminPD, 0.001, "Tmin"}, 0.001, 20},
 {{TmaxPD, 15.001, "Tmax"}, 0, 20}, {{TstepPD, 7.5, "ΔT"}, 0.01, 10}, {{BminPD, 0, "Bmin"}, -60, 60},
 {{BmaxPD, 40, "Bmax"}, -60, 60}, {{BstepPD, 20, "ΔB"}, 0.01, 30}]
```

Figure B.9: Mathematica code to generate 3D plots of the order parameters vs. temperature and applied magnetic field.

List of Figures

Bibliography

[1] M. T. Hutchings, in *Solid State Physics*, edited by F. Seitz and D. Turnbull Vol. 16, p. 227, Academic Press, New York, 1964. 15, 17, 18, 19, 20, 143

[2] J. Jensen and A. R. Mackintosh, *Rare Earth Magnetism: Structure and Excitations* (Clarendon Press, Oxford, 1991). 15, 16, 17, 18, 19, 21, 23, 155

[3] K. H. J. Buschow and F. R. de Boer, *Physics of Magnetism and Magnetic Materials* (Kluwer Academic Publishers, 2003). 15, 18, 20, 22, 23, 155

[4] K. W. H. Stevens, Proc. Phys. Soc. A **65**, 209 (1952). 15, 19, 143

[5] P. A. Lindgard and O. Danielsen, J. Phys. C: Solid State Phys. **7**, 1523 (1974).

[6] K. Takegahara, J. Phys. Soc. Jpn. **69**, 1572 (2000).

[7] H. Kusunose, J. Phys. Soc. Jpn. **77**, 064710 (2008). 15, 19, 21

[8] B. Bleaney and K. W. H. Stevens, Rep. Prog. Phys. **16**, 108 (1953). 19

[9] Y. Tokiwa, K. Sugiyama, T. Takeuchi, M. Nakashima, R. Settai, Y. Inada, Y. Haga, E. Yamamoto, K. Kindo, H. Harima and Y. Ōnuki, J. Phys. Soc. Jpn. **70**, 1731 (2001). 22, 86, 87, 88, 89,

91, 95, 96, 97, 98, 99, 101, 102, 103, 104, 105, 106, 107, 109, 112, 127, 128, 138, 145, 158, 159, 160, 161

[10] I. M. Lifshitz, Sov. Phys. JETP **11**, 1130 (1960). 27, 28, 32, 34, 155

[11] Y. M. Blanter, M. I. Kaganov, A. V. Pantsulaya and A. A. Varlamov, Phys. Rep. **245**, 159 (1994). 28, 32, 34

[12] P. Ehrenfest, Commun. Kamerlingh-Onnes Lab. Un. Leiden Suppl. **75 B**, 813 (1933). 27, 34

[13] A. V. Andrianov and O. A. Savelieva, Europhys. Lett. **82**, 47012 (2008). 27, 32, 37

[14] Y. Okamoto, A. Nishio and Z. Hiroi, Phys. Rev. B **81**, 121102 (2010). 36, 155

[15] N. Kozlova, J. Hagel, M. Doerr, J. Wosnitza, D. Eckert, K.-H. Müller, L. Schultz, I. Opahle, S. Elgazzar, M. Richter, G. Goll, H. v. Löhneysen, G. Zwicknagl, T. Yoshino and T. Takabatake, Phys. Rev. Lett. **95**, 086403 (2005). 37

[16] R. Daou, C. Bergemann and S. R. Julian, Phys. Rev. Lett. **96**, 026401 (2006). 35, 36, 155

[17] P. M. C. Rourke, A. McCollam, G. Lapertot, G. Knebel, J. Flouquet and S. R. Julian, Phys. Rev. Lett. **101**, 237205 (2008). 37

[18] E. A. Yelland, J. M. Barraclough, W. Wang, K. V. Kamenev and A. D. Huxley, Nat. Phys. **7**, 890 (2011). 36, 37, 155

[19] T. Plackowski, D. Kaczorowski and J. Sznajd, Phys. Rev. B **83**, 174443 (2011). 37, 39

[20] A. Hackl and M. Vojta, Phys. Rev. Lett. **106**, 137002 (2011). 27, 32, 37

[21] L. Van Hove, Phys. Rev. **89**, 1189 (1953). 29, 31

[22] W. Potzel, M. Steiner, H. Karzel, W. Schiessl, M. Köfferlein, G. M. Kalvius and P. Blaha, Phys. Rev. Lett. **74**, 1139 (1995). 32

[23] A. N. Velikodnyĭ, N. V. Zavaritskii, T. A. Ignat'eva and A. A. Yurgens, Zh. Eksp. Teor. Fiz. **43**, 597 (1986), [JETP Lett. **43**, 773 (1986)]. 34

[24] V. S. Egorov, M. Y. Lavrenyuk, N. Y. Minina and A. M. Savin, Zh. Eksp. Teor. Fiz. **40**, 25 (1984), [JETP Lett. **40**, 750 (1984)].

[25] Y. P. Gaĭdukov, N. P. Danilova and N. E. V., Zh. Eksp. Teor. Fiz. **39**, 522 (1984), [JETP Lett. **39**, 637 (1984)].

[26] S. V. Varyukhin and V. S. Egorov, Zh. Eksp. Teor. Fiz. **39**, 510 (1984).

[27] S. V. Varyukhin, V. S. Egorov, M. N. Khlopkin, V. P. Antropov, V. G. Vaks, M. I. Katsnel'son, V. Koreshkov, A. I. Likhtenshtein and A. V. Trefilov, Zh. Eksp. Teor. Fiz. **94**, 254 (1988), [Sov. Phys. JETP **67**, 2318 (1988)]. 34

[28] T. T. M. Palstra, A. A. Menovsky, J. v. d. Berg, A. J. Dirkmaat, P. H. Kes, G. J. Nieuwenhuys and J. A. Mydosh, Phys. Rev. Lett. **55**, 2727 (1985). 39

[29] H. Amitsuka, M. Sato, N. Metoki, M. Yokoyama, K. Kuwahara, T. Sakakibara, H. Morimoto, S. Kawarazaki, Y. Miyako and J. A. Mydosh, Phys. Rev. Lett. **83**, 5114 (1999). 39

[30] R. Okazaki, T. Shibauchi, H. J. Shi, Y. Haga, T. D. Matsuda, E. Yamamoto, Y. Onuki, H. Ikeda and Y. Matsuda, Science **331**, 439 (2011). 39

[31] S. Fujimoto, Phys. Rev. Lett. **106**, 196407 (2011). 39

[32] N. Harrison, M. Jaime and J. A. Mydosh, Phys. Rev. Lett. **90**, 096402 (2003). 39, 78

[33] A. Suslov, J. B. Ketterson, D. G. Hinks, D. F. Agterberg and B. K. Sarma, Phys. Rev. B **68**, 020406 (2003).

[34] K. H. Kim, N. Harrison, M. Jaime, G. S. Boebinger and J. A. Mydosh, Phys. Rev. Lett. **91**, 256401 (2003). 39, 78

[35] L. M. Sandratskii and J. Kübler, Phys. Rev. B **50**, 9258 (1994). 39

[36] L. Rebelsky, M. W. McElfresh, M. S. Torikachvili, B. M. Powell and M. B. Maple, **69**, 4810 (1991). 39

[37] T. D. Matsuda, N. Metoki, Y. Haga, S. Ikeda, T. Okubo, K. Sugiyama, N. Nakamura, K. Kindo, K. Kaneko, A. Nakamura, E. Yamamoto and Y. Ōnuki, J. Phys. Soc. Jpn. **72**, 122 (2003).

[38] T. D. Matsuda, S. Ikeda, E. Yamamoto, Y. Haga, H. Shishido, H. Yamagami, R. Settai and Y. Ōnuki, J. Phys. Soc. Jpn. **79**, 114712 (2010).

[39] J. Morkowski, G. Chelkowska, M. Werwiński, A. Szajek, R. Troć and C. Neise, J. Alloys Compd. **509**, 6994 (2011).

[40] P. Svoboda, P. Javorský, F. Honda, V. Sechovský and A. Menovsky, Cent. Eur. J. Phys. **2**, 397 (2004), 10.2478/BF02475639.

[41] T. Endstra, G. J. Nieuwenhuys and J. A. Mydosh, Phys. Rev. B **48**, 9595 (1993). 39

[42] S. Süllow, G. J. Nieuwenhuys, A. A. Menovsky, J. A. Mydosh, S. A. M. Mentink, T. E. Mason and W. J. L. Buyers, Phys. Rev. Lett. **78**, 354 (1997). 39

[43] S. Süllow, S. A. M. Mentink, T. E. Mason, R. Feyerherm, G. J. Nieuwenhuys, A. A. Menovsky and J. A. Mydosh, Phys. Rev. B **61**, 8878 (2000).

[44] S. Süllow, I. Maksimov, A. Otop, F. J. Litterst, A. Perucchi, L. Degiorgi and J. A. Mydosh, Phys. Rev. Lett. **93**, 266602 (2004).

[45] S. Süllow, A. Otop, A. Loose, J. Klenke, O. Prokhnenko, R. Feyerherm, R. W. A. Hendrikx, J. A. Mydosh and H. Amitsuka, J. Phys. Soc. Jpn. **77**, 024708 (2008). 39, 40, 41, 42, 43, 44, 45, 46, 51, 53, 59, 60, 63, 66, 155, 156

[46] S. Ikeda, M. Nakashima, T. D. Matsuda, N. Tateiwa, E. Yamamoto, A. Nakamura, Y. Haga, M. Hedo, Y. Uwatoko and Y. Ōnuki, J. Phys. Soc. Jpn. **75**, 125003 (2006).

[47] M. Bleckmann, A. Otop, S. Süllow, R. Feyerherm, J. Klenke, A. Loose, R. W. A. Hendrikx, J. A. Mydosh and H. Amitsuka, J. Magn. Magn. Mater. **322**, 2447 (2010). 39, 46, 57

[48] G. Zwicknagl, A. Yaresko and P. Fulde, Physica B **312-313**, 304 (2002). 39, 80

[49] M. Dressel, N. Kasper, K. Petukhov, B. Gorshunov, G. Grüner, M. Huth and H. Adrian, Phys. Rev. Lett. **88**, 186404 (2002).

[50] G. Zwicknagl and P. Fulde, J. Phys. Condens. Matter **15**, S1911 (2003). 80

[51] S.-I. Fujimori, Y. Saitoh, T. Okane, A. Fujimori, H. Yamagami, Y. Haga, E. Yamamoto and Y. Onuki, Nat. Phys. **3**, 618 (2007).

[52] J.-P. Rueff, S. Raymond, A. Yaresko, D. Braithwaite, P. Leininger, G. Vankó, A. Huxley, J. Rebizant and N. Sato, Phys. Rev. B **76**, 085113 (2007).

[53] G. J. McMullan, P. M. C. Rourke, M. R. Norman, A. D. Huxley, N. Doiron-Leyraud, J. Flouquet, G. G. Lonzarich, A. McCollam and S. R. Julian, New J. Phys. **10**, 053029 (2008). 39

[54] R. Caspary, P. Hellmann, M. Keller, G. Sparn, C. Wassilew, R. Köhler, C. Geibel, C. Schank, F. Steglich and N. E. Phillips, Phys. Rev. Lett. **71**, 2146 (1993). 39, 80

[55] R. Feyerherm, A. Amato, F. N. Gygax, A. Schenck, C. Geibel, F. Steglich, N. Sato and T. Komatsubara, Phys. Rev. Lett. **73**, 1849 (1994). 39, 80

[56] G. J. Nieuwenhuys, Phys. Rev. B **35**, 5260 (1987). 39, 41, 43

[57] R. A. Steeman, E. Frikkee, S. A. M. Mentink, A. A. Menovsky, G. J. Nieuwenhuys and J. A. Mydosh, J. Phys. Condens. Matter **2**, 4059 (1990). 41, 51, 67

[58] H. Amitsuka, T. Sakakibara, K. Sugiyama, T. Ikeda, Y. Miyako, M. Date and A. Yamagishi, Physica B **177**, 173 (1992). 39, 41, 42, 47, 137, 156

[59] D. Schulze Grachtrup, M. Bleckmann, S. Süllow, B. Willenberg, H. Rakoto, Y. Skourski and J. Mydosh, J. Low Temp. Phys. **159**, 147 (2010). 40, 43, 79

[60] D. Schulze Grachtrup, M. Bleckmann, B. Willenberg, S. Süllow, M. Bartkowiak, Y. Skourski, H. Rakoto, I. Sheikin and J. A. Mydosh, Phys. Rev. B **85**, 054410 (2012). 40, 47, 48, 49, 50, 51, 52, 53, 54, 55, 60, 66, 68, 81, 156, 157

[61] Z. Çakir, Elektronische Eigenschaften von $5f$-Systemen: Die Schwer-Fermion-Verbindung UPt_2Si_2, Master's thesis, TU Braunschweig, 2012. 40, 45, 80, 82, 137

[62] K. Hiebl and P. Rogl, J. Nucl. Mater. **144**, 193 (1987). 40

[63] H. Ptasiewicz-Bąk, J. Leciejewicz and A. Zygmunt, Solid State Commun. **55**, 601 (1985). 41

[64] R. A. Steeman, E. Frikkee, C. van Dijk, G. J. Nieuwenhuys and A. A. Menovksy, J. Magn. Magn. Mater. **76-77**, 435 (1988). 41

[65] M. Bleckmann, *Itinerant to localized views on f-electron systems: A multiprobe study*, PhD thesis, TU Braunschweig, 2009. 43, 48, 49, 50, 92, 93, 95

[66] S. Elgazzar, J. Rusz, P. M. Oppeneer and J. A. Mydosh, Phys. Rev. B **86**, 075104 (2012). 45, 81, 82, 137

[67] A. A. Menovsky, A. C. Moleman, C. E. Snel, T. J. Gortenmulder, H. J. Tan and T. T. M. Palstra, J. Cryst. Growth **79**, 316 (1986). 46

[68] S. Zherlitsyn, A. D. Bianchi, T. Herrmannsdoerfer, F. Pobell, Y. Skourski, A. Sytcheva, S. Zvyagin and J. Wosnitza, IEEE Trans. Appl. Supercond. **16**, 1660 (2006). 46

[69] N. Johannsen, S. Süllow, A. V. Sologubenko, T. Lorenz and J. A. Mydosh, Phys. Rev. B **78**, 121103 (2008). 51

[70] N. H. Anderson, Electrical resistivity investigations on metallic rare-earths, in *Crystalline Electric Field and Structural Effects in f-electron Systems*, edited by J. E. Crow, R. P. Guertin and T. W. Mihalisin, chap. 6, p. 373, Springer Verlag GmbH, 1980. 59, 61

[71] N. Nagaosa, J. Sinova, S. Onoda, A. H. MacDonald and N. P. Ong, Rev. Mod. Phys. **82**, 1539 (2010). 63

[72] V. A. Schmidt and S. A. Friedberg, Phys. Rev. B **1**, 2250 (1970). 67

[73] E. Stryjewski and N. Giordano, Adv. Phys. **26**, 487 (1977). 67

[74] K. Katsumata, H. A. Katori, S. M. Shapiro and G. Shirane, Phys. Rev. B **55**, 11466 (1997).

[75] J. Kincaid and E. Cohen, Phys. Rep. **22**, 57 (1975).

[76] W. Selke, Z. Phys. B: Condens. Matter **101**, 145 (1996).

[77] M. Santos and W. Figueiredo, Phys. Rev. B **58**, 9321 (1998).

[78] M. Žukovič and T. Idogaki, Phys. Rev. B **61**, 50 (2000). 67

[79] S. Süllow, A. Otop, J. Klenke, R. Feyerherm, R. W. A. Hendrikx and J. A. Mydosh, J. Appl. Phys. **99**, 08F704 (2006). 67

[80] G. Wei, J. Liu, H. Miao and A. Du, Phys. Rev. B **76**, 054402 (2007). 67, 79

[81] S. Süllow, B. Janossy, G. L. E. van Vliet, G. J. Nieuwenhuys, A. A. Menovsky and J. A. Mydosh, J. Phys. Condens. Matter **8**, 729 (1996). 68, 78

[82] K. Oda, T. Kumada, K. Sugiyama, N. Sato, T. Komatubara and M. Date, J. Phys. Soc. Jpn. **63**, 3115 (1994).

[83] A. de Visser, H. Nakotte, L. Tai, A. Menovsky, S. Mentink, G. Nieuwenhuys and J. Mydosh, Physica B **179**, 84 (1992). 68, 78

[84] S. Süllow, B. Becker, A. de Visser, M. Mihalik, G. J. Nieuwenhuys, A. A. Menovsky and J. A. Mydosh, J. Phys. Condens. Matter **9**, 913 (1997). 71

[85] N. Tateiwa, N. Sato and T. Komatsubara, Phys. Rev. B **58**, 11131 (1998). 71

[86] M. Jaime, K. H. Kim, G. Jorge, S. McCall and J. A. Mydosh, Phys. Rev. Lett. **89**, 287201 (2002). 78

[87] P. Haen, J. Flouquet, F. Lapierre, P. Lejay and G. Remenyi, J. Low Temp. Phys. **67**, 391 (1987).

[88] C. Paulsen, A. Lacerda, L. Puech, P. Haen, P. Lejay, J. L. Tholence, J. Flouquet and A. Visser, J. Low Temp. Phys. **81**, 317 (1990).

[89] K. Hasselbach, L. Taillefer and J. Flouquet, Phys. Rev. Lett. **63**, 93 (1989).

[90] S. Adenwalla, S. W. Lin, Q. Z. Ran, Z. Zhao, J. B. Ketterson, J. A. Sauls, L. Taillefer, D. G. Hinks, M. Levy and B. K. Sarma, Phys. Rev. Lett. **65**, 2298 (1990). 78

[91] M. de Azevedo, C. Binek, J. Kushauer, W. Kleemann and D. Bertrand, J. Magn. Magn. Mater. **140-144, Part 3**, 1557 (1995). 78

[92] G. Zwicknagl, A. N. Yaresko and P. Fulde, Phys. Rev. B **65**, 081103 (2002). 80

[93] G. Zwicknagl, private communication, 2012. 82

[94] B. Lüthi, M. E. Mullen, K. Andres, E. Bucher and J. P. Maita, Phys. Rev. B **8**, 2639 (1973). 83

[95] R. Aléonard and P. Morin, Phys. Rev. B **19**, 3868 (1979).

[96] P. Morin, J. Rouchy and D. Schmitt, Phys. Rev. B **17**, 3684 (1978).

[97] M. Kosaka, H. Onodera, K. Ohoyama, M. Ohashi, Y. Yamaguchi, S. Nakamura, T. Goto, H. Kobayashi and S. Ikeda, Phys. Rev. B **58**, 6339 (1998).

[98] T. Matsumura, S. Nakamura, T. Goto, H. Amitsuka, K. Matsuhira, T. Sakakibara and T. Suzuki, J. Phys. Soc. Jpn. **67**, 612 (1998).

[99] P. Morin, D. Schmitt and E. du Tremolet de Lacheisserie, J. Magn. Magn. Mater. **30**, 257 (1982).

[100] J. Effantin, J. Rossat-Mignod, P. Burlet, H. Bartholin, S. Kunii and T. Kasuya, J. Magn. Magn. Mater. **47 - 48**, 145 (1985). 83

[101] S. Sako, H. Onodera, H. Yamauchi, K. Indoh, A. Tobo, K. Ohoyama and Y. Yamaguchi, J. Phys. Soc. Jpn. **69**, 1872 (2000). 84

[102] S. Kobayashi, M. Sera, M. Hiroi, N. Kobayashi and S. Kunii, J. Phys. Soc. Jpn. **69**, 926 (2000). 84

[103] S. Kishimoto, A. Kondo, M.-S. Kim, H. Tou, M. Sera and F. Iga, J. Phys. Soc. Jpn. **74**, 2913 (2005). 84

[104] M.-S. Kim, Y. Nakai, H. Tou, M. Sera, F. Iga, T. Takabatake and S. Kunii, J. Phys. Soc. Jpn. **75**, 064704 (2006). 84

[105] S. Kobayashi, Y. Yoshino, S. Tsuji, M. Sera and F. Iga, J. Phys. Soc. Jpn. **72**, 25 (2003). 84

[106] H. C. Walker, K. A. McEwen, P. Boulet, E. Colineau, J.-C. Griveau, J. Rebizant and F. Wastin, Phys. Rev. B **76**, 174437 (2007). 84, 92

[107] A. Prasad, H. S. Jeevan, C. Geibel and Z. Hossain, J. Phys. Condens. Matter **22**, 126004 (2010). 84

[108] T. Kawae, M. Shimogai, M. Mito, K. Takeda, H. Ishii and T. Kitai, Phys. Rev. B **65**, 012409 (2001). 84

[109] S. W. Zochowski and K. A. McEwen, Physica B **199&200**, 416 (1994). 84, 92

[110] M. Schäpers, Antiferroquadrupolare Phasen in $U(Pd_{1-x}Pt_x)_3$, Master's thesis, TU Braunschweig, 2010. 92, 93, 94, 95, 96, 97, 131, 159

[111] H. C. Walker, M. D. Le, K. A. McEwen, M. Bleckmann, S. Süllow, C. Mazzoli, S. B. Wilkins and D. Fort, Phys. Rev. B **84**, 235142 (2011). 84, 91, 131, 133

[112] T. J. Heal and G. I. Williams, Acta Crystallogr. **8**, 494 (1955). 84, 85, 88

[113] K. McEwen, W. Stirling, C. Loong, G. Lander and D. Fort, J. Magn. Magn. Mater. **76 - 77**, 426 (1988). 84, 91

[114] N. Shamir, M. Melamud, H. Shaked and M. Weger, Physica B+C **94**, 225 (1978). 85

[115] K. Andres, D. Davidov, P. Dernier, F. Hsu, W. Reed and G. Nieuwenhuys, Solid State Commun. **28**, 405 (1978). 85, 86, 91, 158

[116] S. W. Yun, H. Sugawara, J. Itoh, M. Takashita, T. Ebihara, N. Kimura, P. Svoboda, R. Settai, Y. Ōnuki and H. Sato, J. Phys. Soc. Jpn. **63**, 1518 (1994). 85, 86, 158

[117] H. Ott, K. Andres and P. Schmidt, Physica B+C **102**, 148 (1980).

[118] W. J. L. Buyers and T. M. Holden, in *Handbook on the Physics and Chemistry of the Actinides*, edited by G. H. Lander and A. J. Freeman Vol. 2, p. 289, Elsevier Science, Amsterdam, 1985. 87, 101, 159

[119] U. Steigenberger, K. McEwen, J. Martinez and D. Fort, J. Magn. Magn. Mater. **108**, 163 (1992).

[120] K. McEwen, U. Steigenberger and J. Martinez, Physica B **186 - 188**, 670 (1993). 100, 102

[121] K. McEwen, M. Ellerby and M. de Podesta, J. Magn. Magn. Mater. **140-144**, 1411 (1995).

[122] K. McEwen, U. Steigenberger, K. Clausen, Y. Bi, M. Walker and C. Kappler, Physica B **213 - 214**, 128 (1995). 86, 104

[123] C. Kappler, M. B. Walker and J. Luettmer-Strathmann, Phys. Rev. B **51**, 11319 (1995).

[124] J. Luettmer-Strathmann, C. Kappler and M. B. Walker, Phys. Rev. B **52**, 6285 (1995). 85

[125] K. McEwen, U. Steigenberger, K. Clausen, J. Kulda, J.-G. Park and M. Walker, J. Magn. Magn. Mater. **177 - 181, Part 1**, 37 (1998). 86

[126] N. Lingg, D. Maurer, V. Müller and K. A. McEwen, Phys. Rev. B **60**, R8430 (1999). 87, 158

[127] T. Takeuchi, Y. Tokiwa, R. Settai, Y. Haga, E. Yamamoto, T. Honma and Y. Ōnuki, Physica B **281-282**, 602 (2000). 86

[128] K. A. McEwen, J.-G. Park, A. J. Gipson and G. A. Gehring, J. Phys. Condens. Matter **15**, S1923 (2003). 87, 88, 101, 102, 103, 110, 111, 116, 118, 120, 138, 158

[129] W. Buyers, A. Murray, T. Holden, E. Svensson, P. de V. DuPlessis, G. Lander and O. Vogt, Physica B+C **102**, 291 (1980). 88, 101, 138, 158

[130] D. F. McMorrow, K. A. McEwen, U. Steigenberger, H. M. Rønnow and F. Yakhou, Phys. Rev. Lett. **87**, 057201 (2001). 87, 88, 89

[131] H. C. Walker, K. A. McEwen, M. D. Le, L. Paolasini and D. Fort, J. Phys. Condens. Matter **20**, 395221 (2008). 88, 90, 112, 117, 120, 127, 128, 129, 138, 158, 161

[132] H. C. Walker, K. A. McEwen, D. F. McMorrow, S. B. Wilkins, F. Wastin, E. Colineau and D. Fort, Phys. Rev. Lett. **97**, 137203 (2006).

[133] K. McEwen, H. Walker, M. Le, D. McMorrow, E. Colineau, F. Wastin, S. Wilkins, J.-G. Park, R. Bewley and D. Fort, J. Magn. Magn. Mater. **310**, 718 (2007).

[134] J. Fernández-Rodríguez, S. W. Lovesey and J. A. Blanco, J. Phys. Condens. Matter **22**, 022202 (2010). 89

[135] T. Ito, H. Kumigashira, S. Souma, T. Takahashi, Y. Haga, Y. Tokiwa and Y. Ōnuki, Phys. Rev. B **66**, 245110 (2002). 89

[136] A. N. Yaresko, V. N. Antonov and P. Fulde, Phys. Rev. B **67**, 155103 (2003).

[137] S.-i. Fujimori, T. Ohkochi, I. Kawasaki, A. Yasui, Y. Takeda, T. Okane, Y. Saitoh, A. Fujimori, H. Yamagami, Y. Haga, E. Yamamoto, Y. Tokiwa, S. Ikeda, T. Sugai, H. Ohkuni, N. Kimura and Y. Ōnuki, J. Phys. Soc. Jpn. **81**, 014703 (2012). 89

[138] L. Petit, A. Svane, W. M. Temmerman and Z. Szotek, Phys. Rev. Lett. **88**, 216403 (2002). 91

[139] A. de Visser, J. Klaase, M. van Sprang, J. Franse, A. Menovsky and T. Palstra, J. Magn. Magn. Mater. **54 - 57, Part 1**, 375 (1986). 92

[140] M. Graf, R. Keizer, A. de Visser and J. Franse, Physica B **259 - 261**, 666 (1999).

[141] A. de Visser, M. J. Graf, P. Estrela, A. Amato, C. Baines, D. Andreica, F. N. Gygax and A. Schenck, Phys. Rev. Lett. **85**, 3005 (2000). 92

[142] M. E. Fisher and J. S. Langer, Phys. Rev. Lett. **20**, 665 (1968). 92

[143] E. Bauer and M. Rotter, Magnetism of complex metallic alloys: Crystalline electric field effects, in *Book Series on Complex Metallic Alloys*, edited by E. Belin-Ferrero Vol. 2, World Scientific, 2009. 101

[144] Y. Tokiwa, private communication, 2013. 102

[145] R. Osborn, K. McEwen, E. Goremychkin and A. Taylor, Physica B **163**, 37 (1990). 102

[146] A. Abragam and B. Bleaney, *Electron Paramagnetic Resonance of Transition Ions* (Oxford University Press, Oxford, 1970). 143

[147] M. Rotter, D. M. Le, L. G. Pascut, T. Hoffmann, M. Doerr, R. Schedler, P. F. Hoffmann, S. Rotter and M. Banks, McPhase Users Manual, online, 2013, 04/23/2013. 143

Curriculum Vitae

Personal Data

Name	Dirk Schulze Grachtrup
Date of birth	16.01.1982
Place of birth	Warendorf

Education

1988 - 1992	Primary school Schuntersiedlung, Braunschweig
1992 - 1994	Orientation Level Nibelungen, Braunschweig
1994 - 2001	Gymnasium Neue Oberschule (High school), Braunschweig, Degree: Abitur

Military Service

07/2001 - 03/2002	6. / PzGrenBtl. 332, Wesendorf

Part-time Work

04/2002 - 06/2002	Gardening and construction assistance, Wulf Gartenlandschaften GmbH, Bad Harzburg and Braunschweig
07/2004 - 04/2008	Assistant work, deformation division, GOM - optical measuring techniques GmbH, Braunschweig

University

10/2002 - 06/2008	Technical University Braunschweig, Degree: Diplom, Thesis subject: *"Puls- und Relaxationskalorimetrie Vergleichsmessungen unter verschiedenen Bedingungen"*

Current Position

since 05/2008	Research assistant Institute for the Physics of Condensed Matter Technical University of Braunschweig Supervisor: Prof. Dr. Stefan Süllow

Publications

- D. Schulze Grachtrup, M. Bleckmann, S. Süllow, B. Willenberg, H. Rakoto, Y. Skourski, and J. A. Mydosh: *High Field Magnetization of* UPt_2Si_2, J. Low Temp. Phys., **159**, 147 (2010)

- D. Schulze Grachtrup, M. Bleckmann, B. Willenberg, S. Süllow, M. Bartkowiak, Y. Skourski, H. Rakoto, I. Sheikin, and J. A. Mydosh: *Field-induced phases in* UPt_2Si_2, Phys. Rev. B, **85**, 054410 (2012)

Braunschweig, November 17, 2014

Last but not least...

... I want to say a big "Thank you!" to all the people I worked with or who supported me in other ways during the last years and who had some part in the successful work here.

First of all there are our workshop, electronics and technical staff who take care of all the broken things, replacement parts and expendable supplies. And despite the fact that some things take their time they are really fast with an impressive precision in urgent cases and whenever really necessary. And of course it is always fun to hear some new stories from Thilo.

Then I have to mention Ilya Sheikin, my local contact for the high magnetic field experiments in Grenoble. Each time I went there it was a pleasure to work with him, even though that meant long, but exciting and successful nights in front of the computers in the lab. And luckily he wasn't offended even when I had to wake him up in the middle of the night to solve some unexpected issues. At this point I also want to mention Nico for performing the last successful set of experiments in Grenoble some weeks ago which verified some of the theses presented here and bringing back two bottles of Gigondas.

Furthermore, there is Mucio Continentino in Rio de Janeiro who invited me to stay at the CBPF for two months to begin my theoretical studies on $U(Pd_{1-x}Pt_x)_3$ and who was very supportive and organized a great place to stay for me (Thanks Yara for the great time in your appartment!). And not to miss all the PhD students at the CBPF who invited me almost everywhere and made me feel really comfortable in

Rio, especially Isabel.

Of course I also have to mention Gertrud Zwicknagl who continued to guide my calculations to success back here in Braunschweig and who was very supportive and most of the time quickly available to discuss any physical issues. Without her help and corrections to my code this thesis would have probably taken much longer. Thanks for all this help.

Besides all the people somehow directly involved in the work for this thesis I am very grateful to Hella who takes all my quirks (like lots of thermometers at home), all the traces of what might be called in general *physicists behavior* and several weekend or evening visits at the institute. And who also makes the time spent outside of the institute very pleasant. I am as grateful to Julia who likes to sleep long (as her parents do) and always wakes up in the morning with a big smile and thus allowed for enough rest and a cheerful morning so that all the thinking and writing to finish this thesis did not become too hard. And of course the same applies to Felix who also sleeps very well which is what he does most of the time as it is normal for his age.

Then I have to thank my parents and grandparents for lots of support. Not only, but in particular, some financial support in the first 6 years at the university until I finished my first degree. Another important source of steady support and motivation are all the friends here in Braunschweig (and wherever they moved in the last years) who always provided a lot of amusement and good reasons to procrastinate. And besides, their regularly asked question "What exactly is it what you're doing?" reliably kept me from drifting too far from a non-physicists life.

To produce good work it is of course important to have a nice and pleasant surrounding. Unfortunately the physics building is not an advantage in this sense. Luckily, the people at the institute make more than up for this. Here, I want to mention some of them in particular. First, Matthias, Jan and Ali who already were PhD students when I

started my thesis and introduced me into the lab and life as a PhD student very nicely (including a not so cheap special course in German grammar). Next, there are Daniela, Josefin and Teresa who share one office with me and are very kind company. And of course, Mathias, who became a good friend in the last years and is involved in lots of amusing and not so scientific activities at the institute (as most steady participant of the after-work beer, co-developer of the famous beer cooler, activist for an enhanced room 044 and after-lunch-battle opponent who lets me win sometimes, just to name the most important) as well as in the outside world (Rock Harz, Berlin Rock City, W:O:A, etc.). And there is still one crate of beer waiting due to an unlucky bet.

And finally, of course, a big THANKS to my advisor Stefan Süllow who, once you get hold of him, always has lots of good ideas and useful comments to all the scientific challenges popping up every now and then. Who additionally is very supportive when it comes to writing applications for experiments or funding and made many conference trips possible (besides providing funding for my position all the years). And besides the scientific part, he showed a very high level of tolerance and support to all our at most semi-scientific side projects and office modifications. Furthermore, he even encouraged us to continue with some of these projects and, last but not least, he provided a state-of-the-art coffee maker for our group.